

**COMPRESSIONAL BEHAVIOR OF HYDROGEN-BONDED CRYSTALS:  
ANHYDROUS COMPARISONS AND POLYMORPHISM**

by

*Hannah L. Shelton*

A DISSERTATION SUBMITTED TO THE GRADUATE DIVISION OF THE  
UNIVERSITY OF HAWAI'I AT MĀNOA IN PARTIAL FULFILLMENT OF THE  
REQUIREMENTS FOR THE DEGREE OF  
DOCTOR OF PHILOSOPHY  
IN  
GEOLOGY AND GEOPHYSICS  
DECEMBER 2018

Dissertation Committee:

Przemyslaw Dera, Chairperson

Bin Chen

Hope Ishii

Eric De Carlo

Craig Jensen

## ACKNOWLEDGEMENTS

First and foremost, I would like to thank my adviser, Dr. Przemyslaw Dera. Your patience and expertise have been invaluable. The learning curve was steep, but you went above and beyond in providing me with research opportunities and looking out for my best interests. To my committee members Dr. Bin Chen, Dr. Hope Ishii, Dr. Eric De Carlo, and Dr. Craig Jensen - thank you for your support, many lessons, and willingness to comb through the following 150 pages. My sincere thanks go to Dr. Madison Barkley, Dr. Eva Zurek, Tiange Bi, Dr. Jesse Smith, and Dr. Sergey Tkachev for their roles in the following chapters. I would also express my gratitude to Dr. G. Jeff Taylor for his sage wisdom and puns, and Dr. John Sinton for his encouragement to apply to G&G.

To my mineral physics lab-mates Yi Hu, Greg Finkelstein, Xiaojing Lai, Tommy Yong, May Chornkrathok, and Warren McKenzie – thank you for all of the camaraderie (and making me feel useful!) An additional shout out to Jeff Montgomery, Savannah Spencer, John Lazarz, Will Bassett, Jeff Pigott, Erin Nissen, Matt Whitaker, Camelia Stan, and Earl O’Bannon for the strange but solid friendships from conferences and beamtime.

John, Noah, CJ, Evan, Warren, and Sharra – you have been a deeply valued source of sanity, and the lab collectively owes you for making me come to work on the weekend. Caroline - thank you for aggressively becoming my friend during petrology class, and sticking with me since then. To the rest of the G&G, HIGP, and Zoo crew – I promise I didn’t forget you, but I am running out of room. Mea culpa.

To Justin, who keeps me company late at night, sits through traffic to pick me up from the airport, and comforts me when my experiments fail – know that I could not have done this without you.

To my parents, who are endlessly proud despite not knowing what I do, know that space camp was a really good decision.

Additional thanks are due to the Carnegie-DOE Alliance Center, which funded much of this work under cooperative agreement DE FC52-08NA28554, as well as NSF grant EAR-1541516, and the Fred M. Bullard Fellowship for continuing graduate students.

## ABSTRACT

Hydrogen, despite its ubiquity, remains a little-understood factor in high pressure mineral physics and material science. Hydrogen in the solid state can profoundly affect the structure and behavior of crystal, often as hydrogen bonding interactions. In a geological setting, the addition of hydrogen – typically as water – drastically changes the material properties of mantle minerals, including the rheology, electrical conductivity, elasticity, and phase transition conditions. However, the degree of influence that hydrogen exerts is often variable, which makes the determination of structural and thermoelastic information at high pressures more difficult. To better understand its role in crystal structures, analogue materials have been used to explore the influence of hydrogen in crystal structures at high pressure. In this dissertation, several high pressure crystal structures with relevance to planetary and materials science have been examined in the context of hydrous and anhydrous analogues. Chapter 3 describes the high pressure behavior of the mineral  $\beta$ -behoite ( $\text{Be}(\text{OH})_2$ ) as a hydrous analogue structure to  $\alpha$ -cristobalite, a high-temperature polymorph of  $\text{SiO}_2$ . The low-pressure structures  $\beta$ -behoite and  $\alpha$ -cristobalite are topologically identical, but differ by the added presence of  $\text{O}-\text{H}\cdots\text{O}$  hydrogen bonds, which add structural rigidity and resist distortion of the structure. As a result, behoite does not follow cristobalite's phase transition pathway to higher coordination states. This pathway is discussed in detail within Chapter 4, where the change in Si ion coordination at high pressures creates a polymorph called cristobalite X-I. This phase is the only known octahedrally coordinated phase of  $\text{SiO}_2$  that cannot be returned to ambient pressures, and represents a bridge in the densification process of  $\text{SiO}_2$  that occurs within the Earth. Additionally, cristobalite X-I is discussed as an analogue structure for six-coordinated  $\text{CO}_2$ , which may occur in the interiors of giant planets. Lastly, Chapter 5 examines high-pressure hydrogen bonding and polymorphism in melamine, an

aromatic organic molecule derived from *s*-triazine that forms an extensive network of hydrogen bonds. These hydrogen bonds inhibit reactivity and polymorphism when compared to non-hydrogen bonded organic crystals like *s*-triazine and benzene, and may act as a stabilizer in the formation of co-crystals relevant to molecular materials and organic minerals.

## **TABLE OF CONTENTS**

ACKNOWLEDGEMENTS .....	ii
ABSTRACT .....	iii
TABLE OF CONTENTS.....	v
LIST OF TABLES .....	vii
LIST OF FIGURES .....	ix
<b>CHAPTER 1. INTRODUCTION .....</b>	<b>1</b>
1.1. The Mineralogical Role of Hydrogen.....	1
1.2. Hydrous Analogues of Anhydrous Mineral Systems .....	4
1.3. High-Pressure Hydrogen Bonding in Organic Crystals.....	8
<b>CHAPTER 2. EXPERIMENTAL METHODS .....</b>	<b>11</b>
2.1. High Pressure in Diamond Anvil Cells (DACs).....	11
2.2. Single Crystal X-Ray Diffraction .....	14
2.3. Computational Methods.....	18
2.4. Raman Spectroscopy .....	22
<b>CHAPTER 3. HYDROGEN BOND EFFECTS ON COMPRESSIONAL BEHAVIOR OF ISOTYPIC MINERALS: HIGH-PRESSURE POLYMORPHISM OF CRISTOBALITE-LIKE Be(OH)<sub>2</sub></b>	
ABSTRACT.....	24
3.1. INTRODUCTION .....	25
3.2. MATERIALS AND METHODS .....	28
3.2.1 Ambient X-ray Diffraction .....	28
3.2.2 High-Pressure X-ray Diffraction .....	29
3.3. RESULTS .....	35
3.3.1 Structural Evolution.....	35
3.3.2 Symmetry Relations Between $\beta$ - and $\gamma$ -phases .....	42
3.3.3 Equation of state .....	44
3.4. DISCUSSION.....	48
3.5. CONCLUSIONS .....	52
3.6. ACKNOWLEDGEMENTS.....	53

**CHAPTER 4. THE IDEAL CRYSTAL STRUCTURE OF CRISTOBALITE X-I: A BRIDGE IN SiO<sub>2</sub> DENSIFICATION**

ABSTRACT .....55

4.1. INTRODUCTION .....56

4.2. EXPERIMENTAL AND COMPUTATIONAL METHODS .....58

    4.2.1 Single-Crystal X-ray diffraction.....58

    4.2.2 DFT Calculations.....61

4.3. RESULTS .....63

4.4. DISCUSSION.....76

4.5. CONCLUSIONS .....78

4.6. ACKNOWLEDGMENTS.....79

**CHAPTER 5. EVOLUTION OF INTERATOMIC AND INTERMOLECULAR INTERACTIONS AND POLYMORPHISM OF MELAMINE AT HIGH PRESSURE**

ABSTRACT .....80

5.1. INTRODUCTION .....81

5.2. MATERIALS AND METHODS .....84

5.3. RESULTS.....86

    5.3.1 X-Ray Diffraction.....86

    5.3.2 Equation of State and Bond Compressibility .....88

    5.3.3 Hydrogen Bonding Behavior with Pressure .....95

    5.3.4 Raman Spectroscopy .....99

5.4. DISCUSSION.....103

5.5. ACKNOWLEDGMENTS .....104

**CHAPTER 6. CONCLUSIONS AND FUTURE PROSPECTS .....105**

APPENDIX A: SUPPLEMENTARY MATERIAL TO CHAPTER 4 .....109

APPENDIX B: SUPPLEMENTARY MATERIAL TO CHAPTER 5.....112

References.....116

## LIST OF TABLES

### CHAPTER 3:

3.1 Summary of data collection, crystallographic data, and refinement statistics.....	32
3.2 Unit cell parameters of low- and high-pressure behoite ( $\text{Be}(\text{OH})_2$ ).....	33
3.3 Fractional atomic coordinates and atomic displacement parameters.....	34
3.4 Definitions of symmetry operations.....	34
3.5 Anisotropic displacement parameters of beryllium .....	36
3.6 Bond distances ( $\text{\AA}$ ) for UA1, UA1_0, UA2, UA4, IDD5.....	36
3.7 Bond angles ( $^\circ$ ) for UA1, UA1_0, UA2, UA4, IDD5 .....	37
3.8 Hydrogen bonding distances ( $\text{\AA}$ ) for UA1, UA2, UA4, IDD5 .....	38
3.9 Hydrogen bonding angles ( $^\circ$ ) for UA1, UA2, UA4, IDD5.....	39

### CHAPTER 4:

4.1 Data collection and refinement details for $\text{SiO}_2$ X-IH 10.7(1) GPa .....	66
4.2 Atomic coordinates and displacement parameters of $\text{SiO}_2$ X-IH at 10.7(1) GPa .....	66
4.3 Bond lengths ( $\text{\AA}$ ) of $\text{SiO}_2$ X-IH at 10.7(1) GPa .....	67

### CHAPTER 5:

5.1 Selected data collection and refinement details from lowest and highest pressure points .....	88
5.2 Evolution of unit cell parameters of melamine with pressure .....	90

### APPENDIX A:

A1 Unit cell parameters experimental methods.....	112
A2 Unit cell parameters from DFT (vdW-optB88) methods .....	113
A3 Definitions of symmetry operations.....	114
A4 Calculated elastic properties at 10 GPa .....	114
A5 Calculated Debye frequency and Debye temperature at 10 GPa.....	115
A6 Calculated Elastic Tensors at 10 GPa .....	115
A7 Locations of octahedral voids in the X-IB model.....	119

<b>A8</b> Locations of octahedral voids in the X-IH model.....	119
<b>A9</b> Possible SiO <sub>2</sub> structures with full Si atom occupancies in the X-IB oxygen sublattice .....	120
<b>A10</b> Possible SiO <sub>2</sub> structures with full Si atom occupancies in the X-IH oxygen sublattice .....	120
<b>A11</b> Comparison of results of the four comparative crystallographic refinements.....	121

**APPENDIX B:**

<b>B1</b> Selected bond lengths and angles for melamine at 36.2(1) GPa.....	124
<b>B2</b> Atomic coordinates and equivalent isotropic displacement parameters for carbon and nitrogen atoms in melamine at 36.2(1) GPa.....	124
<b>B3</b> Definitions of symmetry operators.....	125
<b>B4</b> Hydrogen bond D-H-A lengths and angles at 36.2(1) GPa .....	125

## LIST OF FIGURES

### CHAPTER 1:

1.1. Crystal structures of CaCl <sub>2</sub> -type SiO <sub>2</sub> and $\delta$ -AlOOH, in space group Pnmm .....	6
1.2. Crystal structures of MgSiO <sub>3</sub> perovskite (bridgmanite) and MgSi(OH) <sub>6</sub> hydroxide-perovskite (“3.65 Å-phase”) .....	7
1.3. Comparison of aniline-II, <i>o</i> -diaminobenzene, benzene-II, and <i>s</i> -triazine, with the viewing axis specified .....	10

### CHAPTER 2:

2.1. Cutaway view of a diamond anvil cell interior .....	12
2.2. Example of ruby fluorescence-based pressure measurement .....	13
2.3. Example phonon dispersion curve and density of states .....	21
2.4. Example of Rayleigh, Stokes, and Anti-Stokes photon scattering .....	23

### CHAPTER 3:

3.1. Comparison of BeO <sub>4</sub> , ZnO <sub>4</sub> , and SiO <sub>4</sub> tetrahedra structures in behoite, wülfingite, and $\alpha$ -cristobalite .....	28
3.2. Low-pressure (0.3(1) GPa) and high-pressure (7.7(1) GPa) diffraction patterns of Be(OH) <sub>2</sub> .....	31
3.3. Bifurcation of the hydrogen bonds in Be(OH) <sub>2</sub> with pressure within the $\beta$ -phase .....	40
3.4. Rotation of Be(OH) <sub>2</sub> tetrahedra between low- and high-pressure phases .....	40
3.5. Hydrogen bonding environments in low- and high-pressure Be(OH) <sub>2</sub> .....	43
3.6. Diagram of subgroup–supergroup relations between the low and high-pressure phases of Be(OH) <sub>2</sub> .....	45
3.7. $F_f$ plot for the high-pressure phase of Be(OH) <sub>2</sub> .....	46
3.8. Pressure evolution of unit cell volume of Be(OH) <sub>2</sub> across the phase transition .....	47
3.9. Pressure evolution of unit cell parameters of Be(OH) <sub>2</sub> .....	48

## CHAPTER 4:

4.1. Indexed diffraction patterns of cristobalite X-I at 12.5 GPa and quenched sample containing $\alpha$ -cristobalite .....	60
4.2. Phonon band structure and density of states for cristobalite X-I at 10 and 2.5 GPa .....	62
4.3. Comparison of octahedral chain geometries in high density polymorphs of SiO <sub>2</sub> .....	65
4.4. Possible SiO <sub>2</sub> crystal structures with fully occupied Si sites in X-IB, X-IH models .....	69
4.5. Comparative crystal structure refinement results of the X-IH and X-IB models .....	70
4.6. Enthalpies as a function of pressure for cristobalite-II, stishovite, seifertite, post-quartz, and SiO <sub>2</sub> X-I.....	72
4.7. Theoretically determined heat capacities ( $C_v$ ) for cristobalite-II, stishovite, seifertite, post-quartz, and SiO <sub>2</sub> X-I .....	73
4.8. Comparison of equations of state for SiO <sub>2</sub> X-I, stishovite, and seifertite .....	75
4.9. Pressure dependence of normalized unit cell parameters of SiO <sub>2</sub> X-I .....	76

## CHAPTER 5:

5.1. Hydrogen bonding network of melamine at low and high pressures .....	83
5.2. Diffraction patterns of low- and high-pressure phases of melamine.....	87
5.3. Visible changes in a melamine crystal before and after the irreversible high-pressure amorphization at 45 GPa .....	87
5.4. Evolution of normalized unit cell parameters of melamine with pressure .....	89
5.5. Evolution of unit cell volume of melamine with pressure .....	91
5.6. Average carbon-nitrogen bond lengths for ring and amine components of melamine .....	92
5.7. Hirshfeld surfaces displaying the shape index of melamine at low and high pressures.....	94
5.8. Hirshfeld surfaces displaying $d_{\text{norm}}$ at 0.96(5), 17.1(1), and 36.2(1) GPa .....	94
5.9. Intra-plane hydrogen bond D $\cdots$ A distance as a function of pressure .....	95
5.10. Inter-plane hydrogen bond D $\cdots$ A distance as a function of pressure .....	96
5.11. Hydrogen bonding network of melamine at low and high pressures .....	98
5.12. Electrostatic potential surfaces of melamine molecules at low and high pressures .....	98
5.13. Raman spectra of melamine in N-H vibration region .....	100

<b>5.14.</b> Raman spectra of melamine in the ring vibration-mode range .....	101
<b>5.15.</b> Raman spectra of melamine in the C-N vibration mode range .....	102

**APPENDIX B:**

<b>B1</b> Ring centroid-centroid distance and shift as a function of pressure .....	122
<b>B2</b> F-f plot for data plotted with a third-order Vinet equation of state .....	123

## CHAPTER 1. INTRODUCTION

### 1.1 The Mineralogical Role of Hydrogen

The response of a crystal system to applied stresses is controlled by the interplay of competing atomic forces, and shifts of this balance have significant effects on material properties and polymorphism. The presence of hydrogen within a crystal is no exception, and may exert its influence over the physical properties of a crystal in a variety of ways. As a structural component, various hydrogen-bearing functional groups are common in both organic and inorganic crystals, and inter- and intra-molecular hydrogen bonding often directs crystal growth and structure [1, 2]. Hydrogen may also be introduced interstitially into a crystalline solid, where hydrogen bearing ions (often  $H^+$ ,  $OH^-$ , or  $NH_4^+$ ) may substitute for other ions as structural defects [3-6], and both neutral molecules and ions may reside as guest inclusions within void spaces or form clathrates [4, 5, 7, 8]. Hydrogen's behavior in crystals is of marked interest in solid state chemistry and materials science, where it is both a building block and a tool of crystal engineering [9, 10]. Its importance extends into planetary sciences, where the presence or absence of hydrogen is felt in both micro- and macro-scale geological processes [11]. The interaction of hydrogen with rock-forming silicate minerals – typically as  $H_2O$  within the oxidizing regions of the Earth [12] – is associated with pronounced changes in the rheology and thermal transport properties of mantle materials. For instance, the addition of water on a geologic scale facilitates both near-surface processes like back-arc volcanism near subducting slabs, and may govern less-understood processes such as deep-mantle melting and plume upwelling [13].

The presence of hydrogen in crystal structures often manifests as hydrogen bonds between structural features. Hydrogen bonding inherently involves three atoms, where a donor, hydrogen atom, and acceptor (abbreviated as  $D-H\cdots A$ ) interact with one another in an incipient proton-transfer reaction. The strength of this interaction is dependent on the species of donor and acceptor as well as the geometry of the bond [14], with energies ranging from weakly electrostatic to covalent [14], roughly 0.2 to 40 kcal/mol. Common donors and acceptors are oxygen, nitrogen, and sulfur, along with halogens and  $\pi$ -bonds that may act as strong and weak acceptors, respectively [1, 14]. Shorter, more linear bonds are generally stronger at ambient conditions, with symmetric bonds (where the proton is equidistant to donor and acceptor) considered to be especially strong. The stability of the bond can be further modified by the local

environment; for instance, bonds may be strengthened by resonance effects and electronic activation, or may be weakened by steric hindrance and repulsive interactions. If the density of available acceptor atoms is high enough, two or three acceptors may participate simultaneously, forming bifurcated and trifurcated bonds. The possibility of symmetrization and bifurcation grows as a crystal is compressed and donor-acceptor pairs on neighboring molecules or functional units are brought in closer to one another. Although this causes a decrease in bond length, it does not necessarily translate into an increase of bond strength; pressurization may distort hydrogen bonds from the ideal, linear arrangement or push the bond into an unstable, repulsive arrangement [15]. Hydrogen bond networks generally resist structural changes induced by compression in both minerals and molecular crystals, and this stability correlates strongly to the amount of bonding interactions [15, 16]. Conversely, in crystals where hydrogen bonding is not a dominant structural motif, and interactions occur in interstitial sites or from incomplete hydroxylation, the presence of hydrogen appears to destabilize many crystal structures under compression [17].

Most hydrated minerals, either as hydroxides or hydrates, do not persist in the Earth's interior to great depths, but can be directly implicated in the transport of surface water and other volatiles into the mantle. The most prevalent of these are formed from common silicate minerals, such as pyroxene-derived amphiboles and chlorites, which are commonly found in oceanic environments where large-scale hydrothermal alteration may occur [13]. This oceanic crust can contain up to 50% hydrated species [18], and is recycled into the mantle through subduction zones, where water and other volatile species are liberated as the hydrous mineral phases decompose under heat and pressure [13, 19, 20]. The fate of the hydrated mineral species depends on several factors, including the speed at which they are subducted, the temperature of the surrounding asthenosphere and upper mantle, and the activity of water in the surrounding area. At high temperatures, these dehydration and dehydrogenation processes produce anhydrous species such as olivine, ortho- and clinopyroxenes, and silica phases [19], as well as H<sub>2</sub>O-rich fluids that accumulate in the mantle wedge [21]. Measurable amounts of water can be incorporated into these nominally anhydrous mantle mineral (NAM) species under high-pressure conditions [22]. For instance, (Mg,Fe)<sub>2</sub>SiO<sub>4</sub> polymorphs can incorporate significant amounts of water within their structures, up to several weight percent [23]. This added water (as OH<sup>-</sup> and H<sup>+</sup>) acts as a

structural defect, requiring local charge balance by cation vacancies, or incorporation by crystallographic shearing mechanisms [8, 23], which reduces overall bond strength and promotes polymorphism [23, 24]. This results in potentially observable mantle anomalies: the presence of 1 percent water by weight within ringwoodite at ambient conditions depresses the shear modulus comparable to an anhydrous temperature increase of approximately 800-1000°C [23]. The addition of water to stishovite, an octahedrally coordinated high-pressure polymorph of SiO<sub>2</sub>, may also be visible as seismic and electrical conductivity anomalies of the mid and lower mantle [3, 25, 26] and can be linked to experimentally observed decreases in elastic moduli and lowering of phase transition pressures [17, 22].

In sufficiently fast-moving and low-temperature subduction environments, a suite of hydrated high-pressure minerals known as dense hydrous magnesium silicates, or “alphabet phases” may form [8]. The evidence for these phases comes almost entirely from laboratory experiments, with a few exceptions [27], but they appear to form at upper and mid-mantle pressures under sufficiently water-rich conditions [28] and may act as a vehicle for water transport below the transition zone [8]. Unlike the hydrogen incorporation in nominally anhydrous species, the high-pressure hydrogen bonding in dense hydrous magnesium silicates [29-31] and  $\delta$ -AlOOH [32-34] may be responsible for phase stabilization and stiffening of the elastic moduli, and could be perceivable as anomalously fast acoustic velocities in the vicinity of the mantle transition zone. In very fast-moving slabs, these minerals may be transported as far as the core-mantle boundary [22]. The interaction of this hydrous material and the reduced iron in the Earth’s outer core may create iron hydrides and free hydrogen, forming the deepest component of the Earth’s hydrogen-water cycle [12, 35].

The influence of hydrogen in planetary interiors also extends to other planets and moons: the high pressure behavior of molecular hydrogen has been the subject of long-running investigation and debate [36-42], with consequences for the formation history and internal structure of gas giant planets. Other simple species such as NH<sub>3</sub> and H<sub>2</sub>O form rich varieties of solid phases in response to pressurization [38, 42-45], driven by an equally wide range of nuclear and electronic interactions; for example, there are more than fifteen stable phases of water ice, each varying by the structure and ordering of hydrogen bonding networks [8, 45]. Hydrogen-bond interactions form the mineralogical basis for the icy moons and dwarf planets of the outer solar system,

where the surface mineralogy is predominantly ultra-low temperature ices instead of silicates [46, 47], and the interior geodynamics may be driven by ammonia and salt-rich subsurface oceans interacting with high-pressure water ices [46, 48]. Titan, the largest moon of Saturn, has an exceptionally exotic lithology composed of low-density molecular materials such as water and ammonia ices, organic crystals and hydrates, and methane-based surface fluids [49-51]. Although the internal structure of Titan is largely unknown, the subduction or subsumption of molecular minerals and hydrates into a subsurface ocean could occur through tectonic and cryovolcanic processes analogous to the transport of water into the Earth's mantle [48, 52]. Similarly, the high-pressure behavior of these hydrogen-bearing molecular minerals is largely unexplored: although molecular organic compounds have been a popular subject of high-pressure research with regard to functional materials, they have been a minor topic in high-pressure mineral physics research [16].

## **1.2 Hydrous Analogues of Anhydrous Mineral Systems**

Although there is ample evidence for the presence of water and hydrogen-bonding interactions within the Earth's mantle, the variable behavior of hydrogen within minerals complicates the determination of structural parameters. Small changes in the pressure, temperature, and hydration conditions of experiments can also lead to potentially conflicting results: For instance, various high-pressure and high-temperature hydration experiments of  $\text{MgSiO}_3$  perovskite have produced solubility estimates as low as several parts per million to as high as 0.4 weight percent [22, 53]. The degree of hydrogen incorporation produces complex changes in physiochemical behavior [16], where small variations in water content can have dramatic effects on the thermoelastic properties and polymorphism [11, 23]. Without thermoelastic information at the upper bounds of hydration for these minerals, realistic interpretations of seismic data to describe areas of the mantle with elevated water content are challenging [54].

The use of analogue materials in high-pressure mineral physics is a common method to explore the effects of elemental substitution and composition-dependent phase behavior in structurally similar compounds. Analogue phases have been especially prevalent in studies of lower mantle minerals, where small differences in elemental composition can result in large variability in pressure-dependent structural properties such as cation coordination number and

polyhedral connectivity. The perovskite to post-perovskite phase transformation in  $ABX_3$  structures is a well-investigated example, where the transformation of  $MgSiO_3$  bridgmanite (space group  $Pbnm$ ) to a post-perovskite structure (space group  $Cmcm$ ) is often implicated as the source of the  $D''$  discontinuity at the Earth's core-mantle boundary [55]. This transformation occurs at approximately 125 GPa and 2500 K, creating a very technically challenging high-pressure experiment, and the  $MgSiO_3$  post-perovskite crystal is only stable at very high pressure, which limits possible analysis techniques. The experimental difficulty combined with the geophysical importance has driven interest in the high-pressure behavior of other materials that undergo the perovskite to post-perovskite transition, but at much lower pressures [56]. A variety of transition metal oxides and fluorides inhabit this system, including  $CaIrO_3$ ,  $CaRhO_3$ ,  $NaFeF_3$ , and  $MgGeO_3$ , whose comparably mild phase transition conditions allow for the exploration of pressure-induced polymorphism in silicate perovskites at lower pressures and temperatures [57-59].

Other investigations have been made using  $AX_2$  system analogues to understand pressure-dependent polymorphism in fundamental materials like  $SiO_2$  and  $CO_2$ . Despite their dissimilarity at ambient pressures and temperatures,  $CO_2$  and  $SiO_2$  share several isostructural polymorphs [60-62], and the densification pathways of  $SiO_2$  have been used in predicting ultra-high pressure phases of  $CO_2$  possible within giant planets [60, 61]. Similarly,  $GeO_2$  shares common structures and phase transformation pathways with  $SiO_2$  [63], and can achieve higher coordination states at lower pressures due to its larger cation radius [64]. This makes it an attractive model for studying the mechanisms of coordination change in  $SiO_n$  polyhedra, which are responsible for depth-dependent stratification of the Earth's mantle [28].

Analogue structures have also been used to study the role of hydrogen in nominally anhydrous systems. For water incorporation within the mantle, comparisons are often made between structurally related mineral species that form a gradient dependent on stoichiometric  $OH^-$  content. For example, the dense hydrous magnesium silicate phase H ( $MgSiO_2(OH)_2$ ), high-pressure  $\delta$ - $AlOOH$ , and  $CaCl_2$ -type  $SiO_2$  are topologically identical in the space group  $Pnnm$  [22, 28].

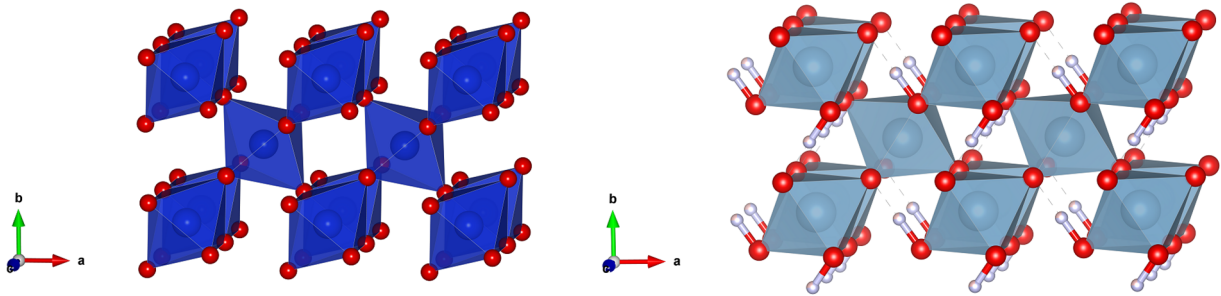


Figure 1.1.  $CaCl_2$ -type  $SiO_2$  (left) [65] and  $\delta$ - $AlOOH$  (right) [33].  $\delta$ - $AlOOH$  is structurally identical to  $CaCl_2$ -type  $SiO_2$ , but with hydrogen bonds that distort the chain of octahedra.

The stability fields for these phases within the mantle overlap to a great degree and likely form solid solutions with one another, where phase transition pressures are significantly lowered in the silicate species by aluminum and hydroxyl incorporation [66-68].

Comparisons may also be made between oxide and hydroxide crystals whose crystal structures are not identical, but are linked by crystallographic relationships. Perovskite-group crystals again provide an example: hydroxide perovskites, with a general formula of  $BB'(OH)_6$ , deviate from the ideal  $ABX_3$  stoichiometry with the full protonation of corner-shared oxygens, potential splitting of the B cation site symmetry, and the absence of an A-site counter ion [69]. Generally, hydroxide-perovskites have lower symmetry than their anhydrous counterparts, dependent on the number of equivalent hydrogen positions and the hydrogen bonding topology in the cavities between oxygen-sharing polyhedra [70, 71]. Examples include stottite ( $FeGe(OH)_6$ ), tetrawickmanite ( $MnSn(OH)_6$ ), and the “3.65 Å-phase” ( $MgSi(OH)_6$ ).  $MgSi(OH)_6$  represents an idealized hydrous magnesium silicate derivative of  $MgSiO_3$ , and their crystal structures are related by a supergroup-subgroup relationship where the addition of hydrogen reduces the overall symmetry from  $Pbnm$  to  $P2_1/n$  [72]. There is little information regarding the high-pressure behavior of most hydroxide perovskites, despite relevance for both industrial hydrogen storage and water within the deep Earth [69, 71, 73].

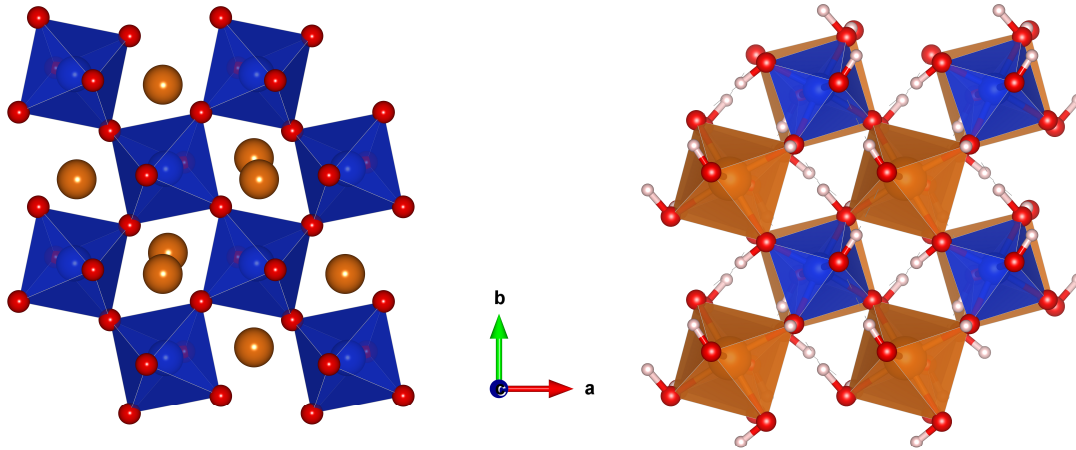


Figure 1.2.  $\text{MgSiO}_3$  perovskite (bridgmanite, left) [28] and  $\text{MgSi}(\text{OH})_6$  hydroxide-perovskite (“3.65 Å-phase”, right) [72]. In bridgmanite,  $\text{SiO}_6$  octahedra surround  $\text{Mg}^{2+}$  ions in the A-site. In the 3.65 Å-phase, Mg and Si ions sit in the octahedral sites, with bridging hydrogen bonds in the A-site vacancy.

Chapters 3 and 4 describe the high-pressure behavior of similarly structurally-related species,  $\beta$ -behoite ( $\text{Be}(\text{OH})_2$ ) and  $\alpha$ -cristobalite ( $\text{SiO}_2$ ).  $\alpha$ -cristobalite is a high temperature, low-pressure tetrahedrally-coordinated polymorph of  $\text{SiO}_2$  with tetragonal symmetry (space group  $\text{P4}_12_12$ ), and is common to terrestrial igneous environments, protoplanetary disks, and industrial ceramics [74-77]. Behoite is not a common mineral species, but possesses a very similar structure with lower orthorhombic symmetry (space group  $\text{P2}_12_12_1$ ), where the presence of hydrogen bonding distorts the inter-tetrahedral network from that seen in  $\alpha$ -cristobalite. These two minerals otherwise possess topologically identical frameworks of corner-connected tetrahedra, and initially show compression-driven displacive phase transitions at similar pressures. However, the hydrogen bond network within behoite appears to preserve the corner-shared tetrahedral structure to much higher pressures than seen in cristobalite. Within Chapter 3, the compressional behavior of behoite up to approximately 30 GPa is described, and its use as a fully-hydrated analogue material of cristobalite is discussed. Chapter 4 describes the high-pressure phase transformation behavior of cristobalite, with emphasis on the structure of the octahedrally-coordinated polymorph known as cristobalite X-I, its relationship to other high-pressure silica phases, and analogies to the high-pressure behavior of  $\text{CO}_2$ .

### 1.3 High-Pressure Hydrogen Bonding in Organic Crystals

The compressional behaviors of organic compounds have been of interest since the earliest days of high-pressure science [78], but experiments were relatively rare in comparison to those on elements, metals, and inorganic compounds [79]. Within the last three decades, significant advances in high-pressure X-ray diffraction and vibrational spectroscopy techniques have allowed for systematic studies of the high-pressure polymorphism of crystalline organic solids, with applications primarily for pharmaceuticals, energetic materials, and molecular electronics research [80]. These studies have often focused on the noncovalent intra- and intermolecular interactions that direct crystal packing, polymorphism, and reactivity, of which hydrogen bonding is considered the strongest and most versatile [81, 82]. Although the high-pressure behavior of organic crystals has typically been approached from an industrial perspective, there is applicability to the mineralogy of organic-rich planets and moons: photochemical reactions in Titan's nitrogen and methane-rich atmosphere are predicted to create complex aromatic hydrocarbons and nitrogen heterocycles, known as tholins, which would be deposited on the surface [83, 84]. Intermolecular hydrogen-bonding processes could drive the geological interactions and polymorphism in many tholin-derived molecular minerals within Titan [49].

As with the anhydrous-to-hydrous gradients and hydrated analogues of silicate minerals, the effects of hydrogen bonding may be compared between related molecules that differ by the amount, geometry, or strength of hydrogen-bonding functional groups. For instance, benzene, aniline, and *ortho*-, *meta*-, *para*-diaminobenzenes differ by the degree and geometry of amine functional groups [85-88]. In this case, benzene forms the base structural unit that the subsequent compounds are built upon, with no functional groups that are able to form directional interactions beyond weak C-H $\cdots$  $\pi$  interactions. The addition of amino groups allows for N-H $\cdots$ N and N-H $\cdots$  $\pi$  bonding that directs the orientations of the molecules with respect to their neighbors, as well as adding additional electron density from the delocalized lone pair of electrons of the amino nitrogen. The hydrogen bonds, primarily the N-H $\cdots$ N interactions, also exert control over the high pressure polymorphism and reactivity. This has previously been examined in benzene and aniline: in benzene, pressure causes the molecular orbitals of adjacent molecules to overlap, causing electronic delocalization and a reduction of the energy gap between the ground and excited electronic states. This in turn promotes dimerization between

neighboring molecules and amorphization of the crystal [89]. Conversely, the N-H $\cdots$ N bonds between individual molecules in aniline stabilize the crystal structure under pressure and raise the threshold of reactivity when compared to benzene [87, 89, 90].

Similar studies have been conducted with deliberate emphasis on the design and control of energetic molecular materials for use in explosives. Here, changes in the molecular structure and hydrogen bonding capability have been examined systematically in related energetic materials to determine thermodynamic properties, and by extension the mechanical stability and thermal activation behavior. For instance, in pentaerythritol tetranitrate (PETN) derivatives, variations in the non-energetic functional groups were studied to determine the effect of intermolecular hydrogen bonding and molecular packing density on the reactivity of the nitrate ester functional group [91]. Although a general trend was observed between the energy of detonation and handling sensitivity, the added presence of hydrogen bonding correlated most strongly with decreased sensitivity, and only weakly correlated with decreased detonation energies. Similar behavior has also been observed in other energetic materials such as TATB and DATB [92-94], where additional hydrogen-bond mediated intermolecular interactions such as  $\pi$ - $\pi$  interactions also decreased impact sensitivity without compromising detonation energies.

This approach can also be extended to other systems, such as *s*-triazine (1,3,5-triazine) and its derivatives. As with benzene, *s*-triazine does not display evidence of hydrogen bonding, and also experiences pressure-induced destabilization (although by a different mechanism) [95, 96]. Melamine (1,3,5-triazine-2,4,6-triamine), a derivative of *s*-triazine with NH<sub>2</sub> groups bonded to each carbon, forms an extensive hydrogen bonding network that inhibits polymorphism to very high pressures. Chapter 5 of this work documents the compressional behavior of melamine to approximately 36 GPa, utilizing single-crystal X-ray diffraction and Raman spectroscopy experiments to describe the response of the hydrogen bonding network and the potential use of melamine in the design of functional crystals.

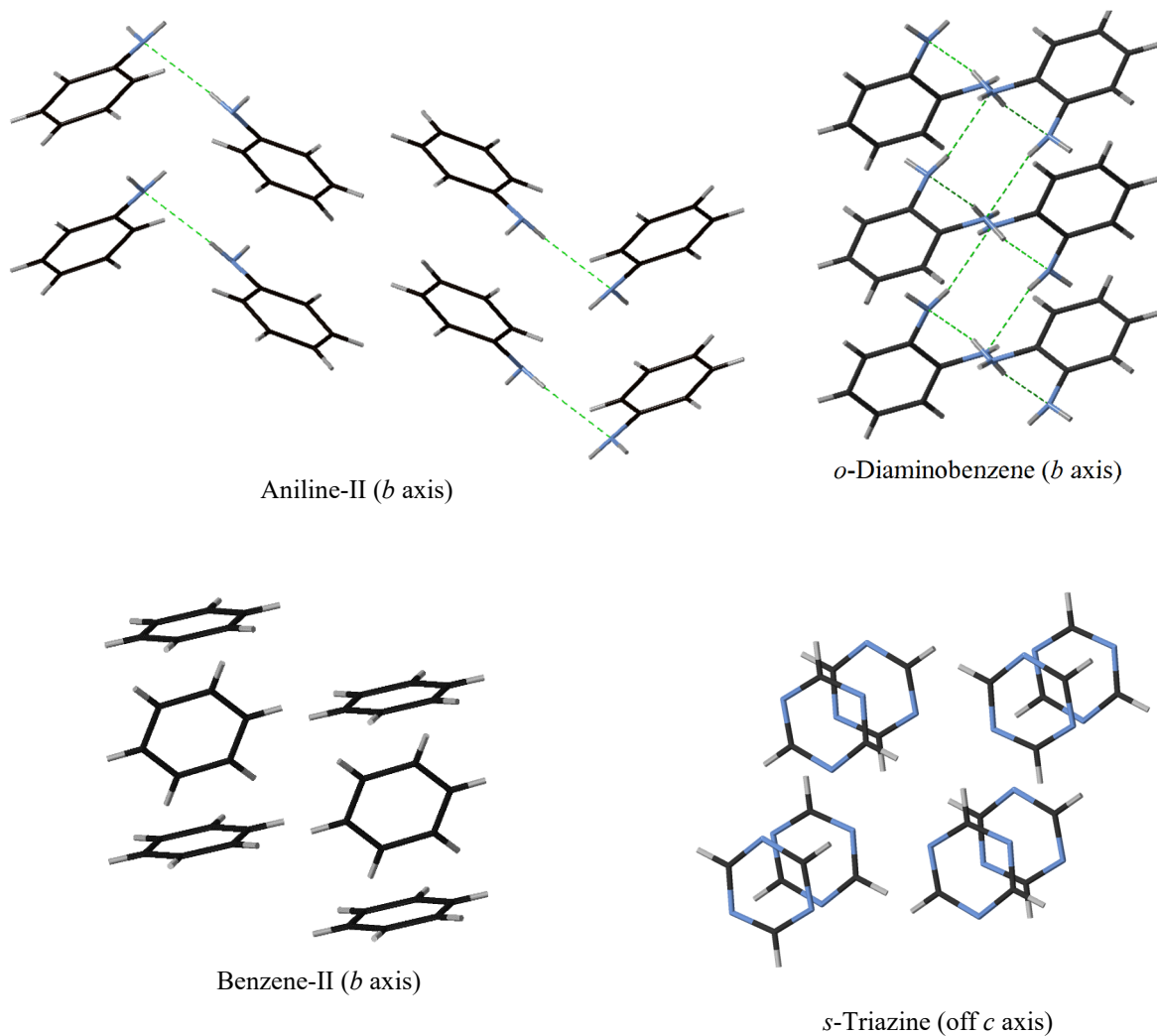


*Figure 1.3. Comparison of aromatic organic crystals, with the viewing axis specified. Aniline and diaminobenzene form networks of N-H...N hydrogen bonds. Benzene forms alternating layers of rings, while *s*-triazine forms stacks of overlapping rings.*

## CHAPTER 2. EXPERIMENTAL METHODS

### 2.1 High Pressure in Diamonds Anvil Cells (DACs)

The overarching theme within this work is to examine the compressional behavior of several crystal structures in relation to the presence or absence of hydrogen bonding. To achieve the high pressures relevant to planetary interiors, diamond anvil cells (DACs) were employed in each subsequent chapter. Diamond anvil cells have been a workhorse of high-pressure experiments and operate on the principle that pressure is generated when force is applied over a unit of area:

$$P = \frac{F}{A}$$

This deceptively simple formula allows for the generation of geologically-relevant pressures at a decidedly non-geological scale; instead of increasing the exerted force, the area to which the force is applied is decreased to produce high pressures. Since its invention in the 1950s, a variety of diamond anvil cell designs have been developed, all of which compress a micron-scale sample between the flat-polished, parallel tips (termed culets) of two gem-quality diamonds [97]. The diamonds are held parallel to one another by backing plates, which in turn are aligned with one another and mounted into the opposing halves of the cell's frame. The opposing halves of the cell are then brought together to generate pressure. This is commonly accomplished by tightening of screws that join the halves of the cell, but also may be accomplished by the action of a pneumatic membrane or gearbox. The geometry and material of the backing plates vary, but must ensure parallelism between the diamonds at high pressures. Similarly, a variety of diamond cuts are available depending on the desired pressure or experimental technique. A schematic of the interior of a diamond anvil cell is shown in Figure 2.1.

Generally, modern diamond anvil cell experiments do not directly compress a sample between the diamonds. Instead, a metal gasket is indented between the diamond culets to approximately 40 microns in thickness, and a hole is drilled in the center of the indentation. This serves as a sealed sample chamber that prevents the loss of the sample, holds in pressure-transmitting media, and prohibits the diamonds from touching one another. Gaskets are typically made of hard metals, such as rhenium or steel, but may also be made of X-ray transparent materials such as beryllium or cubic boron nitride, depending on the desired experiment and cell

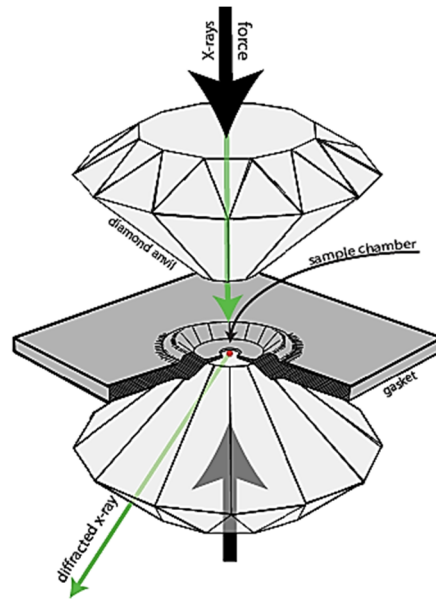


Figure 2.1. Cutaway view of a diamond anvil cell interior. After [mawi.tu-darmstadt.de](http://mawi.tu-darmstadt.de).

geometry. Next, the sample is placed in the center of the gasket hole, along with a pressure calibrant. The sample chamber is then filled with pressure-transmitting media and sealed by bringing the opposing diamonds together into the indentation of the gasket. Pressure can then be increased by bringing the diamonds closer to one another, exerting a large amount of force over the small area of the sample chamber [98].

The force exerted by the opposing diamonds is uniaxial, however, hydrostatic compression is typically desired in high-pressure experiments. Anisotropic stresses, and the resulting unequal strains often decrease the quality of diffraction and spectroscopic peaks, and may result in significantly different phase transition pressures or resulting polymorphs. To avoid this, a pressure transmitting medium is typically used to convert the uniaxial force from the diamonds into homogenous, isotropic pressure around the sample. The choice of pressure medium depends on the pressure range and sample solubility as well as reactivity; noble gases, solvents, or soft solids such as NaCl are popular choices [98, 99]. In the subsequent chapters, helium, neon, and a solution of methanol-ethanol-water were used, depending on the sample. For instance, although helium provides better hydrostaticity than neon, it may diffuse into diamonds or into voids in the sample [7, 100]. Similarly, methanol-ethanol-water mixtures are a convenient pressure medium choice, but are best suited to pressures below 12 GPa and may interact with hydrogen-bonded molecular crystals, altering their compressional behavior [99].

There are several common methods to measure the pressure within a diamond anvil cell: First, the unit cell parameters of a pressure standard (commonly Ag, Au, or MgO) or the pressure transmitting medium (often Ne) can be compared to a known equation of state [98]. Second, the shift in the laser-induced fluorescence for a pressure standard, typically ruby ( $\text{Al}_2\text{O}_3:\text{Cr}^{3+}$ ) or samarium-doped yttrium aluminum garnet ( $\text{Y}_3\text{Al}_5\text{O}_{12}:\text{Sm}^{3+}$ ) may be used. For ruby measurements, pressure determination is made by the redshifted position of the  $R_1$ - $R_2$  spectral lines, which has been calibrated for use up to 180 GPa [101-103]. The ruby-based pressure scale has become one of the most popular methods of pressure determination, and the experiments of the subsequent chapters use this method. Figure 2.2 depicts a typical shift in ruby fluorescence peaks upon pressurization, using pressure data obtained from the experiments in Chapter 5.

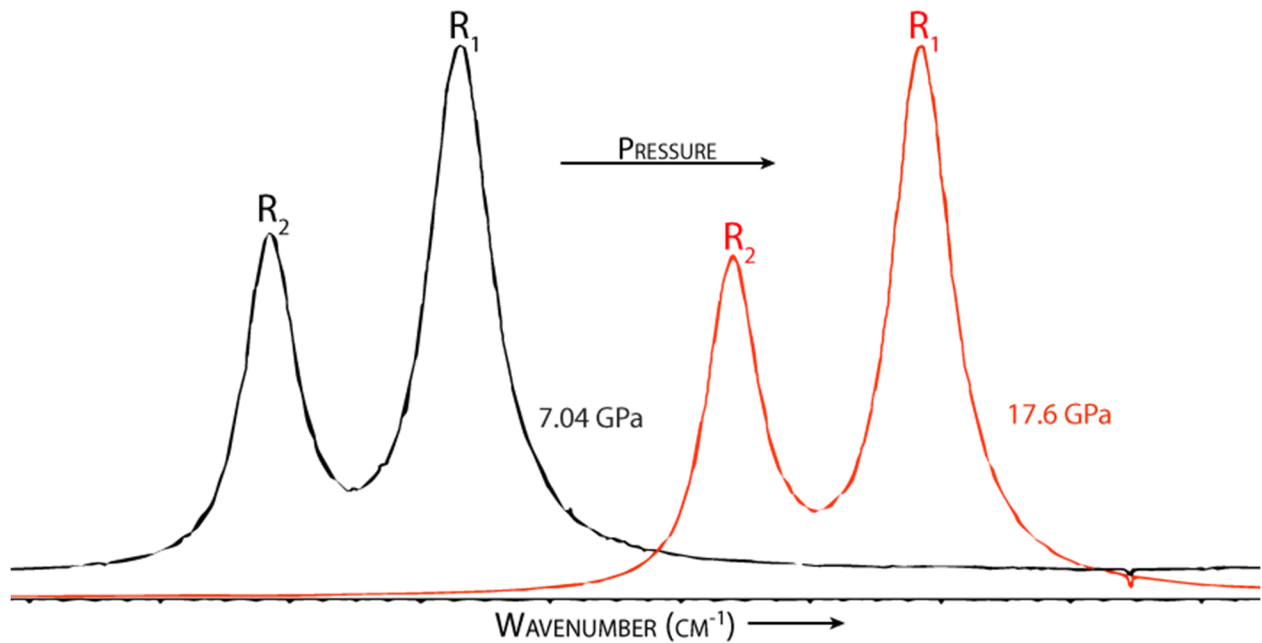


Figure 2.2. Example of ruby fluorescence pressure measurement. The signal is redshifted to higher wavelengths when the ruby is compressed.

## 2.2 Single-Crystal X-Ray Diffraction

X-ray diffraction is often the technique of choice for the determination of crystal structures, and is the most accessible diffraction method for high-pressure experiments. The results of the following chapters are built upon crystal structures determined using high-pressure single-crystal X-ray diffraction, and an introductory look at the mechanism of diffraction and the challenges imposed by diamond anvil cells are given below.

X-ray diffraction is a specific form of coherent X-ray scattering that occurs when X-ray photons interact elastically with the electron density surrounding atoms within a crystalline solid. In particular, diffraction results from the constructive interference of these scattered photons; when collimated X-rays are scattered from parallel lattice planes in a crystal, the resulting in-phase waves act additively to produce a beam of X-ray photons that is recorded as a diffraction peak or spot. This interaction is described in simplest terms by Bragg's Law:

$$n\lambda = 2d_{hkl}\sin\theta$$

where  $\lambda$  is the wavelength of the incident X-ray,  $d_{hkl}$  is the interplanar distance between a family of planes related by  $(hkl)$ ,  $n$  is the order of the diffracted wave, and  $\theta$  is the X-ray angle of incidence. For single-crystal diffraction, the crystal is rotated with respect to the incident X-ray beam to produce an array of diffraction peaks when the values of  $h$ ,  $k$ , and  $l$  are integer values. The position and intensity of these peaks are used to solve for the unit cell parameters and atomic positions within the crystal. In powder diffraction, the sample consists of many randomly oriented crystallites and does not need to be rotated; the array of diffraction peaks produced by each crystallite sum to produce circular patterns, whose intensities are commonly plotted as a function of the  $2\theta$  angle. Although powder diffraction is often a more convenient technique, the random orientation of the many crystallites results in the loss of three-dimensional  $hkl$  information; all symmetry-equivalent points are averaged together, which prevents the identification of individual planes in reciprocal space. As a result, single-crystal diffraction is generally preferred for the purposes of crystal structure solution, and is the technique used in the following chapters. However, powder diffraction is a powerful diagnostic tool to identify known phases (especially in mixed-phase samples) and to determine phase transitions.

For a given peak with Miller indices ( $hkl$ ), its measured intensity is related to the type and position of the scattering atoms by the structure factor:

$$\mathbf{F}(hkl) = \sum_{j=1}^N f_j e^{2\pi i(hx_j + ky_j + lz_j)}$$

where  $f_j$  is the atomic scattering for the  $j$ th atom at coordinates  $(x_j, y_j, z_j)$ . The electron density ( $\rho$ ) is obtained by the inverse Fourier transform:

$$\rho(x, y, z) = \frac{1}{V} \sum_{hkl} |\mathbf{F}(hkl)| e^{i\alpha} e^{-2\pi i(hx_j + ky_j + lz_j)}$$

where  $V$  is the volume of the unit cell,  $|\mathbf{F}(hkl)|$  and  $\alpha$  are the amplitude and phase of the structure factor. However, this definition assumes that there is an infinite set of  $hkl$  values and that the phase of the diffraction peaks is known; instead, real diffraction patterns sets are limited series of peaks whose intensity is directly proportional to  $|\mathbf{F}(hkl)|^2$ , but contains no phase information about the diffracted wave. To work around this phase problem, various techniques have been developed to generate a model crystal structure using the peak intensities collected during an experiment. The predicted structure factors of the model can then be compared against those observed, and the structure model is iteratively refined until the two reasonably match. In the following chapters, the primary method of structure solution is the *direct methods* approach; in this solution, it is assumed that peak intensities contain structural information about individual atoms, which can be represented as increased electron density. Second, it is assumed that the background signal is not negative, which would imply negative electron density. This technique works well for small molecules whose atoms are of similar weights, and in principle does not require any other information about the crystal [104]. Another method implemented in Chapters 3 and 4 is *simulated annealing*, which is an *ab initio* approach that is analogous to heat-annealing a solid or growing a crystal from a melt. In this method, a number of atoms (or molecular units) are chosen and are placed randomly in a starting unit cell. The energy of this system is computed, and from that value a new unit cell is created by modifying the original atomic

positions and lattice parameters. The energy for this new configuration is calculated, and the process repeats until there are minimal differences between the structure factors of the predicted and observed unit cells [105]. With simulated annealing, it is advantageous to seed the starting unit cell with known chemical and structural information to reduce the amount of parameters that can change. As a result, this method works well for organic structures as well as framework minerals where the coordination and bonding environment is well-known.

Once an initial structure solution has been determined, it likely needs to be optimized. However, crystal structure refinement is often less straightforward than the structure solution, and there is no single strategy to apply. Regardless of the method, refinement fine-tuning generally modifies the positions and displacement parameters of atoms in the unit cell, and is performed iteratively until satisfactory agreement is reached [104]. In the following chapters, the *least squares* method was implemented, where the squares of the difference between the observed and predicted structure factors are minimized. This difference is typically described by several measures of confidence, or “residuals” [106, 107]:

$$R_1 = \frac{\sum_{hkl} ||F_{obs}| - |F_{calc}||}{\sum_{hkl} |F_{obs}|}$$

$$wR_2 = \sqrt{\frac{\sum_{hkl} w(|F_{obs}|^2 - |F_{calc}|^2)^2}{\sum_{hkl} w|F_{obs}|^2}}$$

Both of these values represent measures of agreement between the structure model and the observed data, but offer different perspectives on the quality of the refinement. The value of  $R_1$  is determined by how well a structure model matches a *selection* of observed data (often  $F_{obs} > 4\sigma(F_{obs})$ ), and uses no weighting scheme to account for the relative influence of an observation on the resulting refinement. The  $wR_2$  value is usually based on *all* observed data, and the functions being minimized are weighted by a term ( $w$ ) representing the precision of the measurement. There are a variety of weighting schemes depending on the refinement software used, but each attempts to account for statistical uncertainty (in each measured peak intensity) and systematic errors (introduced by the instrument) in the data. Differences between weighting

schemes can make it difficult to compare between structure models, so  $wR_2$  is often used to gauge the internal progress of a refinement. Conversely, the unweighted  $R_1$  value is more commonly used for comparing between two potential structures for the same data [108, 109].

These terms also differ by the refinement against  $|F|^2$  or  $|F|$ . Refinement against  $|F|^2$  holds several advantages: the value of  $|F|^2$  is directly proportional to the intensity of an observed peak, and allows the inclusion of very small or negative intensities (compared to the background signal) in the refinement. Otherwise, these data are arbitrarily excluded to avoid the refinement getting stuck in a ‘false minimum’ [108]. This reduces the volume of data and introduces additional uncertainty; however, if the intensity data are sufficiently strong and complete, either method produces similar results. Both the  $wR_2$  and  $R_1$  values are typically produced at the end of a refinement cycle to allow for thorough determination of the structure’s validity [109, 110].

The introduction of the diamond anvil cell creates additional challenges to solving and refining crystal structures. The sample sizes are small – on the order of 10-30 micrometers in diameter – and there are spatial limitations to the data collection. The incident X-rays are usually oriented along the axis of compression, through the two opposing diamonds (Fig. 2.1), which absorb and diffract some of the beam. The high pressures generated often causes diffraction peaks to smear or broaden, which creates additional uncertainty of unit cell parameters and atomic positions. Additionally, the opening angle geometry of the cell limits the angle of rotation, which decreases the completeness of the data set and reduces the confidence in the solved structure [111, 112]. These difficulties can be mitigated to some extent by increasing the energy of the incident X-rays (often by using a synchrotron light source) and the use of wide opening angle diamonds and backing plates [113, 114]. This is the case in the following chapters, where a synchrotron was used as the primary X-ray source for the high-pressure experiments.

Accurately describing the structural characteristics of hydrogen bonds at high pressures has often proven to be challenging; light-element crystals tend to weakly diffract X-rays at ambient conditions, and hydrogen is an extremely weak X-ray scatterer. For ambient pressure experiments on lab-based X-ray sources, it is common to cool the crystal with liquid nitrogen or helium to reduce the vibrational motion of the atoms and prevent smearing or overlap in the electron density maps. However, high pressure experiments are generally performed at ambient or elevated temperature. Using brilliant X-ray sources such as synchrotrons increases the signal-

to-noise ratio and resolution, but may not be enough to fully resolve hydrogen positions. In these situations, there are two primary ways to include the hydrogen atoms in the crystal structure. If the hydrogen atoms cannot be located in the electron density map but the chemistry of the crystal is well-known, hydrogen atoms can often be placed into the structure using bond length and angle parameters initially determined from neutron diffraction. X-ray diffraction consistently underestimates covalent bond lengths to hydrogen, as the lone electron must account for both the electron density around the hydrogen nucleus and in the hydrogen-donor bond. In neutron diffraction, incident neutrons are scattered by the nuclei of atoms, rather than their electron density; hydrogen has an exceptionally large neutron scattering factor, and accurate hydrogen positions can easily be determined [110]. If the electron density from hydrogen atoms can be located, neutron-diffraction derived restraints may be placed onto a hydrogen atom that allow for some freedom in refinement, but prevent unrealistic bond lengths or unphysical atomic displacement parameters. Both of these methods are used as subsets of the *riding hydrogen* model, where the hydrogen positions and displacements are tied to the atom to which the hydrogen is bonded. This method is used in Chapters 3 and 5 to produce hydrogen bond geometries that are reasonable with regard to those seen in ambient-pressure measurements.

## 2.3 Computational Methods

Computational crystallographic and molecular dynamics methods provide an additional avenue in understanding and interpreting X-ray diffraction data. Simulations can be used to predict the material properties of a given compound, such as the crystal structure, energetic stability, and electronic and magnetic properties. This has been especially useful at high pressures, where the analytical techniques that may be performed in a diamond anvil cell are limited. Theoretical calculations in high-pressure science are used to make predictions where experimental data are unavailable or of poor quality, to provide guidance in planning experiments, and to interpret their results. To supplement and validate the crystal structures obtained from our high-pressure experiments, density functional theory (DFT) calculations were performed in Chapter 4. A brief overview of density functional theory is presented below.

In essence, most modern computational methods make an attempt at solving the Schrödinger equation:

$$\left[ -\frac{\hbar^2}{2m} \nabla^2 + V(r) \right] \psi(r) = E\psi(r)$$

where  $\hbar$  is the reduced Planck constant,  $m$  is the mass of a particle,  $\nabla^2$  is the Laplacian operator,  $V$  is the potential energy,  $\psi$  is the position-dependent wave function, and  $E$  is the total energy in the system. However, an exact solution to this equation is only possible for systems with one electron, such as an individual hydrogen atom or helium ( $\text{He}^+$ ) ion. In cases where there are additional particles (termed “many body systems”), approximations must be made about the system. These approximations begin with a non-relativistic, time-independent version of the Schrödinger equation:

$$\hat{H}\psi = E\psi$$

Where  $\hat{H}$  is the Hamiltonian operator, and  $E$  is the eigenvalue of the Hamiltonian and represents the total energy in the system. With density functional theory, it is assumed that the electron density ( $\rho$ ) determines all of the properties of a system, and can be used to determine the ground state energy:

$$E[\rho] = \langle \psi | \hat{H} | \psi \rangle$$

This allows DFT calculations to sidestep complicated many-body wave functions: although the complexity of the wave function increases with the number of electrons, the electron density has the same number of variables regardless of the size of the system [115, 116].

However, the electrons within a system still interact with one another and with nuclei, and the energy from this interaction (or *exchange correlation*) must be approximated. No exact expression for the exchange correlation function is known, and the differences between approximations of the correlation form the basis for most modelling methods [107, 117, 118]. Although the contribution from the exchange correlation is small compared to that from kinetic and coulombic terms, small variations can cause large differences in predicted chemical reactivity and bonding. As a result, there are a dizzying variety of exchange correlation

functionals to choose from. The applicability and success of the correlation depends on the nature of the system being modeled; in Chapter 4, the vdW-DF-optB88 exchange correlation functional was chosen to account for London dispersion forces and van der Waals interactions in the crystal structure at high pressures [119, 120].

In addition to an exchange correlation potential, a *basis set* for the single-particle wave functions must be chosen. In periodic structures, the wave function may be expressed as a Bloch function, which expresses an electron's wave function as the product of a periodic function and a plane wave:

$$\psi(\mathbf{r}) = e^{i\mathbf{k}\cdot\mathbf{r}}u(\mathbf{r})$$

where  $\mathbf{r}$  is the position,  $u$  is the periodic function, and  $\mathbf{k}$  is the plane wave vector [115]. These plane waves obey periodic boundary conditions, often the unit cell of a crystal, and can be linearly combined to form the electron density. Multiple functions are then sampled over a “mesh” of wave vectors referred to as *k points*, and integrated over the primitive unit cell of the reciprocal lattice, or first Brillouin zone. This forms the basis of the most popular method for periodic structures, the *plane-wave* basis set, which treats each Bloch function as a Fourier series of plane waves whose vectors are also reciprocal lattice vectors [116]. Within Chapter 4 a derivation of the plane-wave method, the *projector augmented wave* (PAW) method, was used. The PAW method describes the electronic structure as sets of plane waves that are independent of atomic nuclei, and makes the calculation more efficient by including pseudopotentials that describe the coulombic interactions of nuclei and core electrons with the valence electrons. As a result, only the valence electron wave functions need to be calculated. Additionally, PAW smooths the valence electron wave functions into a form that can be described by plane wave expansion, reducing the time needed for the calculation [121, 122]. As a result, PAW is a popular and accurate method for determining the electronic structure of crystalline materials.

Although DFT calculations quantify the ground state properties of a system, they can be further used to describe non-equilibrium properties that are dependent on lattice dynamics. Generally, these properties are determined by calculating the energy and stress in a system after a perturbation is introduced, such as the movement of an atom away from the ground state position. When an atom is displaced from its ground state position, the forces on other atoms in

the crystal increase; between bonded atoms, this interaction is spring-like, and propagates as vibrational waves through the lattice structure. Additionally, the motion of atoms in a crystalline lattice can be generally described by harmonic oscillations around the equilibrium atomic positions [123]. The vibrational modes of the lattice (and the quantization of the vibrational energy) are called phonons [123], and are derived from these harmonic approximations. The relation between a phonon's energy and wave vector are dependent on the crystal structure; only certain wave vectors are allowed by a given structure (termed phonon modes), and are defined in terms of the  $k$  points within the first Brillouin zone [115].

As carriers of energy through a solid, phonon calculations are can be used to determine many materials properties, including thermoelastic parameters, electrical resistivity, optical properties, and structural phase transitions [115]. In Chapter 4, two phonon-derived properties are used as diagnostic tools to validate the crystal structure of cristobalite X-I: phonon dispersion curves (also referred to as the phonon band structure) and the phonon density of states. Phonon dispersion curves relate phonon energies (or frequencies) to a wave vector; generally, dispersion curves are used to evaluate if a given crystal structure is dynamically stable. The potential energy

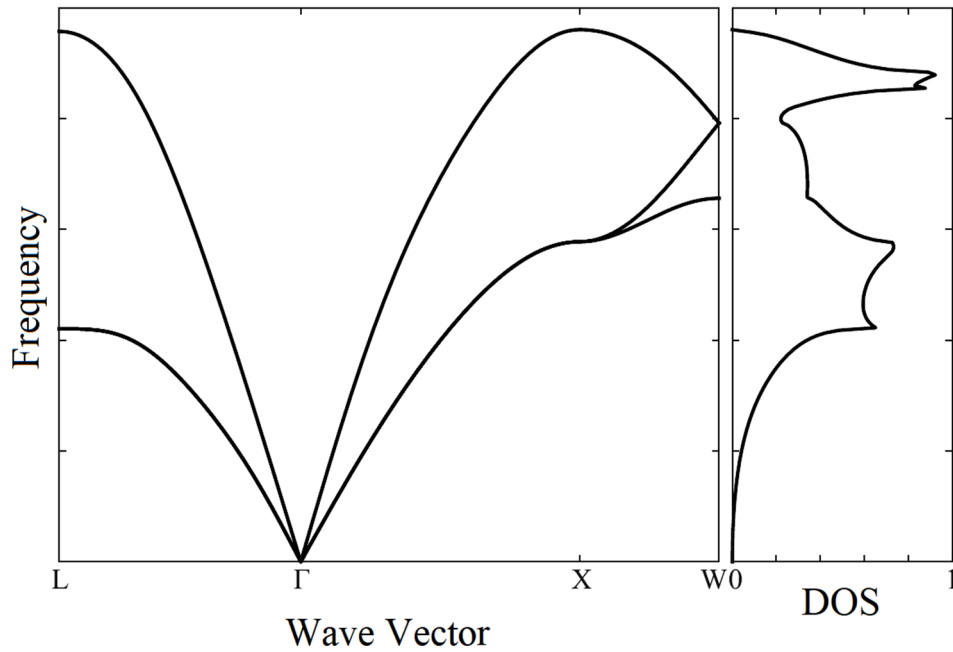
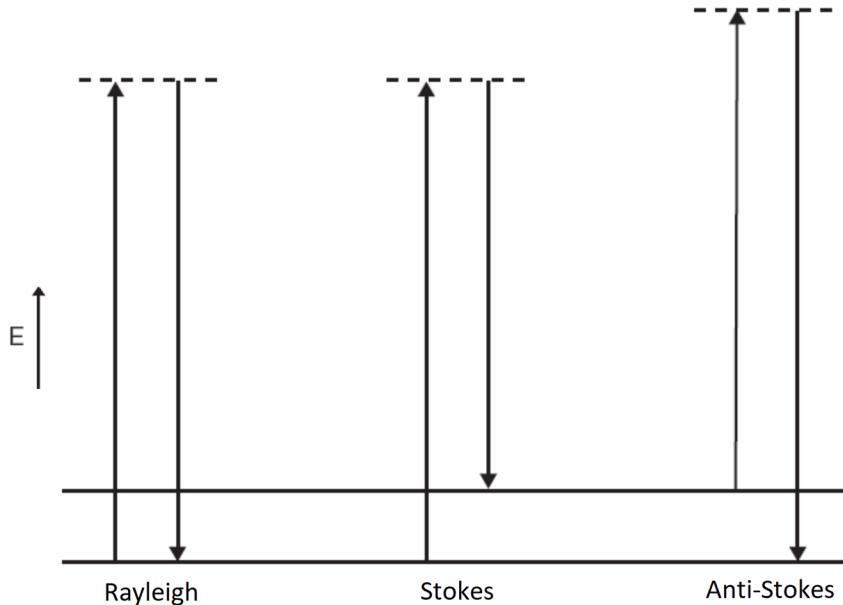


Figure 2.3. Phonon dispersion curves and density of states (DOS) for aluminum. After Togo & Tanaka, 2015.

in a crystal should always increase with any perturbation from displacement of an atom, resulting in a positive frequency. However, if the frequency is negative, the displacement of an atom lowered the energy for the system, and may indicate that the structure is not stable. The phonon density of states provides the number of modes per unit frequency, per unit volume described by the boundary conditions of the Brillouin zone [123]. This translates into describing the number of available energy states that could be occupied, but does not convey information about whether that state *is* occupied. The phonon dispersion and density of states information can be directly compared with X-ray and neutron inelastic scattering, and can be used to predict IR and Raman frequencies.

## 2.4 Raman Spectroscopy

Unlike X-ray diffraction, spectroscopic techniques do not depend on long-range periodicity or crystallinity and are an excellent complementary technique to X-ray diffraction when observing pressure-induced changes in crystal structure. Raman spectroscopy is a type of inelastic photon scattering, where a monochromatic radiation source illuminates the sample and interacts with the atomic vibrations and rotational movement of bonds within a substance. This increases the energy within the molecule, which must release this energy and return to a lower energy configuration [124, 125]. Raman scattering consists of Stokes and Anti-Stokes scattering, where the lower energy configuration is either higher or lower than the original energy state, respectively; generally, Stokes scattering is recorded as part of a Raman spectrum. The energy difference between the energy states is plotted as a function of wavelength, or more commonly, wavenumbers ( $\text{cm}^{-1}$ ). This relaxation shifts the energy of the scattered photons in predictable ways that are attributable to the structure and functional groups present; the position of a Raman band is dependent on the energy difference between the ground state and first excited state for a given bond. The energies of the bond vibrations can be considered spring-like and well-approximated by harmonic oscillators [125], and the frequency of the Raman band depends on the force constant and masses of atoms involved. Lighter atoms and stronger bonds produce higher Raman wavenumber shifts, while heavier atoms and weaker interactions are lower in frequency [124].



*Figure 2.4. Types of photon scattering. Raman scattering encompasses Stokes and Anti-Stokes scattering. After Vandenabeele, 2013.*

As a result, the Raman pattern can be used to identify structural and electronic environments within a compound, which are in turn sensitive to changes in pressure; this can be a powerful investigative technique for exploring phase transitions as well as more subtle changes in bond geometry and electron density. Raman spectroscopy is utilized in Chapter 5 to describe the bonding behavior of melamine near and after its high pressure phase transition, including the rearrangement of the hydrogen bonding network and interactions between neighboring aromatic rings within the crystal.

## CHAPTER 3. HYDROGEN BOND EFFECTS ON COMPRESSIONAL BEHAVIOR OF ISOTYPIC MINERALS: HIGH-PRESSURE POLYMORPHISM OF Be(OH)<sub>2</sub>

Hannah Shelton<sup>1</sup>, Madison C. Barkley<sup>2,3</sup>, Robert T. Downs<sup>3</sup>, Ronald Miletich<sup>4</sup>, and Przemyslaw Dera<sup>1</sup>

<sup>1</sup>Hawai'i Institute of Geophysics and Planetology and Department of Geology and Geophysics, School of Ocean and Earth Science and Technology, University of Hawaii at Mānoa, Hawai'i, 96822

<sup>2</sup>Arizona Historical Society, Phoenix, Arizona 85007

<sup>3</sup>Department of Geosciences, University of Arizona, Tucson, Arizona 85721

<sup>4</sup>Institut für Mineralogie und Kristallographie, Universität Wien, Althanstraße 14, A-1090 Wien

Correspondence: [sheltonh@hawaii.edu](mailto:sheltonh@hawaii.edu)

Published as *Phys. Chem. Minerals* **2016** 43:571-586; doi:10.1007/s00269-016-0818-5

### ABSTRACT

Three isotypic crystals, SiO<sub>2</sub> ( $\alpha$ -cristobalite),  $\epsilon$ -Zn(OH)<sub>2</sub> (wülfingite) and Be(OH)<sub>2</sub> ( $\beta$ -behoite), with topologically identical frameworks of corner-connected tetrahedra, undergo displacive compression-driven phase transitions at similar pressures (1.5-2.0 GPa), but each transition is characterized by a different mechanism resulting in different structural modifications. In this study, we report the crystal structure of the high-pressure  $\gamma$ -phase of beryllium hydroxide and compare it with the high-pressure structures of the other two minerals. In Be(OH)<sub>2</sub>, the transition from the ambient  $\beta$ -behoite phase with the orthorhombic space group  $P2_12_12_1$  and ambient unit cell parameters  $a = 4.5403(4)$  Å,  $b = 4.6253(5)$  Å,  $c = 7.0599(7)$  Å, to the high-pressure orthorhombic  $\gamma$ -polymorph with space group  $Fdd2$  and unit cell parameters (at 5.3(1) GPa)  $a = 5.738(2)$  Å,  $b = 6.260(3)$  Å,  $c = 7.200(4)$  Å takes place between 1.7 and 3.6 GPa. This transition is essentially second order, is accompanied by a negligible volume discontinuity, and exhibits both displacive and reversible character. The mechanism of the phase transition results in a change to the hydrogen bond connectivities and rotation of the BeO<sub>4</sub> tetrahedra.

### 3.1 INTRODUCTION

When a crystal is subjected to stress, its elastic structural response is controlled by the interplay of various interatomic forces. The balance between these forces can have significant effects on polymorphism. Hydrogen bonding within crystal structures can, for instance, affect phase transitions induced by increased pressure and temperature [126, 127], changing the transition conditions from those occurring in anhydrous isomorphs. While most hydrous minerals do not persist in the Earth's interior to great depths, measurable amounts of water can be incorporated into nominally anhydrous mineral structures as structural defects. Significant attention has been recently devoted to the role of hydrogen bonds in dense aluminum silicates and nominally anhydrous dense silicates synthesized at hydrothermal conditions, in the context of possible water storage in the Earth's mantle. Previous experiments have shown that  $(\text{Mg,Fe})_2\text{SiO}_4$  polymorphs derived from olivine can incorporate significant amounts of water within their structures, up to several weight percent [23]. Added water (as  $\text{OH}^-$ ) acts as a structural defect, requiring local charge balance by cation vacancies, or incorporation by crystallographic shearing mechanisms [8, 23]. The inclusion of water has measurable effects on the rheologic and seismic properties of these minerals, although many of these effects are subtle, and not yet well constrained experimentally. Notably, the presence of 1 percent  $\text{H}_2\text{O}$  by weight within ringwoodite at ambient conditions has an effect on the shear modulus comparable to a temperature increase of 800-1000°C in anhydrous ringwoodite [23]. However, many of the physical and thermochemical properties of hydrated mantle minerals have still not been determined. This knowledge is necessary to improve estimates of seismic wave velocities within the mantle, in particular, the seismic anomalies at the 410 and 660 km mantle discontinuities [23].

The variable nature of water incorporation in nominally anhydrous mantle minerals contributes to the difficulty in determining accurate structural and thermoelastic parameters. For instance, synthetic olivines may reach 0.6 to 0.8 percent water by weight at 12-14 GPa and 1200°C, but natural olivines contain comparably little water [23]. It is theorized that the olivine dehydrates upon ascent and pressure release, but the exact structural mechanism of this dehydration is not well understood [23]. The presence of hydrogen in mineral structures often leads to hydrogen-bond specific discontinuities in compressional behavior, related to hydrogen

hopping or hydrogen bond symmetrization. Examples of this behavior include the ice VII-X phase transition in H<sub>2</sub>O [40, 42, 128] and hydrogen bond symmetrization in phase D [29, 30].

Silica polymorphs are of additional importance as nominally anhydrous mantle minerals, given the prevalence of SiO<sub>2</sub> within the Earth's crust and mantle. A variety of SiO<sub>2</sub> polymorphs exists based on different arrangements of SiO<sub>4</sub> tetrahedra and SiO<sub>6</sub> octahedra, depending on pressure and temperature conditions. Pressures below about 9 GPa favor SiO<sub>4</sub> tetrahedra, leading to the formation of lower density phases, including quartz, cristobalite, tridymite, and coesite. At higher pressures, SiO<sub>6</sub> octahedra become energetically preferable, promoting denser structures including stishovite, a CaCl<sub>2</sub>-structured-phase, and seifertite [26, 129]. These silica polymorphs have many corresponding homeotypes in other compounds. For instance,  $\alpha$ -quartz shares the same trigonal structure with GeO<sub>2</sub> and AlPO<sub>4</sub> [129, 130]. The homeotypes usually undergo similar structural transitions as a function of pressure and temperature, and can be used to model the behavior of SiO<sub>2</sub> with consideration of different chemical properties, namely bond lengths and cation sizes [130].

While SiO<sub>2</sub> mineral phases are nominally anhydrous, a significant amount of water (above one weight percent) can be incorporated within the structure of stishovite [3]. Such substitution was demonstrated to affect physical properties, *e.g.* electrical conductivities [25], as well as phase transition pressures [26]. Among the tetrahedral SiO<sub>2</sub> phases, coesite has been reported with appreciable water content [131], and the level of hydration has been demonstrated to affect the conditions of formation of coesite from glass [132], as well as the coesite-quartz phase transformation [131-133].

With such low water content, the effects of hydration are usually subtle, and difficult to reliably constrain. In these cases, structurally related and fully hydrated compounds, if available, can be used to model the effects of water incorporation and the presence of hydrogen bonding in nominally anhydrous compounds. In order to reliably assess the exact role that hydrogen bonding plays in controlling the physical properties and phase relations, a comparative reference system is useful, involving both anhydrous and completely hydrated minerals. The  $\alpha$ -cristobalite phase of SiO<sub>2</sub> forms a structurally isotypic family with two metal hydroxides, behoite (Be(OH)<sub>2</sub>) and wülfingite (Zn(OH)<sub>2</sub>) [75, 134, 135]. The majority of the hydroxides of divalent metals are based on octahedrally coordinated cations in a layered arrangement (*e.g.* brucite-Mg(OH)<sub>2</sub>;

portlandite- $\text{Ca}(\text{OH})_2$ ;  $\text{Sr}(\text{OH})_2$ ;  $\text{Ba}(\text{OH})_2$ ) [136]. These compounds commonly crystallize with hexagonal symmetry, with a  $\text{CdI}_2$ -like structure [127, 134]. Two metal hydroxides of interest in this study,  $\text{Be}(\text{OH})_2$  and  $\text{Zn}(\text{OH})_2$ , possess the same stoichiometry as other divalent metal hydroxides, but exhibit three-dimensional tetrahedral framework structures topologically equivalent to cristobalite, with hydroxyl groups replacing the bridging O atoms. The symmetry of these hydroxide phases, assuming space group  $P2_12_12_1$ , is related, but distinct from,  $\alpha$ -cristobalite's  $P4_12_12$  space group due to framework distortion associated with the presence of  $\text{O}\cdots\text{O}$  hydrogen bonds [137]. The tetrahedral framework arrangements in  $\alpha$ -cristobalite- $\text{SiO}_2$ ,  $\beta$ - $\text{Be}(\text{OH})_2$ , and wülfingite- $\text{Zn}(\text{OH})_2$  are compared with each other in Figure 3.1. These three minerals constitute the basis of the structurally isotypic reference system.

Beryllium hydroxide, the primary compound of focus in this study, is currently known to metastably exhibit four phases at ambient conditions: an amorphous gel, a metastable  $\alpha$ -phase, an orthorhombic  $\beta$ -phase, and a monoclinic phase often observed with the  $\beta$ -phase [138]. During synthesis, alkali addition to a beryllium salt solution produces a gelatinous beryllium hydroxide [139]. Upon dehydration this amorphous product transforms to the metastable tetragonal crystalline polymorph ( $\alpha$ ), which eventually transforms into the stable orthorhombic crystalline  $\beta$ -polymorph, found naturally as the mineral behoite. The fourth phase is a monoclinic polymorph found naturally with the  $\beta$ -phase, known as clinobehoite [140]. When heated to 770 K, behoite incompletely dehydrates, incongruently forming  $\text{H}_2\text{O}$  and a primarily anhydrous  $\text{BeO}$  crystal structure with defects of OH groups coordinated within [141]. In the present study, a natural single crystal of  $\beta$ -behoite was used in a series of single-crystal X-ray diffraction experiments aimed at solving the structure of the high-pressure phase and elucidating its relation to high-pressure polymorphs of  $\text{Zn}(\text{OH})_2$  and  $\alpha$ -cristobalite.

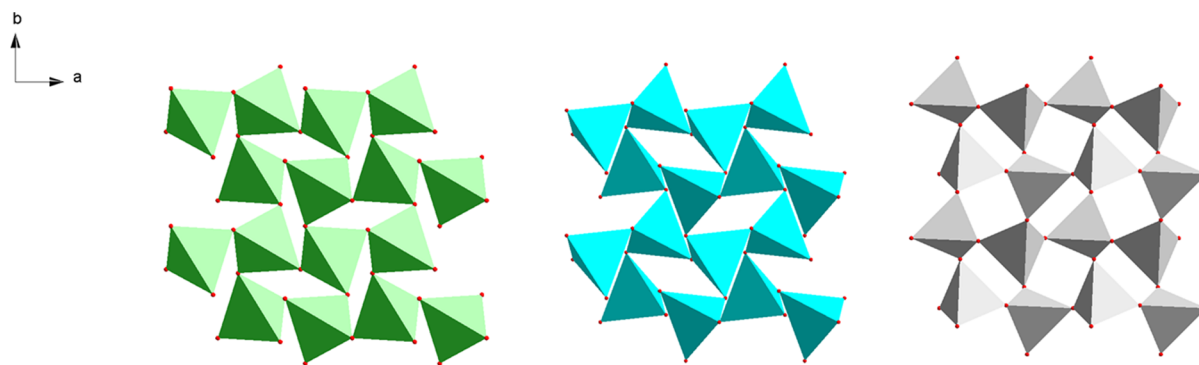


Figure 3.1. From left to right: comparison of  $\text{BeO}_4$ ,  $\text{ZnO}_4$ , and  $\text{SiO}_4$  tetrahedra structures in behoite, wulfingite, and  $\alpha$ -cristobalite.

## 3.2 MATERIALS AND METHODS

All behoite samples used in this study are from Mont St. Hilaire, Quebec, Canada and are in the collection of the RRUFF project (deposition No. R060659). The sample appears as tan colored reticulated groups. The crystals were examined under three distinct experimental conditions. At the University of Arizona, the structure was characterized in air, and within a diamond anvil cell, from atmospheric pressure to 1.70(5) GPa. Another two diamond anvil cell experiments were conducted at Argonne National Laboratory's Advanced Photon Source, at the 13ID-D and 13BM-D beamlines of the GeoSoilEnviro-CARS facility.

### 3.2.1 Ambient X-Ray Diffraction

To properly characterize the starting natural samples used in the experiments an equant, euhedral crystal, approximately  $0.10 \times 0.08 \times 0.05$  mm, was selected and mounted on a Bruker X8 APEX2 CCD X-ray diffractometer equipped with a graphite-monochromatized  $\text{MoK}\alpha$  source (denoted as experiment UA1). X-ray diffraction data were collected to  $2\theta \leq 80^\circ$  with frame widths of  $0.5^\circ$  in  $\omega$  and 90 seconds counting time per frame. Cell refinement and data reduction were completed using the SAINT program, with structure determination and refinement through SHELX97 [142]. The O atom site locations were found using structure-invariant direct methods, while Be and H site locations were found using difference Fourier maps to locate electron densities. In the structure refinement the atomic displacement parameters (ADPs) for Be and O

atoms have been refined anisotropically, whereas ADPs for H atoms were treated as independent isotropic parameters. Summary of the data collection, crystallographic data, and refinement statistics is given in Table 3.1. Unit cell parameters, fractional atomic coordinates and atomic displacement parameters, as well as selected bond lengths and angles of all atoms are listed in Tables 3.2, 3.3, 3.5, 3.6 and 3.7. Symmetry operations are defined in Table 3.4. Hydrogen bond geometry parameters at each pressure are given in Tables 3.8 and 3.9. The data obtained from the ambient pressure experiment are in very good agreement with the earlier combined powder/single crystal study of Stahl et al. [137]. Because the high pressure data sets contained a much smaller number of unique observations (a consequence of the geometrical restrictions imposed by the diamond anvil cell), we limited the number of refined parameters for these sets. Only Be was refined with anisotropic ADPs, with O atoms treated with isotropic approximation, and H atom ADPs were constrained to 120% of the value of corresponding hydroxyl oxygen. The ambient pressure data set served as a test whether such treatment could bias the refined model. The refinement results for the ambient, UA1 data set are reported with both of the above described approaches, and were found to be fully consistent with each other. For each pressure step, the polyhedral volume, tetrahedral angle variance, and mean tetrahedral quadratic elongation were determined using the XtalDraw program [143]. XtalDraw does not calculate estimated standard deviations and these values are not reported here.

### 3.2.2 High Pressure X-Ray Diffraction

The crystal from UA1 was loaded into a four-post diamond anvil cell with a 15:4:1 methanol:ethanol:water pressure medium, which is hydrostatic up to approximately 10 GPa [144]. Pressure in the cell was determined by the fluorescence spectra of included ruby chips [101]. Single crystal intensities were collected on a Picker four-circle diffractometer equipped with MoK $\alpha$  radiation. All accessible data from a sphere of reciprocal space with  $0^\circ \leq 2\theta \leq 60^\circ$  were collected using scans of  $1^\circ$  width, in step increments of  $0.025^\circ$  and 3 seconds per step counting time. Two standard reflections, (-101) and (-112), were measured every 6 hours; no significant variations in the intensities of the standard reflections were observed. Unit cell parameters were measured at 0.50(5), 1.00(5) and 1.70(5) GPa, and a full crystal structure determination was carried out at 1.7(1) GPa, just below the transition pressure.

Additional smaller crystals from the same sample were prepared for synchrotron high-pressure experiments at the APS. Experiments were conducted at the insertion device station 13ID-D and bending magnet 13BM-D station of the GSECARS facility. For use at both stations, a behoite crystal with dimensions of approximately  $0.01 \times 0.015 \times 0.005$  mm was loaded into a symmetric Princeton-type piston-cylinder diamond anvil cell. Diamond anvils with culets of 0.300 mm were mounted on asymmetric backing plates: a backing plate of cubic boron nitride was placed towards the X-ray source, while a backing plate of tungsten carbide was placed towards the detector. A rhenium gasket with initial thickness of 0.250 mm, pre-indented to 0.031 mm, was used for sample containment. For experiments conducted at the GSECARS facility, neon was used as the pressure medium. As with the previous experiment, pressure in the cell was determined by the fluorescence spectra of ruby spheres included in the cell, which was measured at each pressure point both before and after the X-ray data collection [101]. A monochromatic beam with incident energy of 37 keV was focused with a pair of Kirkpatrick-Baez mirrors to a spot of  $0.003 \times 0.005$  mm at 13ID-D and  $0.005 \times 0.015$  at 13BM-D. Diffraction images were collected using a MAR165 Charge Coupled Device (CCD) detector, placed at a sample-to-detector distance of approximately 200 mm. At the 13ID-D station, the sample cell was rotated about the vertical axis of the instrument, from  $-25^\circ$  to  $25^\circ$ , with an exposure time of twenty-five seconds for this range. Step scans, with rotation increments of  $1^\circ$ , were also performed at each step in pressure. At the 13BM-D station, step scans were performed with rotations of 10 seconds per degree. Data collection was performed following the same procedure as previously described by Dera et al. [75, 145].

At the 13ID-D station, single crystal X-ray diffraction data were collected at four pressures: 7.9(1), 10.6(1), 8.6(1) GPa and 5.3(1) GPa, with the last two points collected on decompression. The  $\beta$ - $\gamma$  phase transition was clearly visible in the single crystal diffraction patterns, as shown in Figure 3.2, and took place between 0.3(1) and 7.7(1) GPa based upon the resulting diffraction patterns. The diffraction images were analyzed using the ATREX IDL software package [145, 146]. Full structure determination was carried out only with the data collected at 5.3(1) GPa. The remaining pressure points, including data from the 13BM-D station up to 30.1(1) GPa, were used for unit cell parameter determination. At 5.3(1) GPa the data was collected at three orientations of the diamond cell, differing by rotation about the cell axis ( $\chi$ -rotation) by 120 degrees.



Table 3.1. Data collection and refinement details.

<b><u>UA1</u></b> (ambient pressure)		<b><u>UA3</u></b> (1.03(5) GPa)	
No. of reflections collected	2626	No. of reflections collected	319
No. of independent reflections	806	No. of independent reflections	139
$R_{\text{int}}$	0.0394	$R_{\text{int}}$	0.058
$R[F^2 > 4\sigma(F^2)]$	0.0571	$R[F^2 > 4\sigma(F^2)]$	0.047
$wR(F^2)$	0.1452	$wR(F^2)$	0.125
Goodness-of-fit	1.076	Goodness-of-fit	1.30
No. of parameters refined	24	No. of parameters refined	24
No. of restraints used	2	No. of restraints used	2
<b><u>UA1_0</u></b> (ambient pressure, no ADP constraints)		<b><u>UA4</u></b> (1.74(5) GPa)	
No. of reflections collected	2358	No. of reflections collected	327
No. of independent reflections	651	No. of independent reflections	148
$R_{\text{int}}$	0.0387	$R_{\text{int}}$	0.0472
$R[F^2 > 4\sigma(F^2)]$	0.0416	$R[F^2 > 4\sigma(F^2)]$	0.062
$wR(F^2)$	0.1043	$wR(F^2)$	0.1396
Goodness-of-fit	1.121	Goodness-of-fit	1.273
No. of parameters refined	36	No. of parameters refined	24
No. of restraints used	0	No. of restraints used	2
<b><u>UA2</u></b> (0.53(5) GPa)		<b><u>IDD5</u></b> (5.3(1) GPa)	
No. of reflections collected	317	No. of reflections collected	157
No. of independent reflections	141	No. of independent reflections	99
$R_{\text{int}}$	0.064	$R_{\text{int}}$	0.1177
$R[F^2 > 4\sigma(F^2)]$	0.047	$R[F^2 > 4\sigma(F^2)]$	0.0686
$wR(F^2)$	0.11	$wR(F^2)$	0.1507
Goodness-of-fit	1.164	Goodness-of-fit	1.331
No. of parameters refined	24	No. of parameters refined	20
No. of restraints used	2	No. of restraints used	2

Table 3.2. Unit cell parameters as a function of pressure. Behoite (0 - 1.74(5) GPa) has space group  $P2_12_12_1$ . The high-pressure polymorph (3.6(1) - 30.1(1) GPa) has space group  $Fdd2$ . Values noted with “\*” have been transformed to the low-pressure monoclinic setting.

P (GPa)	Name	a (Å)	b (Å)	c (Å)	V(Å <sup>3</sup> )
10 <sup>-4</sup>	UA1	4.5403(4)	4.6253(5)	7.0599(7)	148.26(3)
10 <sup>-4</sup>	UA1_0	4.5403(4)	4.6253(5)	7.0599(7)	148.26(3)
0.53(5)	UA2	4.5288(4)	4.6196(5)	7.0554(7)	147.61(3)
1.03(5)	UA3	4.5034(4)	4.5977(5)	7.0442(7)	145.85(3)
1.74(5)	UA4	4.4748(4)	4.5706(5)	7.0358(7)	143.90(2)
3.6(1)	BMD1	5.819(4)	6.349(4)	7.237(6)	267.4(3)
5.3(1)	IDD5	5.738(2)	6.260(3)	7.200(4)	258.7(2)
7.9(1)	IDD2	5.660(3)	6.160(3)	7.151(4)	249.3(2)
8.6(1)	IDD4	5.642(4)	6.132(4)	7.139(5)	246.9(3)
10.6(1)	1DD3	5.610(4)	6.084(3)	7.107(4)	242.6(3)
15.2(1)	BMD2	5.559(12)	5.961(11)	7.002(18)	232.0(9)
19.3(1)	BMD3	5.518(10)	5.878(10)	6.949(10)	225.5(6)
23.7(1)	BMD4	5.480(8)	5.815(8)	6.863(10)	218.8(5)
27.5(1)	BMD5	5.442(10)	5.763(10)	6.797(10)	213.2(6)
30.1(1)	BMD6	5.420(10)	5.728(10)	6.766(10)	210.1(6)
<hr/>					
3.6(1)	BMD1*	4.306(5)	4.306(5)	7.237(6)	134.2(6)
5.3(1)	IDD5*	4.246(2)	4.246(2)	7.200(4)	129.8(4)
7.9(1)	IDD2*	4.183(4)	4.183(4)	7.151(4)	125.1(4)
8.6(1)	IDD4*	4.166(6)	4.166(6)	7.139(5)	123.9(6)
10.6(1)	1DD3*	4.138(5)	4.138(5)	7.107(4)	121.7(6)
15.2(1)	BMD2*	4.075(16)	4.075(16)	7.002(18)	116(2)
19.3(1)	BMD3*	4.031(16)	4.031(16)	6.949(10)	112(1)
23.7(1)	BMD4*	3.995(11)	3.995(11)	6.863(10)	109(1)
27.5(1)	BMD5*	3.963(14)	3.963(14)	6.797(10)	107(1)
30.1(1)	BMD6*	3.943(14)	3.943(14)	6.766(10)	105(1)

Table 3.3. Fractional Atomic Coordinates and Atomic Displacement Parameters.

Name	Atom	x	y	Z	U <sub>eq</sub>
UA1	Be	0.302(6)	0.7078(5)	0.6265(3)	0.011(1)
	O1	0.1921(3)	0.1050(3)	0.426(2)	0.012(1)
	O2	0.1570(3)	0.4218(3)	0.7314(2)	0.012(1)
	H2	0.339(6)	0.447(6)	0.779(4)	0.011(1)
	H1	0.274(6)	0.81(5)	0.555(4)	0.011(1)
UA1_0	Be	0.303(4)	0.7084(4)	0.6265(3)	0.011(1)
	O1	0.1923(2)	0.1052(3)	0.426(2)	0.012(1)
	O2	0.1569(2)	0.4217(2)	0.7313(2)	0.012(1)
	H2	0.326(6)	0.422(6)	0.775(7)	0.018(1)
	H1	0.274(6)	0.69(4)	0.556(5)	0.025(1)
UA2	Be	0.31(2)	0.706(3)	0.6261(9)	0.023(7)
	O1	0.1929(9)	0.107(2)	0.422(5)	0.017(1)
	O2	0.1573(8)	0.425(2)	0.7316(5)	0.014(1)
	H2	0.35(1)	0.44(3)	0.771(7)	0.016(1)
	H1	0.266(1)	0.09(1)	0.547(8)	0.016(1)
UA3	Be	0.32(2)	0.705(4)	0.6273(9)	0.021(9)
	O1	0.194(1)	0.107(2)	0.422(5)	0.014(1)
	O2	0.160(1)	0.423(3)	0.7322(5)	0.013(1)
	H2	0.34(1)	0.52(2)	0.779(8)	0.016(1)
	H1	0.28(2)	0.09(1)	0.545(8)	0.016(1)
UA4	Be	0.30(2)	0.709(5)	0.628(1)	0.03(1)
	O1	0.196(1)	0.99(3)	0.418(5)	0.015(1)
	O2	0.161(1)	0.418(3)	0.7317(5)	0.013(1)
	H2	0.31(1)	0.56(2)	0.769(9)	0.015(1)
	H1	0.28(2)	0.11(1)	0.541(9)	0.015(1)
IDD5	Be	0.0000	0.0000	0.189(1)	0.009(2)
	O	0.175(4)	0.2096(5)	0.316(1)	0.011(1)
	H	-0.5(1)	0.32(1)	0.27(1)	0.00(1)

Table 3.4. Definitions of Symmetry Operations.

Atom	Symmetry Operation
\$1	-x, y+1/2, -z+1/2
\$2	-x+1/2, -y+1, z+1/2
\$3	-x, y+1/2, -z+3/2
\$4	-x, y-1/2, -z+1/2
\$5	-x+1/2, -y+1, z-1/2
\$6	-x, y-1/2, -z+3/2

### 3.3 RESULTS

#### 3.3.1 Structural Evolution

The single crystal refinement of the natural  $\beta$ -behoite sample at ambient conditions yielded a unit cell of  $a = 4.5403(4)$  Å,  $b = 4.6253(5)$  Å,  $c = 7.0599(7)$  Å, with space group  $P2_12_12_1$ , which is in agreement with the unit cell (in a different setting) of [137]. The structure is characterized by a three dimensional tetrahedral framework of corner-sharing  $\text{Be}(\text{OH})_4$  tetrahedra. At low pressures, there are two unique hydroxyl groups, which is consistent with the findings of [150], who observed four Raman active libration modes (two for each independent hydroxyl group) for  $\beta$ - $\text{Be}(\text{OH})_2$ . The polyhedral volume at ambient conditions is  $2.400$  Å<sup>3</sup>, the tetrahedral angle variance is  $5.5431^\circ$ , and the mean tetrahedral quadratic elongation is  $1.0014$  Å. At ambient conditions (UA1), two distinct hydrogen bonds exist between  $\text{O1—H1}_{\$1}\cdots\text{O2}_{\$1}$  and  $\text{O2—H2}\cdots\text{O1}_{\$2}$ , where the  $\$1$  and  $\$2$  symmetry operations are defined in Table 3.4. The donor-acceptor distance and donor-host-acceptor triad are  $2.861(2)$  Å and  $148(3)^\circ$  for  $\text{O1—H1}_{\$1}\cdots\text{O2}_{\$1}$ , and  $2.909(2)$  Å and  $159(3)^\circ$  for  $\text{O2—H2}\cdots\text{O1}_{\$2}$ . Our terminology for naming the geometric parameters of hydrogen bond follows the convention described by Gilli and Gilli [1]. The average length of these hydrogen bonds ( $\text{H1}\cdots\text{O2}$  and  $\text{H2}\cdots\text{O1}_{\$2}$ ) is approximately  $2.07(4)$  Å. At ambient conditions, the length of the hydroxyl bonds for  $\text{O1—H1}_{\$1}$  and  $\text{O2—H2}$  were found to be  $0.88(3)$  and  $0.90(3)$  Å, approximately equal to previously calculated bond lengths [136]. X-ray based methods are well known to underestimate the bond lengths involving hydrogen due to the asymmetric distribution of electron density [2]. In order to assure that this bond length stays within physically reasonable limits, in all high-pressure refinements we used an anti-bumping constraint (DFIX command in SHELX97), restraining the O-H bonding distances to remain within  $0.95\pm 0.05$  Å limits. To demonstrate that this approach does not negatively affect refinement, the ambient data are presented both with and without this additional restraint.

Table 3.5. Anisotropic displacement parameters of beryllium.

	<b>U11</b>	<b>U22</b>	<b>U33</b>	<b>U23</b>	<b>U13</b>	<b>U12</b>
<b>UA1</b>	0.012(1)	0.011(1)	0.011(1)	0.00(1)	0.00(1)	0.00(1)
<b>UA1_0</b>	0.011(1)	0.011(1)	0.010(1)	0.00(1)	-0.01(1)	-0.01(1)
<b>UA2</b>	0.012(3)	0.05(2)	0.011(3)	-0.004(4)	-0.002(2)	0.00(5)
<b>UA3</b>	0.012(3)	0.04(3)	0.011(3)	-0.006(4)	-0.002(2)	0.005(6)
<b>UA4</b>	0.011(3)	0.06(3)	0.014(2)	-0.002(6)	-0.004(3)	-0.005(7)
<b>IDD5</b>	0.008(3)	0.011(4)	0.008(6)	0.00(1)	0.00(1)	0.001(1)

Table 3.6. Bond Distances ( $\text{\AA}$ ): UA1, UA1\_0, UA2, UA4, IDD5.

<b><u>UA1</u></b>		<b><u>UA3</u></b>	
Be(1)-O(2)	1.622(3)	Be(1)-O(2)	1.60(2)
Be(1)-O(1)#1	1.634(3)	Be(1)-O(1)#1	1.62(2)
Be(1)-O(1)#2	1.640(3)	Be(1)-O(1)#2	1.633(9)
Be(1)-O(2)#3	1.646(3)	Be(1)-O(2)#3	1.65(2)
O(1)-Be(1)#4	1.634(3)	O(1)-Be(1)#4	1.62(2)
O(1)-Be(1)#5	1.640(3)	O(1)-Be(1)#5	1.633(9)
O(2)-Be(1)#6	1.646(3)	O(2)-Be(1)#6	1.65(2)
O(2)-H(2)	0.90(3)	O(2)-H(2)	0.97(6)
<b><u>UA1_0</u></b>		<b><u>UA4</u></b>	
Be(1)-O(2)	1.624(2)	Be(1)-O(2)	1.63(2)
Be(1)-O(1)#1	1.635(2)	Be(1)-O(2)#1	1.62(2)
Be(1)-O(1)#2	1.637(2)	Be(1)-O(1)#2	1.63(2)
Be(1)-O(2)#3	1.645(2)	Be(1)-O(1)#3	1.64(1)
O(1)-Be(1)#4	1.635(2)	O(1)-Be(1)#4	1.63(2)
O(1)-Be(1)#5	1.637(2)	O(1)-Be(1)#5	1.64(1)
O(2)-Be(1)#6	1.644(2)	O(2)-Be(1)#6	1.62(2)
O(2)-H(2)	0.83(3)	O(2)-H(2)	0.96(6)
<b><u>UA2</u></b>		<b><u>IDD5</u></b>	
Be(1)-O(2)	1.60(1)	Be(1)-O(1)	1.604(7)
Be(1)-O(1)#1	1.626(8)	Be(1)-O(1)#1	1.604(7)
Be(1)-O(1)#2	1.63(1)	Be(1)-O(1)#2	1.620(6)
Be(1)-O(2)#3	1.66(1)	Be(1)-O(1)#3	1.620(6)
O(1)-Be(1)#4	1.626(8)	O(1)-Be(1)#4	1.620(6)
O(1)-Be(1)#5	1.63(1)	O(1)-H(1)	0.86(5)
O(2)-Be(1)#6	1.66(1)		
O(2)-H(2)	0.90(5)		

Table 3.7. Bond angles (°): UA1, UA2, UA4, IDD5.

**UA1**

O(2)-Be(1)-O(1)#1	108.4(1)
O(2)-Be(1)-O(1)#2	108.8(1)
O(1)#1-Be(1)-O(1)#2	111.4(1)
O(2)-Be(1)-O(2)#3	113.3(1)
O(1)#1-Be(1)-O(2)#3	107.5(1)
O(1)#2-Be(1)-O(2)#3	107.5(1)
Be(1)#4-O(1)-Be(1)#5	125.8(1)
Be(1)-O(2)-Be(1)#6	125.8(1)
Be(1)-O(2)-H(2)	113(2)
Be(1)#6-O(2)-H(2)	109(2)

**UA1\_0**

O(2)-Be(1)-O(1)#1	108.3(1)
O(2)-Be(1)-O(1)#2	108.8(1)
O(1)#1-Be(1)-O(1)#2	111.42(1)
O(2)-Be(1)-O(2)#3	113.24(1)
O(1)#1-Be(1)-O(2)#3	107.55(1)
O(1)#2-Be(1)-O(2)#3	107.60(1)
Be(1)#4-O(1)-Be(1)#5	125.86(9)
Be(1)-O(2)-Be(1)#6	125.84(8)
Be(1)-O(2)-H(2)	114(2)
Be(1)#6-O(2)-H(2)	108.5(2)

**UA2**

O(2)-Be(1)-O(1)#1	110(1)
O(2)-Be(1)-O(1)#2	109.0(5)
O(1)#1-Be(1)-O(1)#2	111.2(5)
O(2)-Be(1)-O(2)#3	113.3(4)
O(1)#1-Be(1)-O(2)#3	106.9(6)
O(1)#2-Be(1)-O(2)#3	106.8(8)
Be(1)#4-O(1)-Be(1)#5	126.5(7)
Be(1)-O(2)-Be(1)#6	126.3(3)
Be(1)-O(2)-H(2)	116(8)
Be(1)#6-O(2)-H(2)	110(6)

**UA3**

O(2)-Be(1)-O(1)#1	109.3(6)
O(2)-Be(1)-O(1)#2	110(1)
O(1)#1-Be(1)-O(1)#2	110.6(5)
O(2)-Be(1)-O(2)#3	113.8(5)
O(1)#1-Be(1)-O(2)#3	107(1)
O(1)#2-Be(1)-O(2)#3	106.2(6)
Be(1)#4-O(1)-Be(1)#5	126.7(7)
Be(1)-O(2)-Be(1)#6	125.6(4)
Be(1)-O(2)-H(2)	94(7)
Be(1)#6-O(2)-H(2)	120(5)

**UA4**

O(2)-Be(1)-O(2)#1	113.5(6)
O(2)-Be(1)-O(1)#2	109.6(7)
O(2)#1-Be(1)-O(1)#2	108(1)
O(2)-Be(1)-O(1)#3	107(1)
O(2)#1-Be(1)-O(1)#3	107.4(7)
O(1)#2-Be(1)-O(1)#3	111.0(6)
Be(1)#4-O(1)-Be(1)#5	124.8(8)
Be(1)-O(2)-Be(1)#6	124.4(5)
Be(1)-O(2)-H(2)	78(6)
Be(1)#6-O(2)-H(2)	126(4)

**IDD5**

O(1)-Be(1)-O(1)#1	110.3(7)
O(1)-Be(1)-O(1)#2	103.6(1)
O(1)#1-Be(1)-O(1)#2	112.8(1)
O(1)-Be(1)-O(1)#3	112.8(1)
O(1)#1-Be(1)-O(1)#3	103.6(1)
O(1)#2-Be(1)-O(1)#3	113.9(7)
Be(1)-O(1)-Be(1)#4	119.4(2)
Be(1)-O(1)-H(1)	113(5)
Be(1)#4-O(1)-H(1)	118(6)

Table 3.8. Hydrogen Bonding Distances (Å): UA1, UA2, UA4, IDD5.

<b><u>UA1</u></b>		<b><u>UA3</u></b>	
H1 - O2	2.08(3)	H1 - O2	2.08(7)
H2 - O1_\$2	2.06(3)	H2 - O1_\$2	2.13(8)
H2 - O1_\$3	2.67(3)	H2 - O1_\$3	2.4(1)
O1 - H1_\$1	0.88(3)	O1 - H1_\$1	0.93(7)
O2 - H2	0.90(3)	O2 - H2	0.97(6)
O1 - O2_\$1	2.861(2)	O1 - O2_\$1	2.86 (2)
O2 - O1_\$2	2.909(2)	O2 - O1_\$2	2.889(6)
O2 - O1_\$3	2.652(2)	O2 - O1_\$3	2.63(2)
<b><u>UA1_0</u></b>		<b><u>UA4</u></b>	
H1 - O2	2.08(2)	H1 - O2	2.03(7)
H2 - O1_\$2	2.05(2)	H2 - O1_\$2	2.32(9)
H2 - O1_\$3	2.67(3)	H2 - O1_\$3	2.22(9)
O1 - H1_\$1	0.88(2)	O1 - H1_\$1	0.94(6)
O2 - H2	0.90(2)	O2 - H2	0.96(6)
O1 - O2_\$1	2.861(2)	O1 - O2_\$1	2.79(2)
O2 - O1_\$2	2.909(2)	O2 - O1_\$2	2.875(7)
O2 - O1_\$3	2.652(2)	O2 - O1_\$3	2.66(2)
<b><u>UA2</u></b>		<b><u>IDD5</u></b>	
H1 - O2	2.08(7)	H1 - O1	0.86(5)
H2 - O1_\$2	2.06(5)	H1 - O1_\$1	2.11(6)
H2 - O1_\$3	2.7(1)	O1 - O1_\$1	2.892(3)
O1 - H1_\$1	0.93(7)		
O2 - H2	0.90(5)		
O1 - O2_\$1	2.88(1)		
O2 - O1_\$2	2.908(5)		
O2 - O1_\$3	2.63(1)		

Table 3.9. Hydrogen Bonding Angles (°): UA1, UA2, UA4, IDD5.

<b><u>UA1</u></b>		<b><u>UA3</u></b>	
O1 - H1_\$1 - O2_\$1	148(3)	O1 - H1_\$1 - O2_\$1	140(5)
O2 - H2 - O1_\$2	159(3)	O2 - H2 - O1_\$2	134(9)
O2 - H2 - O1_\$3	79(2)	O2 - H2 - O1_\$3	93(6)
<b><u>UA1_0</u></b>		<b><u>UA4</u></b>	
O1 - H1_\$1 - O2_\$1	150(3)	O1 - H1_\$1 - O2_\$1	137(5)
O2 - H2 - O1_\$2	160(3)	O2 - H2 - O1_\$2	116(8)
O2 - H2 - O1_\$3	80(2)	O2 - H2 - O1_\$3	106(6)
<b><u>UA2</u></b>		<b><u>IDD5</u></b>	
O1 - H1_\$1 - O2_\$1	143(5)	O1 - H1 - O1_\$1	152(8)
O2 - H2 - O1_\$2	157(6)		
O2 - H2 - O1_\$3	78(7)		

Interestingly, the crystal structure determinations at elevated pressures, but below the transition point (experiments UA2, UA3, UA4) indicate a slight rearrangement of the hydrogen bonding pattern, without a change in space group. At ambient pressure the H2 hydrogen atom (with the symmetry code H2\_\$4) has a well-defined single donor (O2) and acceptor (O1\_\$2). The two next nearest neighboring O atoms, O1\_\$3 and O1 are located 2.53(3) Å and 2.67(3) Å away, much farther than the typical hydrogen bonding distance, at very acute O-H···O angles of 79(2) and 87(2) degrees, as shown in Figure 3.4. At 0.53(5) GPa, this arrangement is maintained. Both the hydrogen bond H···O distances, as well as the contacts to the next neighbor O atoms, remain unchanged within the experimental uncertainties. However, at 1.03(5) GPa, the hydrogen position is significantly shifted towards O1\_\$3. At this pressure the H2···O1\_\$3 distance is reduced to 2.4(1) Å, while the original H-bond stretches as H2···O1\_\$2 increases to 2.13(8) Å. This trend towards hydrogen bond bifurcation continues at 1.74(5) GPa, where the H···O distances become 2.22(7) and 2.32(7) Å, and the corresponding angles 116(6) and 106(5) degrees, respectively, as illustrated in Figure 3.4. At this point, the H1 hydrogen bond length, 2.03(6) Å, with an O-H···O angle of 137(4) degrees, differs only slightly from its ambient value. The Be(OH)<sub>4</sub> tetrahedron remains rigid, with a polyhedral volume at this pressure of 2.2122 Å<sup>3</sup>. The mean quadratic elongation for the BeO<sub>4</sub> tetrahedra is 1.0015 Å, and the tetrahedral angle variance is 6.1329°, similar to ambient parameters. Within the BeO<sub>4</sub> tetrahedra at 1.74(5) GPa,

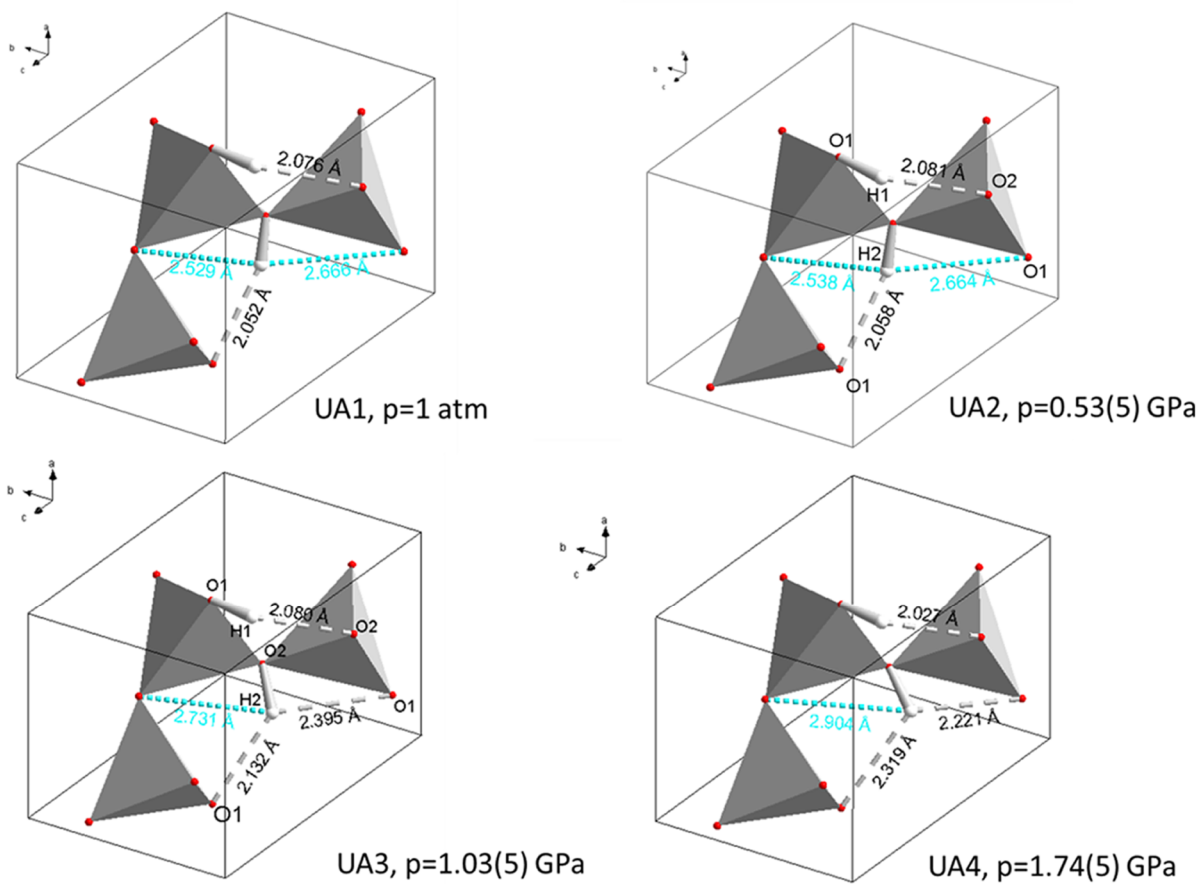


Figure 3.3. Bifurcation of the hydrogen bonds in  $\text{Be}(\text{OH})_2$  with pressure within the  $\beta$ -phase.

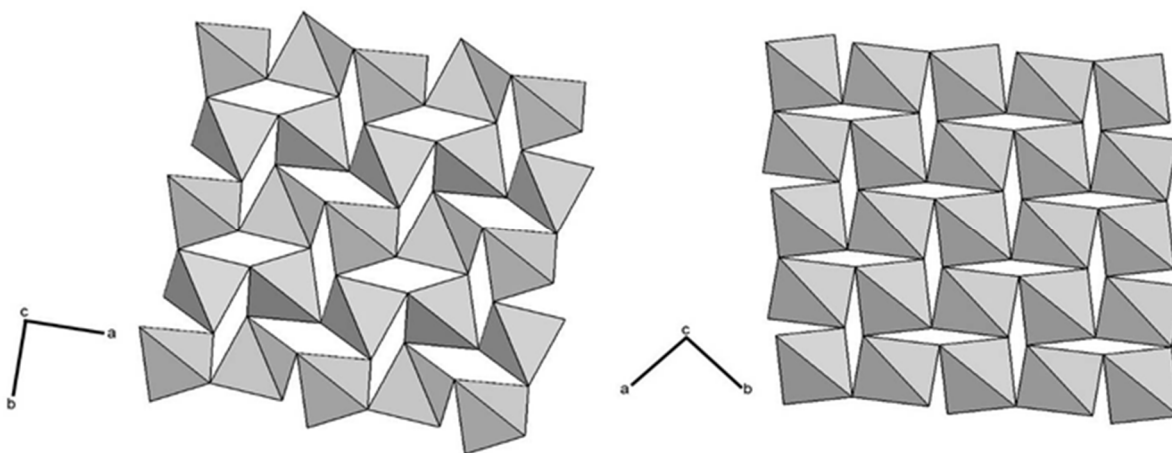


Figure 3.4. Rotation of  $\text{Be}(\text{OH})_2$  tetrahedra between low- and high-pressure phases.

the average Be—O bond distance is 1.626(6) Å, very similar to ambient conditions [137]. The average Be-O-Be bond angle is 126.2(6)° which is also very close to established ambient values. At 1.05(4) GPa, the comparable Si-O-Si bond angle in  $\alpha$ -cristobalite is 140.4(4)° [151]. The bond angles between the BeO<sub>4</sub> tetrahedra at this pressure are more similar to the ambient Zn-O-Zn bond angle in  $\epsilon$ -wulfingite, which is approximately 120°. Upon further compression, the stretched and bifurcated H<sub>2</sub> bond breaks, accompanying the transformation to the  $\gamma$ -phase.

At 5.3(1) GPa, the  $\gamma$ -phase of Be(OH)<sub>2</sub> has an orthorhombic structure with space group *Fdd2*, and unit cell parameters  $a = 5.738(2)$  Å,  $b = 6.260(3)$  Å,  $c = 7.200(4)$  Å,  $V = 258.7(2)$  Å<sup>3</sup> and  $Z = 8$ . At this pressure, the polyhedral volume is 2.1321 Å<sup>3</sup>, the mean tetrahedral quadratic elongation is 1.0057 Å, and the tetrahedral angle variance is 22.3761°. The average Be—O bond distance has shortened with respect to the lower pressure phase, and the BeO<sub>4</sub> tetrahedra contain two pairs of distinct Be—O bonds, with lengths of 1.604(7) and 1.620(6) Å. This results in an averaged bond length of approximately 1.612(6) Å, which is shorter than both the corresponding ambient and 1.74(5) GPa values, although the change in the internal tetrahedral angles indicates distortion in the shape of the BeO<sub>4</sub> tetrahedra. The Be-O-Be bond angles have also decreased to 119.4(2)°. The rotation and collapse of the voids within the tetrahedral framework can be seen in Figure 3.5. With the change of symmetry, there is now only one distinct hydroxyl group environment, as seen in Figure 3.6. The O···H bond length becomes 2.11(6) Å, and the O—H bond length has decreased, with respect to  $\beta$ -behoite, to 0.86(5) Å. The hydrogen bonding donor-host-acceptor triad for this phase has become 152(8)°.

In comparison, for the tetragonal phase of Zn(OH)<sub>2</sub> at 1.4 GPa, the average Zn—O bond in Zn(OH)<sub>2</sub> decreases from 1.954(4) Å to 1.91(3) Å, with two distinct pairs of Zn—O bonds of 1.932 and 1.886 Å in each tetrahedron [152]. This is approximately a 3% decrease in bond length upon compression, whereas the average Be—O bond length in Be(OH)<sub>2</sub> at 5.3(1) GPa is less than 2% shorter than its ambient length. In this regard, the ZnO<sub>4</sub> tetrahedra are slightly more compressible than the BeO<sub>4</sub> tetrahedra. Hydrogen bonding positions and distortion for the high-pressure tetrahedral phase of Zn(OH)<sub>2</sub> were not documented, but they are expected to behave in a similar fashion as in Be(OH)<sub>2</sub>.

The high pressure  $\gamma$ -polymorph persisted up to at least 30.1(1) GPa, the highest pressure reliably reached in our experiments, although the data collected at this pressure was not

sufficiently complete to perform a full structural refinement. Unlike  $\text{Zn}(\text{OH})_2$ , no significant changes in the morphology of the crystals were observed, and only a very small volume discontinuity ( $\Delta V=1\%$ ) accompanied the transition.

### 3.3.2 Symmetry Relations Between $\beta$ - and $\gamma$ -Phases

The reciprocal spaces of the  $\beta$  and  $\gamma$  polymorphs are related according to the equation:

$$\mathbf{A}[\text{hkl}]_{\beta} = [\text{hkl}]_{\gamma}^T$$

$$\mathbf{A} = \begin{bmatrix} 1 & -1 & 0 \\ 1 & 1 & 0 \\ 0 & 0 & 1 \end{bmatrix}$$

where  $[\text{hkl}]_{\beta}$  and  $[\text{hkl}]_{\gamma}$  represent reciprocal vectors of the two respective phases. The two polymorphs can also be considered in terms of space group symmetry relationships. According to the Landau theory, when the crystal structure of a material is altered during a displacive phase transition, the resulting structure is related by symmetry to the original phase by a direct subgroup-supergroup relation [153]. In case of the phase transition in behoite, there exists only an indirect supergroup-subgroup relationship between ambient  $\beta$ -behoite and its high-pressure polymorph. A similar indirect symmetry relation was found for  $\alpha$ -cristobalite and cristobalite-II, and was interpreted in terms of Rigid Unit Mode mechanism characteristic of framework silicates [154].  $\beta$ -behoite has the space group  $P2_12_12_1$ , with the point group symmetry  $222$ , whereas the high-pressure polymorph has the space group  $Fdd2$  with point group symmetry  $mm2$ . A similar behavior is seen in other hydrogen-bonded crystals; these same two space groups were also found for the ferroelectric and antiferroelectric phases of  $\text{KD}_2\text{PO}_4$  (KDP). However, in KDP these polymorphs do not directly transform to each other, but rather are separated by a paraelectric phase. The path through a symmetry tree leading from  $P2_12_12_1$  to  $Fdd2$  is shown in Figure 3.3, and involves four intermediate steps. The first of these steps leads to the tetragonal space group of  $\alpha$ -cristobalite,  $P4_12_12$ . These two space groups are in a direct *translationengleiche*-type I relation, meaning that the translation vectors and size of the primitive unit cells are unaltered across this change. According to the interpretation of Kusaba et al. [152] the first high pressure phase of  $\text{Zn}(\text{OH})_2$  also assumes the tetragonal  $P4_12_12$  space group, and as such it is also a direct *translationengleiche*-type I relation. The second stage is a symmetry

reduction to  $C222_1$  symmetry, known from  $\text{AlPO}_4$ -berlinite [155], which is the only step involving changes in the unit cell vectors. The next three steps involve face-centered symmetries,  $F222$ ,  $Fddd$  and finally,  $Fdd2$ . The change from base-centered to face-centered space group is the only *klassengleiche*-type IIa transition within the whole path – the crystal class is unaltered, but symmetry operators change. The  $Fdd2$  space group in a cristobalite-type tetrahedral framework has been seen in  $\text{Na}_2\text{BeSi}_2\text{O}_6$ -chkalovite, in which both Si and Be cations occupy the tetrahedral sites [156]. According to our observations, neither of the intermediate symmetries manifest themselves as distinct intermediate phases in  $\text{Be}(\text{OH})_2$ . The orthorhombic unit cell of the high-pressure  $\gamma$  phase, when transformed to the setting equivalent to the low pressure phase using transformation matrix (2), is monoclinic in *c*-unique setting, with equal *a* and *b* parameters. The interior  $\varphi$  angle between the  $[100]$  and  $[010]$  direct space vectors is approximately 95 degrees, and decreases with increasing pressure.

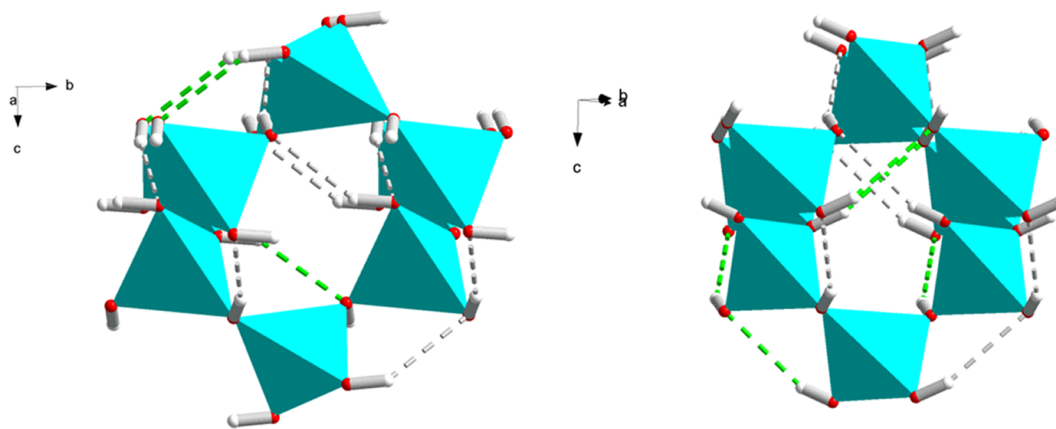


*Figure 3.5. Hydrogen bonding environments in low- and high-pressure  $\text{Be}(\text{OH})_2$ . Two unique hydrogen bonding environments, with different bonding patterns, exist in the low-pressure phase. The green and gray hydrogen bonds displayed differentiate these unique bonding regimes.*

### 3.3.3 Equation of State

Miletich [135] determined the PV equation of state for the high pressure  $\gamma$ -polymorph with a 3<sup>rd</sup> order BM-EOS he obtained  $K_0=45.6$  GPa,  $K'=3.4$  and  $V_0=289 \text{ \AA}^3$ , whereas a 2<sup>nd</sup> order fit (where  $K'$  is fixed to 4) gave  $K_0=43.7$  GPa and approximately the same  $V_0$  (uncertainties were not reported). In the same study, the phase transition point was determined to be between 1.30 and 3.92 GPa based upon x-ray diffraction and Raman spectroscopy measurements. Our high-pressure data, without transforming the high-pressure unit cell to the low-pressure setting, produce  $K_0=48(7)$  GPa,  $K'=5.2(6)$  and  $V_0=282(3) \text{ \AA}^3$ , or  $K_0=49(3)$  GPa and  $V_0=287(2) \text{ \AA}^3$  when  $K'$  is constrained to 4. The normalized stress-Eulerian strain ( $F_N-f_E$ ) analysis shown in Figure 3.7 indicates that the 3<sup>rd</sup> order Birch-Murnaghan fit is preferred. The results of third-order EOS fit are shown in Figure 3.8. For the low pressure phase, the four available data points were insufficient to constrain an equation of state fit. The atypical behavior of the unit cell within this lower-pressure region is attributed to the rearrangement and bifurcation of hydrogen bonds before the phase transition. The equation of state data for  $\gamma$ -Be(OH)<sub>2</sub> are consistent with the established behavior of  $\alpha$ -cristobalite, with the higher bulk modulus justified by the much smaller ambient unit cell volume. For high-pressure cristobalite-II, the bulk modulus (with  $K'$  constrained to 4) is approximately  $K_0=40$  GPa, compared to 20 GPa for the ambient  $\alpha$ -cristobalite [75, 135]. There is currently no comparable equation of state for the tetrahedrally coordinated form of zinc hydroxide, although Kusaba and Kikegawa [134] described the high-pressure, octahedrally coordinated, CdI<sub>2</sub>-like phase of Zn(OH)<sub>2</sub> at 400°C with a third order BM-EOS with  $K_0 = 46.7$  GPa and  $K' = 8.6$ .

The linear compressibilities (defined as  $\beta_{10}=1/3K_{10}$ ) [149] for  $\gamma$ -behoite were determined using a linearized version of the 2<sup>rd</sup> order Birch-Murnaghan equation with unit cell parameters in the setting of the low pressure phase. The resulting refined linear moduli were  $K_{a0}= 60(3)$  GPa, and  $K_{c0}= 65(3)$  GPa. The corresponding axial compressibility ratios of  $\gamma$ -behoite  $\beta_{a0}:\beta_{b0}:\beta_{c0}$  are 1.00:1.00:0.92. The results of linear EOS fit can be seen in Figure 3.9. During this transition the  $c$  axis lengthens, whereas  $a$  and  $b$  discontinuously shrink.

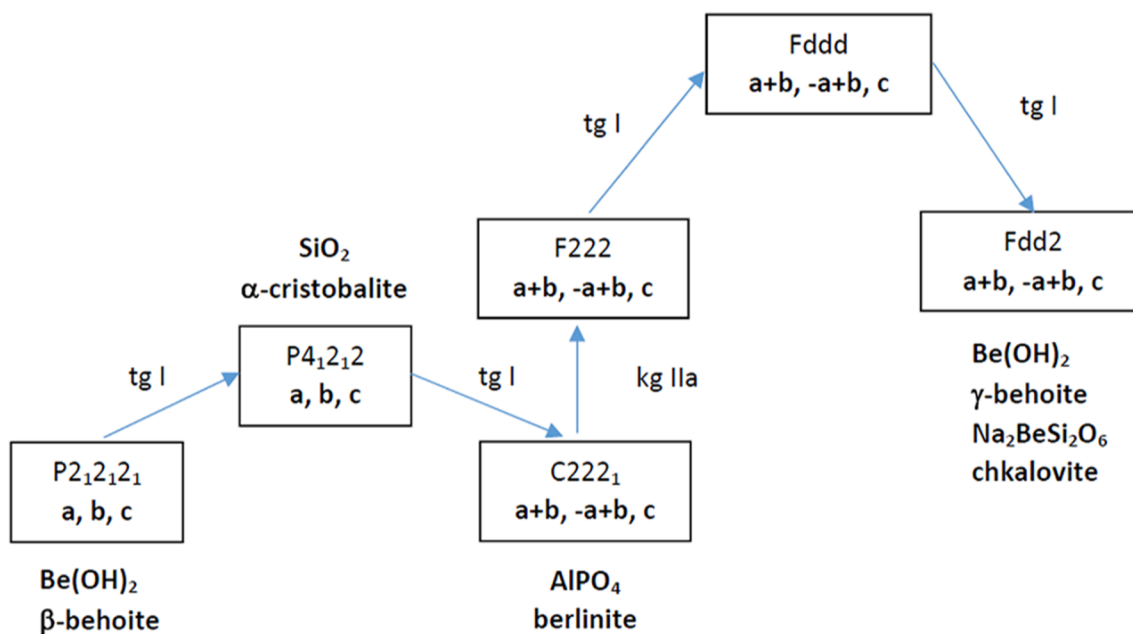


Figure 3.6. Diagram of subgroup-supergroup relations between the low and high-pressure phases of  $\text{Be}(\text{OH})_2$ . The letters under the space group symbol show unit cell vectors, with  $a$ ,  $b$ , and  $c$  representing the  $\text{P}2_12_12_1$  setting. tg and kg represent translationengleiche and klassengleiche relations. Vertical positions of each pair of space group connected by arrow depict super (above) and subgroup (below) hierarchy.

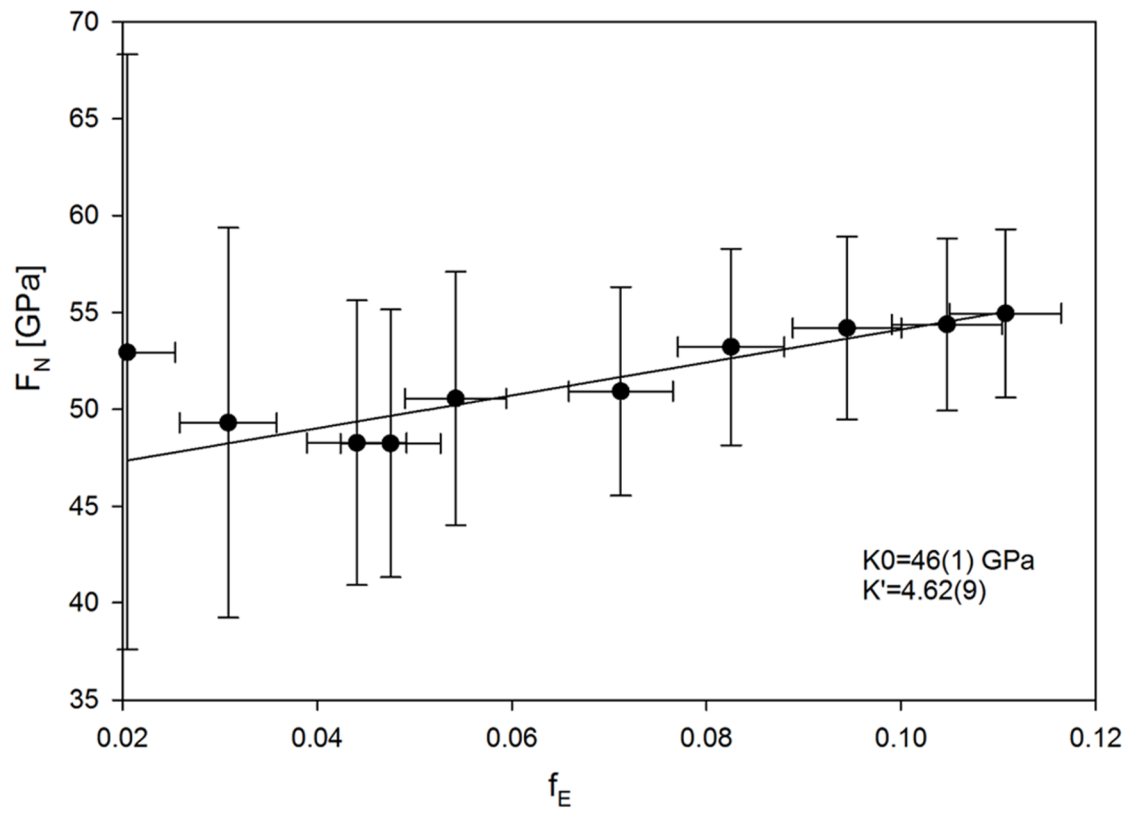


Figure 3.7.  $F_f$  plot of  $\text{Be}(\text{OH})_2$ , where normalized stress is plotted against Eulerian strain, for the high-pressure phase. Data points coincide well with a third-order BM-EOS fit.

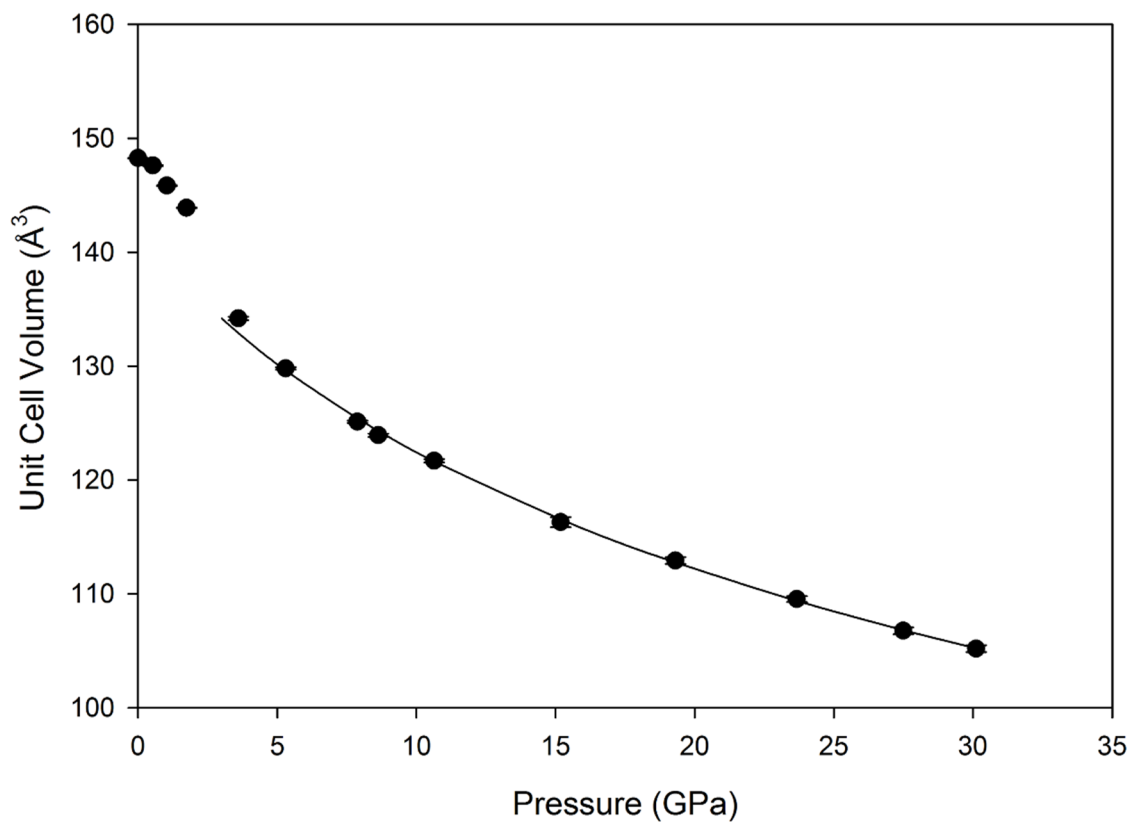


Figure 3.8. Unit cell volume versus pressure for  $\text{Be}(\text{OH})_2$ , fitted with a third-order BM-EOS. The unit cell in this graph has been transformed to the lower-pressure  $P2_12_12_1$  setting:  $V_0$  is half of the untransformed value.

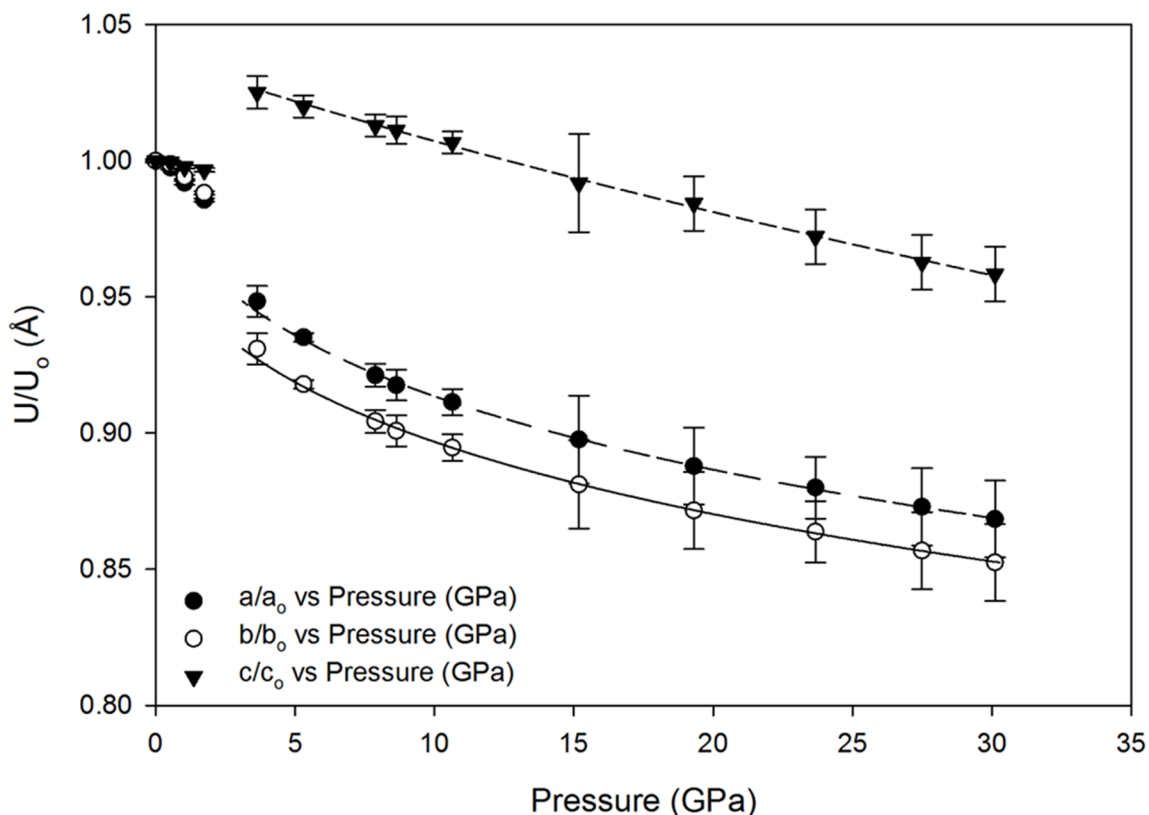


Figure 3.9. Pressure evolution of unit cell parameters of  $\text{Be}(\text{OH})_2$ , transformed to the low pressure unit cell setting, and normalized to ambient unit cell conditions. Results of linearized second-order Birch–Murnaghan EOS fits for each axis are shown with dashed and solid lines.

### 3.4 DISCUSSION

In order to understand the effect of hydrogen bonds on the transformation mechanism in behoite, all of the similarities and differences in the reference series ( $\alpha$ -cristobalite- $\text{SiO}_2$ , behoite- $\text{Be}(\text{OH})_2$ , and wülfingite- $\text{Zn}(\text{OH})_2$ ) must be considered in order to use these compounds as anhydrous and hydrous isostructural equivalents of one another.

Among the various polymorphs of  $\text{SiO}_2$ , cristobalite is one of the high temperature phases into which silica melt crystallizes on cooling. The structure of cristobalite is composed of corner-connected  $\text{SiO}_4$  tetrahedra that form a 3-dimensional modified diamond framework. This

framework possesses voids that gradually collapse through tetrahedral rotation, when the crystal is compressed at high pressure [75, 151, 157]. At pressures of about 1.5 to 1.8 GPa and ambient temperature,  $\alpha$ -cristobalite undergoes a displacive phase transition to monoclinic  $P2_1/c$  cristobalite-II [75, 151, 157]. The  $\alpha$ -II transformation has been shown to be suppressible with sufficiently rapid pressure increase [75]. This transformation is also reversible on pressure release, with a very small density change between the phases of  $\Delta V/V_0 \leq 0.1\%$  [75, 157].

Zinc hydroxide has been previously studied at high pressures and temperatures [134, 152, 158]. At ambient conditions,  $\text{Zn}(\text{OH})_2$  has orthorhombic unit cell parameters with  $a = 8.471(2)$  Å,  $b = 5.140(2)$  Å,  $c = 4.903(2)$  Å, and a unit cell volume of  $213.5(1)$  Å<sup>3</sup> with an average Zn-O bond length of  $1.954(4)$  Å and an average Zn-O-Zn bond angle of  $120.8(2)$  degrees [137]. At these conditions, like  $\text{Be}(\text{OH})_2$ , the structure of  $\text{Zn}(\text{OH})_2$  follows the  $P2_12_12_1$  space group [137]. The Zn-O bond distance within  $\text{Zn}(\text{OH})_2$  is much longer than the corresponding average Si-O and Be-O distances in  $\alpha$ -cristobalite and  $\text{Be}(\text{OH})_2$ , which are only  $1.611(1)$  Å and  $1.632(4)$  Å, respectively [137, 151]. The disparity in cation-oxygen bond lengths causes a significant difference in the polyhedral volumes;  $\text{ZnO}_4$  tetrahedra in wülfingite are approximately 78% and 72% larger than the  $\text{SiO}_4$  and  $\text{BeO}_4$  tetrahedra in cristobalite and  $\text{Be}(\text{OH})_2$ , respectively. Despite the larger tetrahedra in  $\text{Zn}(\text{OH})_2$ , the polyhedral packing efficiencies for  $\text{Zn}(\text{OH})_2$  and  $\text{Be}(\text{OH})_2$  are similar ( $0.071(1)$  and  $0.060(1)$ , respectively), where the polyhedral packing efficiency is defined as the ratio of the summed volumes of all the tetrahedra within a unit cell to the unit cell volume. For comparison, the polyhedral packing efficiency in  $\alpha$ -cristobalite, where no hydrogen bonds hold the polyhedra close together, is  $0.049(1)$  [151].

At approximately 1.1 GPa,  $\text{Zn}(\text{OH})_2$  readily adopts a high pressure phase that is stable until 2.1 GPa, and is accompanied by a 10% increase in density [134, 158]. This phase change is reversible, but appears to be a first-order transition: upon decompression there is a hysteresis of about 0.4 GPa, with the high pressure phase reverting to the ambient phase at 0.7 GPa. The high-pressure phase has been suggested to display either the  $P4_12_12$  or  $P4_32_12$  space group, where each group is an enantiomer of the other [152, 158]. The phase change is akin to cristobalite, where the transition is accompanied by rotations of rigid tetrahedra within the crystal structure. It is unknown, at this time, if the hydrogen bonds present within  $\text{Zn}(\text{OH})_2$  change simultaneously with the rotation of the tetrahedra, or if some degree of bond distortion exists. If  $\text{Zn}(\text{OH})_2$

behaves in a fashion similar to other metal hydroxides, such as  $\text{Ca}(\text{OH})_2$ , it is likely that simultaneous reconfiguration of the hydrogen atoms with the tetrahedral rotations plays a large role in the rate of transition [152, 159].

Above 2.1 GPa, another gradual phase change was also observed in  $\text{Zn}(\text{OH})_2$  [152], where the structure and behavior of this second high-pressure phase has not yet been determined. Increase in temperature and in pressure past 2.1 GPa elicit more changes in the structure of  $\text{Zn}(\text{OH})_2$ : two high temperature-pressure phases were observed by Kusaba et. al., one with an unsolved orthorhombic structure, and the other with a  $\text{Mg}(\text{OH})_2$ -like structure [134].

The  $P2_12_12_1$  space group of  $\beta$ -behoite is related to  $\alpha$ -cristobalite's  $P4_22_12$  space group by a direct, type-I *translationengleiche* subgroup-supergroup relation, where the same translation vectors are found in both structures [160], as shown in the symmetry tree diagram in Figure 3.3. The  $\text{Be}(\text{OH})_4$  polyhedra have geometries very similar to the  $\text{SiO}_4$  units in cristobalite. The presence of the hydrogen bonds, however, deforms the voids in the structure and changes the average T-O-T angle to approximately 126 degrees, which accounts for a unit cell volume smaller than  $\alpha$ -cristobalite by 14% [137, 151].

Similarly to  $\alpha$ -cristobalite,  $\beta$ - $\text{Be}(\text{OH})_2$  undergoes a phase transition between 1.7 and 3.6 GPa. This transformation is accompanied by a negligible volume change, in contrast with the 10% volume discontinuity seen in  $\text{Zn}(\text{OH})_2$ . As with  $\alpha$ -cristobalite and  $\text{Zn}(\text{OH})_2$ , this transition is reversible [135]. Previous high-pressure experiments on  $\text{Be}(\text{OH})_2$  were conducted using synthetic  $\beta$ - $\text{Be}(\text{OH})_2$  powders. Miletich studied behoite's compression behavior up to 10.9 GPa in a 4:1 methanol-ethanol pressure medium and observed a phase transition between 1.79 and 3.11 GPa, but did not report the structure of the high-pressure phase [135].

The  $\beta$ - $\gamma$  transformation of  $\text{Be}(\text{OH})_2$  is both displacive and reversible, with the mechanism involving primarily rotation of rigid  $\text{Be}(\text{OH})_4$  tetrahedra. At ambient conditions, the  $\text{Be}(\text{OH})_4$  tetrahedra are not lined up with respect to one another, forming a pattern of alternating orientations in the plane perpendicular to the  $c$ -axis. When the crystal is compressed, the rigid structural units are forced closer together, causing a realignment and rotation of the tetrahedra, which reduces the inter-polyhedral space, and changes the orientation of the tetrahedra with respect to each other. This is consistent with the mechanism for the pressure induced response found in the wülfingite and related tectosilicates, where rotation of the  $\text{SiO}_4$  tetrahedra

accompanies a slight decrease in the Si-O-Si bond angle, with minimal distortion of the tetrahedra [151, 157]. The pressure-evolution of the unit cell parameters for both  $\beta$  and  $\gamma$ -Be(OH)<sub>2</sub>, normalized to ambient unit cell parameters, is shown in Figure 3.9.

Downs and Palmer suggest that the compressibility of  $\alpha$ -cristobalite is significantly correlated to the bending of Si-O-Si angles and the shortening of Si-Si distances [151]. In  $\alpha$ -cristobalite, as pressure is exerted on the lattice, the SiO<sub>4</sub> tetrahedra rotate and the chain collapses. The same structural response in behoite is hindered by the connecting hydrogen bonds. The average Be-O-Be angle in behoite changes from 126.4(6)° at 0.53(5) GPa to 126.2(6)° at 1.74 GPa, and 119.4(2)° at 5.3(1) GPa. In cristobalite the Si-O-Si angle decreases by 6° over a 1.05 GPa range [151] whereas the Be-O-Be angle in behoite decreases by approximately 7° over a larger range of 3.56 GPa. The Be-O-Be angles observed in behoite are less compressible than the Si-O-Si angles due to the bridging hydroxyl groups in behoite, which add both bulk in terms of atomic repulsion character and rigidity from hydrogen bonding.

Although the above interpretation simply describes the hydrogen bonding behavior of Be(OH)<sub>2</sub>, it does not account for other differences in bonding behavior between behoite and wülfingite. The greater Zn-O bond distance causes the Zn(OH)<sub>4</sub> polyhedra to be much larger than Be(OH)<sub>4</sub> units, despite overall similar hydrogen bond geometry, causing greater framework distortion, as the hydrogen bonds bridge between bulkier tetrahedra. The ambient value of the Zn-O-Zn angle (about 121°) is smaller in comparison to the Be-O-Be inter-tetrahedral angle (about 126°). The bulkier nature of the Zn(OH)<sub>2</sub> structure allows it to become frustrated and energetically unfavorable at much lower pressures than Be(OH)<sub>2</sub> or SiO<sub>2</sub>. This follows a general trend where applied pressure causes an increase of structural distortion within tetrahedra, with structures that have larger cations being comparatively unstable at lower applied pressures [130, 161]. For these large-cation tetrahedra, phase transformations to denser forms were observed at lower pressures than with small-cation homeotypes. The large cation compounds are also in general more compressible. Simultaneous increases of pressure and temperature among  $\alpha$ -quartz homeotypes add an additional effect, where transitions to denser, octahedrally coordinated phases are observed under 10 GPa for all but the smallest cations, and are predicted to be stable past 80 GPa [130].

The trends seen with  $\alpha$ -quartz analogues likely explain what has been seen in the hydrated  $\alpha$ -cristobalite analogues, given the difference in size between the central beryllium and zinc cations. Additionally, at elevated temperatures, the same transition to sixfold coordinated cation polymorph is seen in zinc hydroxide as in non-hydrated  $\alpha$ -quartz analogues.  $\gamma$ -behoite's stability up to 30 GPa also mirrors what is seen in small cation  $\alpha$ -quartz analogues. It is unclear at this time what role hydrogen bonding plays in fostering or inhibiting the phase transitions from fourfold to sixfold coordinated polyhedra. Haines et. al. describes phase transformations from four-coordinated to six-coordinated polyhedra in anhydrous  $\alpha$ -quartz homeotypes that may involve metastable or amorphous intermediates [130]. This seems to be the case with zinc hydroxide, although the hydrogen bonds may prolong the stability of this intermediate phase, observed between 1.1 to 2.1 GPa. Further exploration of  $\text{Zn}(\text{OH})_2$ 's phase transition behavior is needed to better describe its hydrogen bonding and phase behavior, particularly the large volume discontinuity accompanying its first phase transition. The stability range of behoite's high pressure polymorph also needs to be further explored, including the high temperature regime, up to the point of dehydration.

### 3.5 CONCLUSIONS

The pressure-induced phase transition behavior of behoite mirrors that of  $\alpha$ -cristobalite in several ways: both have reversible phase transitions at similar pressure conditions, where the rotation of the structural tetrahedra and angle reduction between tetrahedral elements is directly responsible for the changes in symmetry and unit cell dimensions. The key difference is the hydrogen bonding in behoite, which accounts for additional structural rigidity and resistance against tetrahedral rotation. Significant rearrangements and strain on the hydrogen bonds are apparent on compression within the  $\beta$ -phase stability range, leading to hydrogen bond bifurcation. The  $\beta$ - $\gamma$  phase transition relaxes the strained hydrogen bonds through discontinuous rotation of one of the protons towards a new acceptor. Upon compression to higher pressures, it is anticipated that this  $\text{H1} \cdots \text{O2}$  bond will eventually break and re-coordinate, potentially allowing further structural changes if the hydrogen bond influence is lessened. It remains to be seen if this alteration of the hydrogen bonding occurs at a point similar to the cristobalite II-XI transition, or if the hydrogen bonds cause behoite to deviate away from cristobalite's general compressional behavior and follow the path of the  $\text{Mg}(\text{OH})_2$ -like structures, as seen with the

high pressure, high temperature behavior of zinc hydroxide. Additional comparison with zinc hydroxide, including bond angles and bond lengths, would better establish the predictability of hydrogen bonding behavior in cristobalite-like metal hydroxides.

Similarities in the general trends of high-pressure behavior of anhydrous silica and its fully hydroxylated isotypes are quite apparent in the analogous compression mechanisms, dominated by the rigid unit rotation. On the other hand, the effects of a fully populated network of hydrogen bonds in the hydroxides on guiding the polyhedral framework deformation are rather profound, and lead to high-pressure polymorphs preserving the tetrahedral framework connection topology, but accommodating distinctly different symmetries, compared to anhydrous silica. From this perspective, using the knowledge about the behavior of fully-hydroxylated compounds to model the effects of minute amount of hydroxyl defects in nominally anhydrous analogue phases, relevant to deep Earth environments may not be particularly feasible (in nominal anhydrous phases the sparse hydrogen bonds will not be the dominating interaction). On the other hand, there are known and important cases of anhydrous-plus-fully-hydroxylated-analogue systems where both the anhydrous and the hydroxide components may have geologic relevance. A good example of this relation is the stishovite-SiO<sub>2</sub>,  $\delta$ -AlOOH, phase-H-MgSiO<sub>2</sub>(OH)<sub>2</sub> system [162, 163]. All three compounds crystallize in lower-pressure-rutile, higher-pressure-CaCl<sub>2</sub>-type topologies, sharing the common structural motifs [28]. Each of these minerals exhibit the required structural stability to potentially be present in the Earth lower mantle [163, 164], though the rationale for their occurrence depends on the hydration level as a function of depth. Understanding the consequences of the presence or absence of hydrogen bonds on physical properties and phase equilibria in these analogue phases may prove useful in geophysical modeling of the lower mantle, and from this perspective, the comparative analysis of the cristobalite-Be(OH)<sub>2</sub>-Zn(OH)<sub>2</sub> system helps to understand the general relations between such dry-and-wet analogues.

### 3.6 ACKNOWLEDGMENTS

All of the experiments described in this paper were conducted by M. Barkley, and were part of her Ph.D. thesis research, and the main conclusion of this work were described therein. H. Shelton conducted all structure refinements and comparative analysis. All authors contributed to writing the manuscript. The authors gratefully acknowledge the support of this study from the

Chevron Corporation, BP p. l. c., the University of Arizona Galileo Circle, the Tucson Gem and Mineral Society, and Carnegie-DOE Alliance Center under cooperative agreement DE FC52-08NA28554. Development of the GSE\_ADA software used for data analysis is supported by NSF grant EAR1440005. We also thank Prof. M. Rieder and two anonymous reviewers for their keen editing and constructive criticism of this work. Portions of this project were performed at GeoSoilEnviroCARS (Sector 13), Advanced Photon Source (APS), Argonne National Laboratory. GeoSoilEnviroCARS is supported by the National Science Foundation - Earth Sciences (EAR-0622171) and Department of Energy - Geosciences (DE-FG02-94ER14466). Use of the Advanced Photon Source was supported by the U. S. Department of Energy, Office of Science, Office of Basic Energy Sciences, under Contract No. DE-AC02-06CH11357.

## CHAPTER 4. THE IDEAL CRYSTAL STRUCTURE OF CRISTOBALITE X-I: A BRIDGE IN SiO<sub>2</sub> DENSIFICATION

Hannah Shelton<sup>1,2\*</sup>, Tiange Bi<sup>3</sup>, Eva Zurek<sup>3\*</sup>, Jesse Smith<sup>4</sup>, and Przemyslaw Dera<sup>1,2\*</sup>

<sup>1</sup>Department of Geology and Geophysics, School of Ocean and Earth Science and Technology, University of Hawaii at Mānoa, 1680 East West Road, POST Bldg, Honolulu, HI 96822, USA

<sup>2</sup>Hawaii Institute of Geophysics and Planetology, School of Ocean and Earth Science and Technology, University of Hawaii at Mānoa, 1680 East West Road, POST Bldg, Honolulu, HI 96822, USA

<sup>3</sup>Department of Chemistry, 331 Natural Sciences Complex, SUNY Buffalo, Buffalo, NY 14260-3000, USA

<sup>4</sup>High Pressure Collaborative Access Team, Geophysical Laboratory, Carnegie Institution of Washington, Argonne, IL 60439, USA

Contact email: [sheltonh@hawaii.edu](mailto:sheltonh@hawaii.edu), [ezurek@buffalo.edu](mailto:ezurek@buffalo.edu), [pdera@hawaii.edu](mailto:pdera@hawaii.edu)

Published as *J. Phys. Chem. C* **2018**, 122 (30), 17437–17446; doi:10.1021/acs.jpcc.8b04282

### ABSTRACT

On compression of  $\alpha$ -cristobalite SiO<sub>2</sub> to pressures above approximately 12 GPa a new polymorph known as cristobalite X-I forms. The existence of cristobalite X-I has been known for several decades, however, consensus regarding its exact atomic arrangement has not yet been reached. The X-I phase constitutes an important step in the silica densification process, separating low-density tetrahedral framework phases from high-density octahedral polymorphs. It is the only non-quenchable high-density SiO<sub>2</sub> phase, which reverts to the low-density form on decompression at ambient temperature. Recently, an experimental study proposed an octahedral model of SiO<sub>2</sub> X-I with intrinsic structural defects involving partial Si site occupancies. In contrast, our new single crystal synchrotron x-ray diffraction experiments have shown that the ideal structure of this phase should instead be described by a defect-free model, which does not require partial occupancies. The structure of cristobalite X-I consists of octahedral chains with a 4-60°-2 zigzag chain geometry. This geometry has not been previously considered, but is closely related to post-quartz, stishovite and seifertite. In addition to the ideal, defect-free crystal structure, we also present a description of the defects that are most likely to form within the X-I

phase. Density Functional Theory calculations support our observations, confirming the dynamic stability of the X-I geometry and reasonably reproducing the pressure of the phase transformation. The enthalpy of cristobalite X-I is higher than stishovite and seifertite, but X-I is favored as a high-pressure successor of cristobalite due to a unique transformation pathway. Elastic and lattice dynamical properties of the X-I phase show intermediate values between stable tetrahedral and octahedral polymorphs, confirming the bridge-role of this phase in SiO<sub>2</sub> densification.

## 4.1 INTRODUCTION

SiO<sub>2</sub> is one of the most common, yet important, compounds found on Earth. Despite its compositional simplicity, and because of its crystal chemical characteristics, SiO<sub>2</sub> exhibits a complex phase diagram featuring a variety of thermodynamically stable crystalline phases, as well as numerous metastable crystalline polymorphs and glasses. This includes phase transition sequences and resulting polymorphs that are strongly path-dependent. Because of its 3s<sup>2</sup>3p<sup>2</sup> electronic configuration and crystal radius of 0.54 Å, in the solid state silicon strongly prefers four-coordinated tetrahedral crystallographic sites. This low coordination number results in pronounced structural flexibility, with a tendency to form extended silicate chains, sheets, and framework polyhedral motifs, and accounts for a majority of the mineral diversity observed in shallow-depth terrestrial rocks and commonly utilized SiO<sub>2</sub>-derived materials. In response to pressurization, silicon can assume five- and six- coordinated states; carbon, although similar in chemistry, achieves these hypervalent states only rarely [165]. Densification of silicates involving a change of the coordination number of the Si<sup>4+</sup> cation is one of the sources of stratification of the Earth's mantle, and is responsible for the major seismic discontinuities that are observed as a function of depth [28, 166]. The pressure-dependent behavior of SiO<sub>2</sub> also plays a role in mechanochemical reactions with industrial applications, such as zeolite-facilitated polymerization of organic molecules [167, 168]. The interactions of SiO<sub>2</sub> polymorphs with other fundamental systems, CO<sub>2</sub> in particular, create complex host-guest structures and solid solutions with properties relevant to both planetary and materials science [169-171].

Compression mechanisms of tetrahedral silicate frameworks typically proceed via rigid unit modes [172], which enable structural distortions resulting in small symmetry changes, but do not allow for easy coordination changes of the central Si<sup>4+</sup> cations. More significant polymorphic

transformations involved in silica densification have long been thought to occur through first order reconstructive phase transitions, which typically require thermal activation, and do not easily proceed at ambient temperature. A number of intermediate metastable silica phases have been reported, but their crystal structures have not been reliably determined, despite decades of research. Computational efforts employing density functional theory (DFT) and molecular dynamics identified a number of candidate structure models; however, extensive metastability results in a Gibbs free energy hyper-surface pitted with abundant local minima, and selecting the structures that are actually realized in nature has proven challenging [173-175]. Knowledge about the structural and chemical properties of these more elusive polymorphs may provide a better understanding of the factors controlling silica densification.

One of the little-understood phases is cristobalite X-I, which forms on compression of  $\alpha$ -cristobalite at ambient temperature above about 12.9 GPa [63, 75, 176-178]. Cristobalite, found typically in nature as the  $\alpha$ -polymorph, is a high-temperature, four-coordinated form of SiO<sub>2</sub> with well-documented occurrences in a variety of different geologic environments, including terrestrial igneous rocks, protoplanetary disks around young stars [77], and meteorites that were shocked beyond 10 GPa [179], and can even be formed from amorphous silica via biogenic process on bacterial surfaces [180].  $\alpha$ -cristobalite exhibits a range of interesting and somewhat exotic properties; for instance, it is one of a few materials exhibiting auxetic elasticity. Auxetic materials have a negative Poisson's ratio, and when stretched will expand along the axis perpendicular to the direction of the applied tension [181-183]. On compression in hydrogen [7] and helium [142] cristobalite was found to incorporate these species into structural voids.  $\alpha$ -cristobalite was also the starting material for the first successful high-pressure synthesis of quenchable octahedral seifertite-SiO<sub>2</sub> [174] found in heavily shocked meteorites such as Shergotty and Zagami [184, 185], where it is considered a possible proxy of the peak pressure during shock metamorphism.

Here, we report the results of single-crystal synchrotron x-ray diffraction experiments with  $\alpha$ -cristobalite, using a diamond anvil cell, in which a well-diffracting specimen of the X-I phase was formed via a single-crystal to single-crystal transformation at ambient temperature. The crystal structure of this phase was shown to be nearly defect-free, with ideal SiO<sub>2</sub> stoichiometry, and different than the structure model reported recently by [76]. Our experimental results are

compared with those of previously proposed structures [76], and are supplemented with density functional theory calculations that compare the enthalpy of various silica polymorphs on compression, and examine the dynamic stability of the X-I structure.

## 4.2 EXPERIMENTAL AND COMPUTATIONAL METHODS

### 4.2.1 Single Crystal X-ray Diffraction

The  $\alpha$ -cristobalite samples used in our experiments were from the same source as those used in [76], from the Ellora Caves locality in Aurangabad, Maharashtra, India (Harvard Mineralogical Museum 97849), and were kindly provided to us from the RRUFF project collection at the University of Arizona (RRUFF #R061064). High pressure single-crystal x-ray diffraction experiments were conducted at the Advanced Photon Source (APS) at Argonne National Laboratory. Data were collected at the 16-IDB beamline of the High Pressure Collaborative Access Team (HPCAT), with gas-loading of diamond anvil cells at GSECARS [186]. Two single crystal specimens of  $\alpha$ -cristobalite, approximately  $0.030 \times 0.030 \times 0.010$  mm, were loaded into a BX-90 type diamond anvil cell [114] equipped with conical Boehler-Almax type anvils and backing plates [113]. After gas loading with neon as the pressure transmitting medium [186], the sample was compressed to 12.5(1) GPa in one step. X-ray data collected at this point confirmed successful conversion of both sample crystals to the monoclinic SiO<sub>2</sub> X-I phase, as shown in Figure 4.1a. One of the specimens showed poor diffraction quality, but the second crystal produced sufficiently sharp diffraction peaks to permit single crystal analysis. Complete sets of diffraction data were collected on decompression in intervals of about 2 GPa. In order to control pressure changes without removing the cell from the instrument, a gas-driven membrane device with a Druck PACE 5000 electronic valve controller was used to change pressure. Pressure was measured during decompression by the ruby fluorescence method [101] both before and after a set of complete diffraction data was collected. Diffraction data were collected with Kickpatrick-Baez mirror-focused monochromatic x-rays ( $\lambda=0.41073$  Å) focused onto the sample crystals. At each pressure point, the sample was rotated during x-ray exposure around the  $\omega$ -axis of the instrument, with diffraction images collected at three detector positions, differing by detector translation, perpendicular to the x-ray beam by 70 cm. At 2.49(5) GPa we observed the appearance of sharp diffraction peaks of  $\alpha$ -cristobalite. On further decompression these features became broad and the sample partially amorphized. On complete decompression,

the diffraction pattern of the quenched sample was dominated by broader peaks, which could be explained by the decompression-driven partial amorphization, as shown in Figure 4.1b.

Data collected at 10.7(1) GPa were used for structure solution and refinement. Diffraction images were analyzed using the ATREX IDL software package [146]. Peak intensities were corrected for Lorentz and polarization effects. Peaks were indexed using cell\_now [142], and the orientation matrix was refined and unit cell parameters were obtained using RSV [146]. Integrated peak intensities were used for the structure solution. We used two different approaches: direct methods as implemented in Sir92 [187] and simulated annealing as implemented in Endeavour [147]. Both methods yielded the same structure model, which is described in space group  $P2_1/n$ . This model, which will be referred to as X-IH, was used as a starting point for structure refinement with ShelXL [142]. Refinement was conducted with isotropic atomic displacement parameters and full site occupancies for all atoms, and resulted in a final figure of merit  $R1(F2)=8.43\%$ . Values for the zero-pressure unit cell volume ( $V_0$ ), bulk moduli ( $K$  and  $K'$ ), and linear compressibilities were determined with EOSFit7-GUI [188]. fitting experimental unit cell values with second-order Birch-Murnaghan equations of state [149].

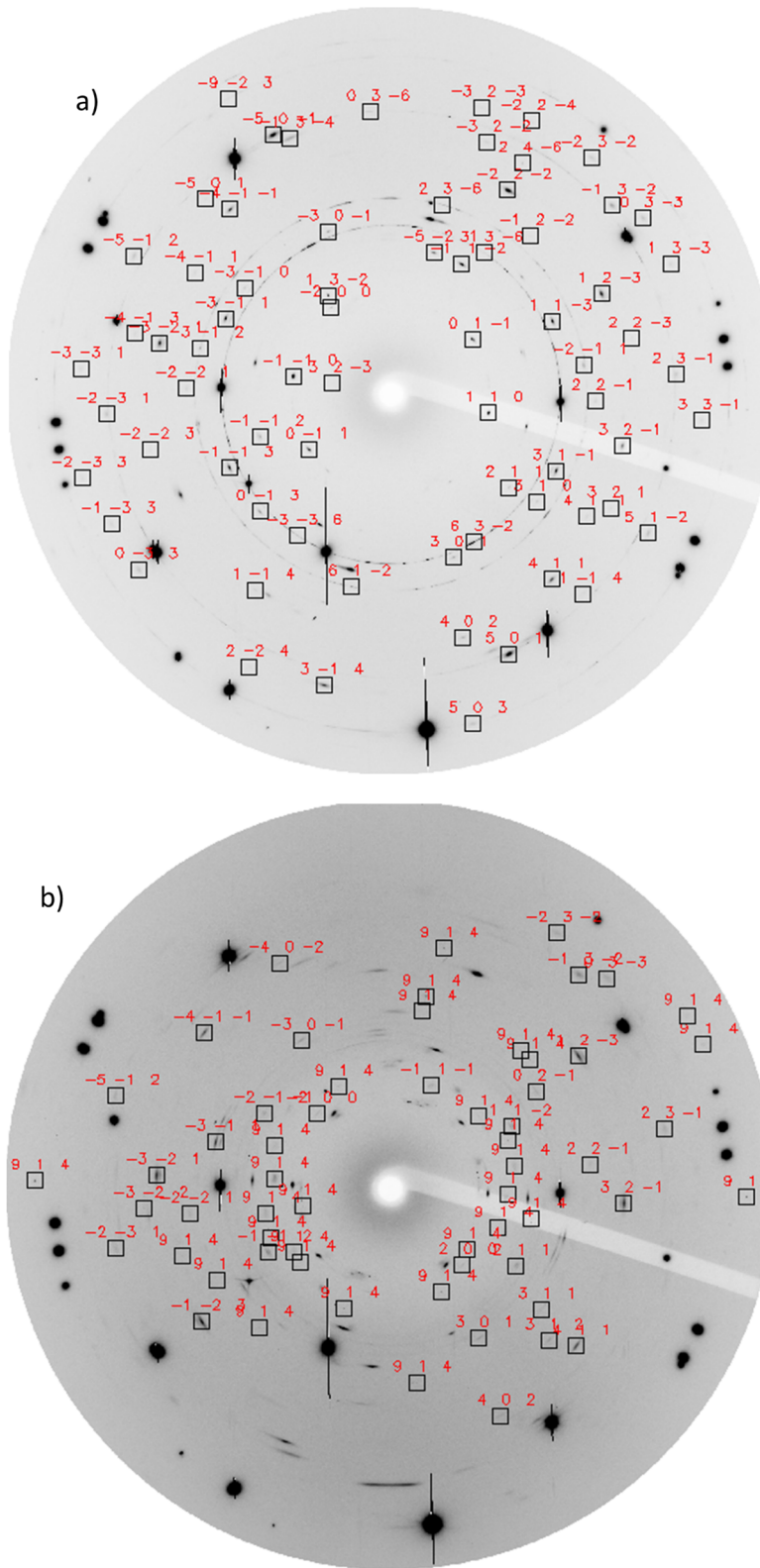


Figure 4.1. Indexed diffraction patterns of cristobalite X-I at 12.5 GPa (a), and quenched sample containing  $\alpha$ -cristobalite (b). Diffraction peaks of two different gains are present, but only one set is shown with Miller index labels.

## 4.2.2 DFT Calculations

Geometry optimizations and electronic structure calculations were performed using DFT, as implemented in the Vienna *Ab Initio* Simulation Package (VASP) version 5.4.1. [189]. In order to account for the effect of long range intermolecular London dispersion interactions, the vdW-DF-optB88 [119, 120, 190] exchange-correlation functional was used, as van der Waals interactions are likely to be important for this system at the pressures considered herein. The projector augmented wave (PAW) method [122] was used to treat the core states with a plane wave basis set. The Si  $3s^2/3p^2$  and O  $2s^2/2p^4$  electrons were treated explicitly using the PAW-PBE Si and PAW-PBE O POTCARs, with the cutoff radii of 1.900 a.u. and 1.200 a.u., respectively. The energy cutoff was set to be 700 eV, while the  $k$ -point grids were generated using the  $\Gamma$ -centered Monkhorst-Pack scheme, and the number of divisions along each reciprocal lattice vector was chosen such that the product of this number with the real lattice constant was 50 Å. Temperature effects were not included in the DFT calculations.

To calculate the elastic stiffness of all studied structures at 10 GPa, the stress-strain method was adopted and six finite distortions of the lattice were performed for each structure. The contributions from the distortions of the rigid ions and the ionic relaxations are included in the reported elastic moduli. Elastic properties, including the Voigt, Reuss, and Voigt-Reuss-Hill averages of bulk modulus ( $K_V$ ,  $K_R$  and  $K_{VRH}$ ), shear modulus ( $G_V$ ,  $G_R$ , and  $G_{VRH}$ ), and the universal elastic anisotropy index ( $A^U$ ) have been calculated utilizing the elastic moduli [191, 192].

We performed phonon calculations for the SiO<sub>2</sub> X-IH structure at 2.5 and 10 GPa and for the cristobalite, cristobalite II, post-quartz, seifertite, stishovite and X-IB phases at 10 GPa using VASP combined with the PHONOPY [123] package under the harmonic approximation. The number of atoms in the simulation supercell was 96 for cristobalite and seifertite, 144 for post-quartz, and 192 for cristobalite II, stishovite and the two cristobalite X-I structures. These correspond to  $2 \times 2 \times 2$  representations of the standard primitive cells for all structures except for stishovite, wherein a  $4 \times 4 \times 2$  supercell was employed. Full calculated phonon dispersion curves for cristobalite X-I at 2.5 and 10 GPa are shown in Figure 4.2. The heat capacity and Debye temperature were obtained from the phonon calculations for all of the structures at 10 GPa.

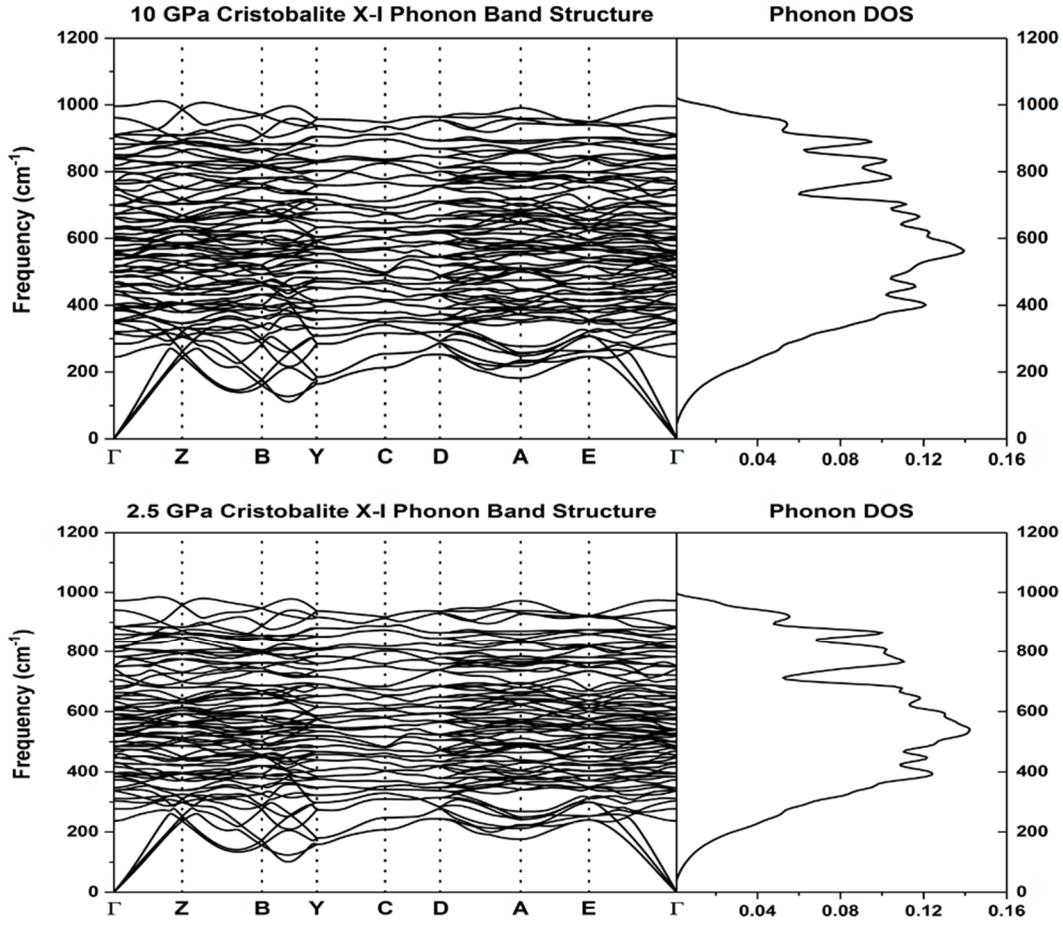


Figure 4.2. Phonon band structure and density of states for cristobalite X-I at 10 and 2.5 GPa. Results are obtained from vdW-DF-optB88 calculations.

The constant volume heat capacity was calculated via

$$C_V = \sum_{qv} k_B \left( \frac{\hbar\omega(qv)}{k_B T} \right)^2 \frac{\exp\left(\frac{\hbar\omega(qv)}{k_B T}\right)}{\left[ \exp\left(\frac{\hbar\omega(qv)}{k_B T}\right) - 1 \right]^2}$$

where  $\hbar$  is the reduced Planck constant,  $k_B$  is the Boltzmann constant,  $T$  is the absolute temperature,  $q$  is the wave vector,  $v$  is the index of the phonon mode, and  $\omega$  is the phonon frequency. The Debye temperature ( $\Theta_D$ ) was calculated from the Debye frequency ( $\omega_D$ ) using the following equation:

$$\Theta_D = \frac{2\pi\hbar\omega_D}{k_B}$$

The Debye frequencies were obtained from the PHONOPY package by fitting the vibrational density of states at lower frequencies (0 to  $\frac{1}{4}$  of the maximum frequency) to a Debye model

$$D(\omega) = a\omega^2$$

The parameter  $a$  and the number of atoms in the unit cell were used to obtain the Debye frequency:

$$\omega_D = \sqrt[3]{\frac{9N}{a}}$$

### 4.3 RESULTS

On compression, cristobalite follows either the  $\alpha \rightarrow \text{II} \rightarrow \text{X-I}$  transition sequence with transition pressures of approximately 1.8 and 12.9 GPa [75], or, depending on compression rate and stress anisotropy, can retain the  $\alpha$ -phase structure to at least 15 GPa, with suppression of the fully tetrahedral phase-II with monoclinic  $P2_1/c$  symmetry [75, 100]. In our decompression experiment the X-I phase formed below 12.5(1) GPa and persisted to at least 2.49(5) GPa, indicating significant hysteresis. The analysis of data collected at 2.49(5) GPa (the experimental pressure closest to the boundary of the  $\alpha$ -II transformation) revealed that domains within the  $\text{SiO}_2$  X-I crystal had experienced a solid-solid phase transformation directly to  $\alpha$ -cristobalite. While the remaining peaks of  $\text{SiO}_2$  X-I retained their significant breadth, the newly formed  $\alpha$ -phase produced sharp diffraction features, suggesting the nucleation of small (probably  $\sim 1 \mu\text{m}$ ), defect-free crystals. These findings are generally consistent with the observations previously reported [76, 100], where quenched samples were analyzed using TEM and were found to be a heterogeneous matrix consisting of amorphous domains with sub-micrometer crystals of  $\alpha$ -cristobalite embedded in them.

These observations are consistent with an X-I to  $\alpha$ -phase transition observed as the sample was decompressed: unlike other dense octahedral  $\text{SiO}_2$  polymorphs, the X-I phase is not quenchable on decompression to ambient temperature. On initial compression, the  $\alpha \rightarrow \text{II}$  transformation seems to be an important step enabling efficient formation of the X-I phase. In

our earlier study [75], rapid compression suppressed the formation of phase II, which greatly extended the metastability range of  $\alpha$ -cristobalite. Without phase II as an intermediate, formation of X-I silica may not be feasible, as Gratz et al. [193] reported shock-induced amorphization. Kubo et al. [194] recently showed that stress rate and transformation kinetics have significant effects on controlling the silica transformation paths, particularly during shock events, and may be responsible for the formation of seifertite, rather than stishovite, within stishovite's stability field. In our decompression experiment cristobalite-II was not observed in any of the data sets, suggesting a preference for the direct back transformation to the original  $\alpha$ -polymorph. The absence of a phase-II intermediate provides a possible explanation for the partial amorphization of the sample on decompression.

By starting from single-crystal specimens of  $\alpha$ -cristobalite, and by assuring quasi-hydrostatic conditions, we were able to obtain a single crystal of SiO<sub>2</sub> X-I suitable for structure analysis. We solved the structure using both direct methods [187] and simulated annealing [147, 195], which both independently arrived at the same model. Our X-I structure model features only two symmetry independent Si sites (both at general 4e Wyckoff positions), which are sufficient to produce the ideal SiO<sub>2</sub> stoichiometry. All Si atoms reside in octahedral sites, which are arranged in an edge-sharing zigzag chain pattern. Various octahedral chain kinking schemes were examined in the family of hypothetical SiO<sub>2</sub> polymorphs by first principles calculations by Teter et al. [196], but the specific arrangement in our X-I model was not considered in that earlier study. For clarity, we adopt a chain-kinking geometry nomenclature, according to which the number of individual octahedra in a straight segment (in the same direction of translation) is specified first, followed by the angle between the first octahedral segment's translational direction and the translation vector to the next straight octahedral section, followed by the number of individual octahedra in the corresponding next segment of octahedra. According to this convention, seifertite represents a 2-120°-2 geometry [184, 185], post-quartz is a 3-120°-2 arrangement [129, 185, 196], whereas X-I contains 4-60°-2 chains. The *m*-phase [197] reported to form from quartz has a chain geometry that is identical with seifertite (2-120°-2), but features monoclinic P2/c symmetry. The P2<sub>1</sub>/n space group in which SiO<sub>2</sub> X-I crystallizes is equivalent, in a different setting, with the P2<sub>1</sub>/c space group of post-quartz [129, 185, 196].

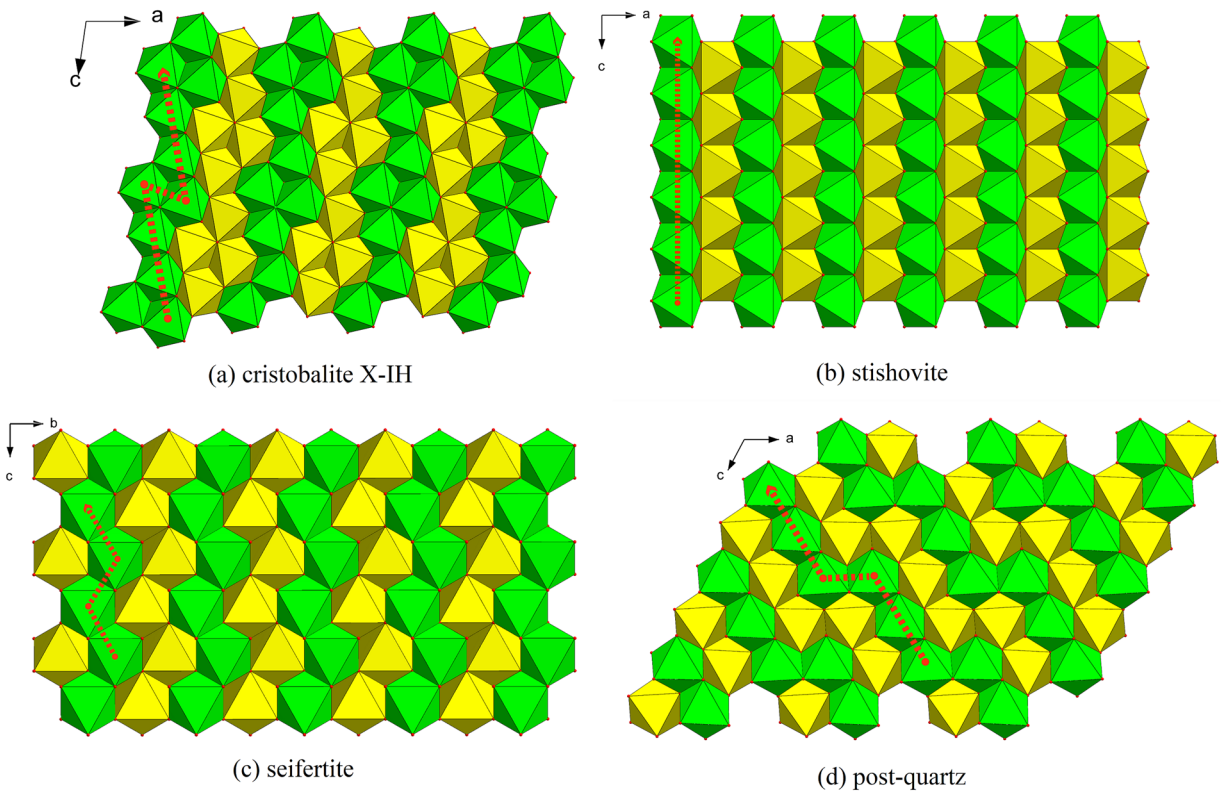


*Figure 4.3: Comparison of octahedral chain geometries in various high density polymorphs of  $\text{SiO}_2$ : a) cristobalite X-IH, b) stishovite [198], c) seifertite [199], d) post-quartz [200]. Green and yellow polyhedra represent alternating layers of octahedral chains aligned with the axis oriented into the page, with voids between chains of like color. The propagation of the chain geometries for each polymorph is highlighted in red.*

Table 4.1. Data collection and refinement details for the SiO<sub>2</sub> X-IH model at 10.7(1) GPa.

<b>P3</b> (10.7(1) GPa)	
No. of reflections collected	227
No. of independent reflections	113
R <sub>int</sub>	0.1118
R[F <sup>2</sup> > 4σ(F <sup>2</sup> )]	0.0843
wR(F <sup>2</sup> )	0.2766
Goodness-of-fit	1.046
No. of parameters refined	26
No. of restraints used	0

Table 4.2. Atomic coordinates and displacement parameters of X-IH at 10.7(1) GPa. The unit cell parameters are a= 6.613(2) Å, b= 4.114(1) Å, c= 6.912(5) Å, β=98.33(6)°.

<b>Atom</b>	<b>x</b>	<b>y</b>	<b>Z</b>	<b>U<sub>eq</sub></b>
Si(1)	0.7056(7)	-0.0054(10)	0.0717(10)	3(2)
Si(2)	0.4264(6)	-0.0031(10)	0.3119(8)	6(2)
O(3)	0.4795(16)	0.2040(30)	0.1050(30)	9(3)
O(4)	0.6410(30)	-0.2520(20)	0.2710(30)	7(3)
O(5)	0.2622(18)	-0.2290(20)	0.1490(20)	2(3)
O(6)	0.3970(20)	-0.2260(30)	0.5210(30)	10(3)

The structure model we propose for cristobalite X-I, which we refer to as X-IH, is shown in Figure 4.3, so it can be compared with other octahedral silica polymorphs. Refinement statistics are listed in Table 4.1, and atomic positions listed in Table 4.2. Bond lengths (Table 4.3) and polyhedral distortions in the X-IH structure are similar to those found in seifertite [199]. Silicon coordination polyhedra share edges that form zigzag chains propagating approximately along the <001> direction. Isolated polyhedral chains are arranged in layers perpendicular to <010>.

Table 4.3. Bond lengths (Å) at 10.7(1) GPa. Bonds marked with # denote symmetry operations as described in Table A2.

Si1-O4 #1	1.723(15)	O3-Si1 #3	1.796(14)
Si1-O6 #2	1.750(18)	O4-Si1 #6	1.723(15)
Si1-O3	1.769(14)	O5-Si2 #7	1.732(14)
Si1-O3 #3	1.796(14)	O5-Si1 #3	1.842(17)
Si1-O4	1.812(19)	O6-Si1 #8	1.750(18)
Si1-O5 #3	1.842(17)	O6-Si2 #5	1.788(15)
Si2-O5	1.718(12)	Si1-Si2	2.656(8)
Si2-O5 #4	1.732(14)	Si1-Si2 #3	2.669(9)
Si2-O6	1.75(2)	Si1-Si1 #3	2.756(9)
Si2-O3	1.743(18)	Si2-Si2 #5	2.641(11)
Si2-O4	1.808(18)	Si2-Si1 #3	2.669(9)
Si2-O6 #5	1.788(15)		

Octahedra in neighboring layers do not overlap. SiO<sub>2</sub> X-I can be easily converted to seifertite by selectively shifting half of the Si<sup>4+</sup> cations from one octahedral layer to empty octahedral voids in the neighboring layer. Similar transformation mechanisms were proposed for stishovite and seifertite [185, 201]. The 4-60°-2 arrangement of octahedral chains is less compact than the 2-120°-2 arrangement of seifertite, and contains large cavities formed by clusters of octahedral voids. Such cavities are absent in seifertite and stishovite.

Recently, a new structure model for the cristobalite X-I phase [76, 100] based on single-crystal diamond anvil cell experiments similar to our own was reported. We will refer to this model as the X-IB model. Both models share important similarities, including the same unit cell parameters and space group, but they are crystallographically distinct. There are several peculiarities about the X-IB model: in order to satisfy the ideal stoichiometry of SiO<sub>2</sub> three symmetry independent Si positions are necessary, one of them with only partial occupancy of approximately 50%. Such a structure would be unusual for a SiO<sub>2</sub> polymorph, as all other known polymorphs can be described by means of ideal non-defective structures (though, of course, defect-containing crystals of these phases can be found). The previous report [76] focuses on the compressional behavior of SiO<sub>2</sub> X-I after the transition, at pressures higher than 12 GPa, and on

characterization of samples quenched to ambient conditions. In this study we determined a defect-free ideal structure (X-IH) and focused on details of the decompression behavior of this high-pressure phase below its initial formation pressure. Detailed comparisons of the X-IH and X-IB models are included below, and comparative crystal structure refinements are discussed in the supporting materials. As a consequence, SiO<sub>2</sub> X-I is less dense, higher in enthalpy, and more compressible than the two other octahedral polymorphs.

The P2<sub>1</sub>/n (#14) space group of cristobalite X-I is well constrained by systematic absences of peaks in the experimental data both in this study as well as in [76], and common to the X-IH and X-IB structure models. This space group is centrosymmetric, with the inversion centers located at [0,0,0], [0.5,0,0], [0,0,0.5] and [0.5, 0, 0.5]. There are two kinds of crystallographic positions: general (4e Wyckoff type), not associated with any symmetry element, and special (2a, 2b, 2c and 2d Wyckoff types), located at the inversion centers. The number in the Wyckoff type symbol refers to the number of symmetry equivalents of the given position in the unit cell.

The X-IH and X-IB structure models are in agreement as to the general geometry of the oxygen sublattice, with all 4 oxygen sites located at the general 4e positions, and fully occupied, resulting in a total of 16 oxygen atoms present in the unit cell (corresponding to Z=8). However, the oxygen sublattice also defines the locations of octahedral voids, and the symmetry of this sublattice and the octahedral voids is distinctly different for the two models. In the X-IB model the position of the oxygen sublattice, with respect to the symmetry elements in the unit cell, is such that there are 5 available symmetry-independent octahedral voids, and is described in Table A7. Two of these voids, V4 and V5, are on special Wyckoff positions 2b and 2d, whereas the remaining three are located on general positions 4e. If all of these voids were occupied, there would be 16 Si atoms in the unit cell, but the SiO<sub>2</sub> stoichiometry only allows half of the octahedral voids to be occupied at one time. Such stoichiometric configurations are indeed allowed by the symmetry, but for an ordered structure (full occupancies) either two of the 4e voids, or one general position and both of the special position voids need to be filled. All different structural arrangements corresponding to such Si ion distributions are summarized in Table A9, and shown in the top row of Figure 4.4. None of these six possible arrangements represents the zigzag chain structure, and all of them are most likely to be high in energy because of clustering of occupied octahedra. The crystal structure model X-IB reported by [76] assumes

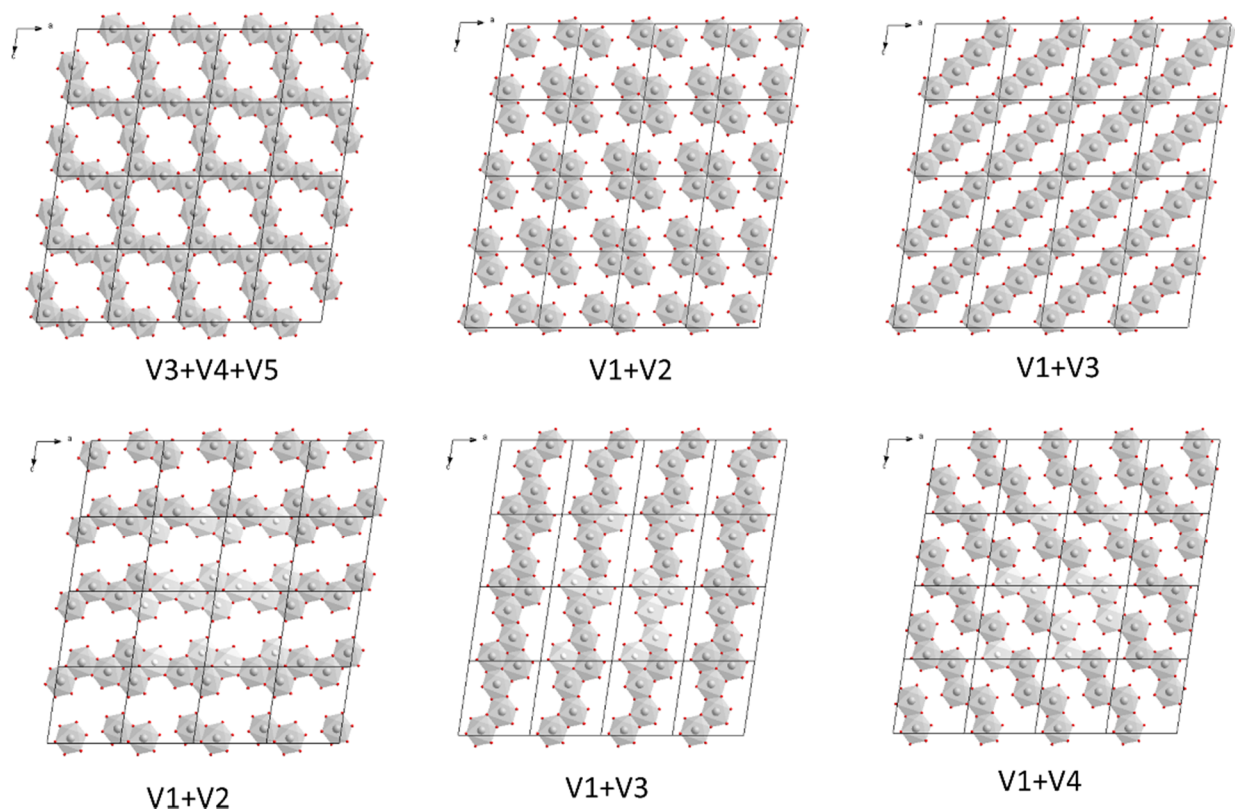


Figure 4.4. Possible  $\text{SiO}_2$  crystal structures with fully occupied Si sites in the oxygen sublattices of models X-IB (top row) and X-IH (bottom row). Labels indicate which of the octahedral voids defined in tables A7 and A8 are occupied.

that only one of the two special position voids is occupied. In order to accommodate the ideal  $\text{SiO}_2$  stoichiometry this implies 1.5 atoms located on general positions, and thus requires partial 50% occupancy of one 4e site, and associated disorder.

The X-IB model with the Si atom locations reported by Černok et al. describes an ideal, fully populated  $3\text{-}120^\circ\text{-}2$  chain propagating along the  $\langle 001 \rangle$  direction (only atoms Si1 and Si2). This  $3\text{-}120^\circ\text{-}2$  chain is shown in grey in Figure 4.5 (S3), and by itself only accounts for a  $\text{Si}_6\text{O}_{16}$  stoichiometry in the unit cell. This partial structural motif is consistent with the X-IH model, as a  $3\text{-}120^\circ\text{-}2$  chain along  $\langle 001 \rangle$  is a sub-component of the ideal  $4\text{-}60^\circ\text{-}2$  chain oriented along  $\langle 001 \rangle$ . An ideal  $4\text{-}60^\circ\text{-}2$  chain structure (which produces the correct  $\text{Si}_8\text{O}_{16}$  stoichiometry), can be formed from the  $3\text{-}120^\circ\text{-}2$  chain structure by adding a fully occupied octahedron at either (but not both) sides of the zigzag kink point (shown in blue in Fig. 4.5). Unfortunately, these two alternative locations are symmetry equivalent in the X-IB model, and thus cannot be occupied with unequal site occupancy factors (SOF). As a consequence, the X-IB model populates these

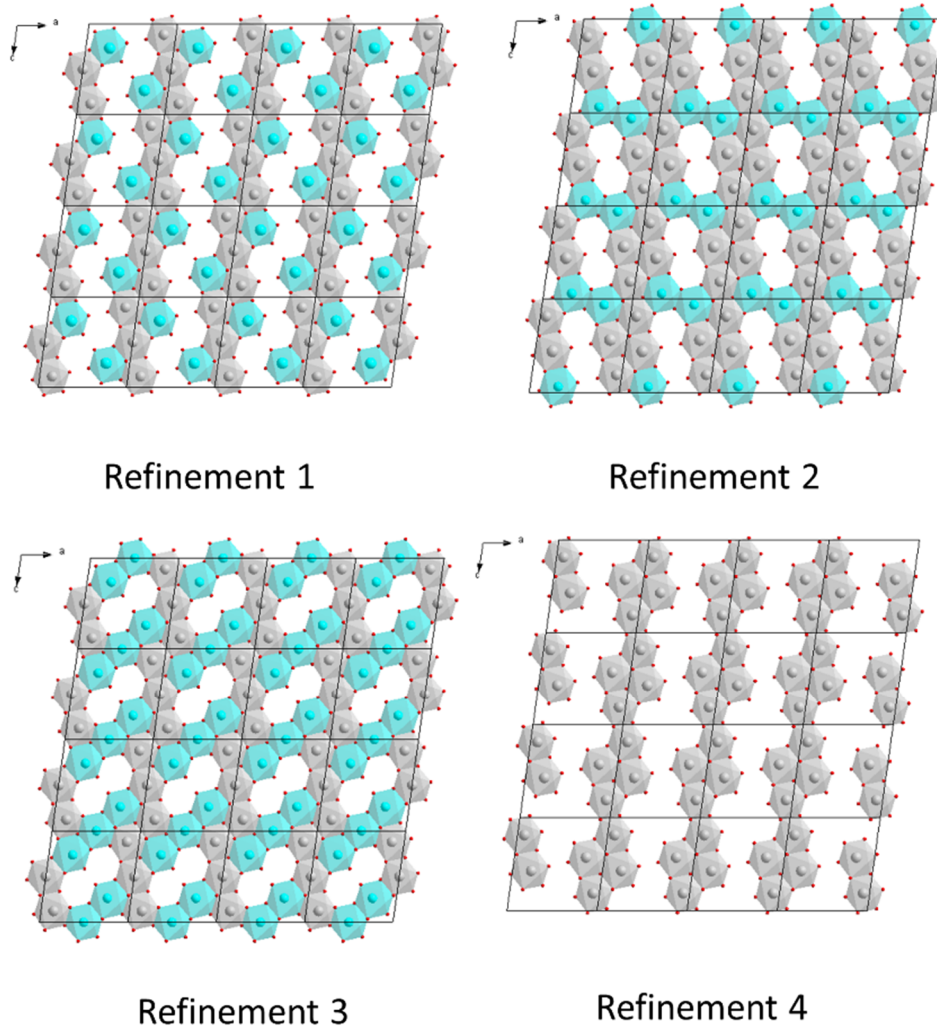


Figure 4.5. Comparative crystal structure refinement results of the X-IH and X-IB models. The refinement results are listed in Table A11.

two sites with even, but partial SOF approximately equal to 0.5. This ion distribution is inconsistent with ideal  $4-60^\circ-2$  chains. Table A9 summarizes all available octahedral void locations in the X-IH model, and Table A10 describes corresponding Si atom distributions. Within this oxygen sublattice model, any two octahedral voids can be fully occupied at one time. In this symmetry, the  $4-60^\circ-2$  chain structure can extend either along  $\langle 001 \rangle$  direction (with voids V1+V3, or V2+V4 occupied) or along the  $\langle 100 \rangle$  direction (with voids V1+V2, or V3+V4 occupied). These topologically equivalent arrangements, shown in the bottom row of Figure 4.4, are almost equal in energy, and likely to lead to disorder and defects. Indeed, both samples obtained in our experiments, and reported by [76] seem to represent such a case, with different

degrees of defects present. Structure refinements conducted with the peak intensity data collected at 40 GPa, from [76] and the X-IH model, indicate that there is a statistical distribution of the 4-60°-2 chains propagating in both directions with probability ratio of approximately 80:20 for  $\langle 100 \rangle$  and  $\langle 001 \rangle$ , respectively, whereas for the data reported in this study this ratio is  $\sim 96:4$ .

Most of the earlier experimental studies involving cristobalite X-I were limited either in terms of the sample quality or by the shortcomings of high-pressure powder diffraction, and thus did not provide definitive answers or solid platforms for computationally generated structure models. In order to obtain a clearer picture of the relative energetics of different polymorphs of SiO<sub>2</sub> and to gain an understanding of the lattice dynamics of the X-I phase we performed a series of DFT calculations. SiO<sub>2</sub> X-I has been one of the most challenging test cases for structure prediction by first-principle methods, even in terms of just predicting the proper coordination geometry. Models of SiO<sub>2</sub> X-I based on powder diffraction experiments and different computational approaches and approximations range from purely tetrahedral [202, 203], through mixed tetrahedral-octahedral [174, 177, 204], to completely octahedral [76, 100]. Some calculations also predict direct transformation from  $\alpha$ -cristobalite to stishovite [205].

To explore this, structure models of  $\alpha$ -cristobalite, cristobalite-II, X-IH, stishovite, seifertite and post-quartz were optimized at unit cell volumes corresponding to pressures from 0 to 50 GPa and their enthalpies, with respect to  $\alpha$ -cristobalite, are shown in Figure 4.6. The X-IH phase has the highest enthalpy of all the octahedral phases considered in this comparison, as it never becomes an equilibrium phase. It does, however become enthalpically favorable over both  $\alpha$ -cristobalite (as do all other octahedral polymorphs), as well as cristobalite-II, at pressures of 5 GPa and 6.6 GPa, respectively. This is consistent with the experimental results, as a difference of at least 5 GPa in DFT-calculated and observed transition pressures is typical. The X-IH phase has the highest enthalpy of all the octahedral phases considered in this comparison, as it never becomes an equilibrium phase. It does, however become enthalpically favorable over both  $\alpha$ -cristobalite (as do all other octahedral polymorphs), as well as cristobalite-II, at pressures of 5 GPa and 6.6 GPa, respectively. This is consistent with the experimental results, as a difference of at least 5 GPa in DFT-calculated and observed transition pressures is typical.

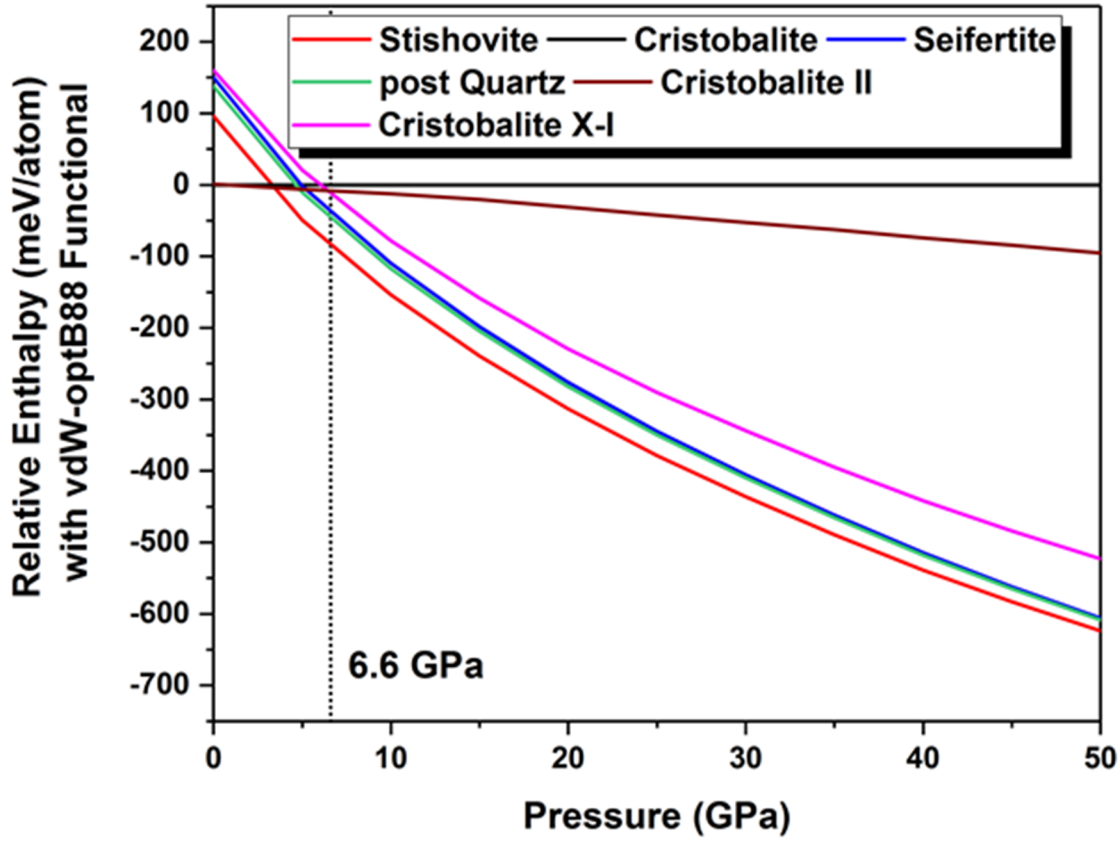


Figure 4.6. Enthalpies as a function of pressure for the cristobalite-II, stishovite, seifertite, post-quartz, and SiO<sub>2</sub> X-I phases, relative to  $\alpha$ -cristobalite between 0 and 50 GPa. The enthalpies were calculated with DFT using the vdW-DF-optB88 functional.

Another recent DFT study [197] found evidence that dynamic phonon instability in quartz is responsible for the transformation to high-density polymorphs at ambient temperature, and the ambient phonon density of states (DoS) for  $\alpha$ -cristobalite was recently investigated using a combination of inelastic x-ray scattering and first principles calculations [206]. Our phonon calculations do not predict any imaginary phonon frequencies, confirming the dynamic stability of the X-IH structure. Additional thermoelastic parameters and behavior of the X-IH structure in comparison to other SiO<sub>2</sub> polymorphs, were also calculated. The heat capacities ( $C_v$ ), the Debye frequencies and temperatures, as well as the elastic tensors and moduli were derived from structures optimized at 10 GPa. A plot of the heat capacities between 0 and 2000 K is shown in Figure 4.7, while other thermoelastic parameters are provided in Tables A3 and A4. As with the enthalpy comparison, the X-IH and X-IB structures are intermediate in heat capacity at all

calculated temperatures between the low and high-density polymorphs, displaying the relationship of  $C_v$  to the connectivity of the  $\text{SiO}_n$  polyhedra and the propagation of phonons within the crystal structure. In general, the same trend is displayed with the Debye frequencies and temperatures for each structure; as the crystal lattice stiffens and compressibility decreases with pressure, the Debye temperature increases. This trend can be seen as pressure increases and the amount of void space between  $\text{SiO}_n$  polyhedra decreases [207, 208].

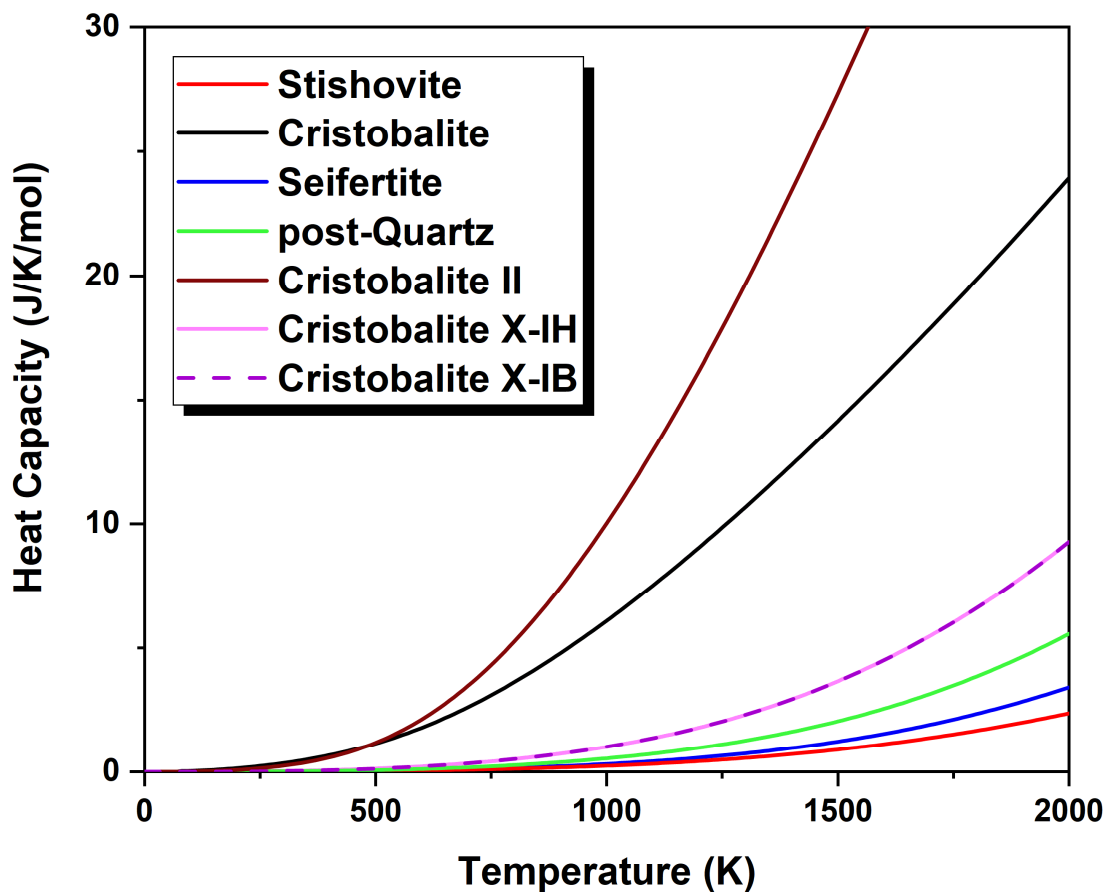


Figure 4.7. Theoretically determined heat capacities ( $C_v$ ) as a function of temperature for cristobalite-II, stishovite, seifertite, post-quartz, and the  $\text{SiO}_2$  X-IH and X-IB phases.

Using unit cell parameters from both our experiment and data provided by the authors of Černok et al. the equation of state of SiO<sub>2</sub> X-IH, truncated to 50 GPa, was determined with a second-order Birch-Murnaghan (BM2) fit. From this fit,  $K_0 = 237(12)$  GPa and  $V_0 = 192.9(4)$  Å<sup>3</sup>, which is in close agreement with the EoS parameters [76, 100] based on earlier experimental data. An additional BM2 fit to our computational DFT unit cell parameters gave  $K_0 = 248.1(1)$  GPa, and  $V_0 = 197.2(8)$  Å<sup>3</sup>, which is consistent with the experimental results. Higher-pressure EoS parameters were obtained from DFT calculations on a 4×4 superstructure representing the disordered X-IB arrangement, which also agree reasonably well with experimental data. As expected, the bulk modulus of the X-IH phase is much higher than  $K' = 8.4(4)$  for  $\alpha$ -cristobalite and  $K_0 = 25(2)$  GPa,  $K' = 4$  for cristobalite-II [75], but also lower than that of stishovite (294(2) GPa) [198] and seifertite (322(4) GPa) [199]. The ambient zero-pressure volume ( $V_0$ ) of the X-IH phase, with large octahedral void clusters, is larger than the more compact stishovite and seifertite. Comparison of the compressibility data for X-I and other octahedral SiO<sub>2</sub> phases, scaled to  $Z=1$ , is presented in Figure 4.8. At the lowest pressure point of our experiment we observed an anomaly of the unit cell parameter behavior, where the unit cell volume seems to slightly decrease on decompression. The diffraction signal changed, indicating the onset of transformation to  $\alpha$ -cristobalite. Within this pressure range, where cristobalite X-I was already out of its range of relative stability over the tetrahedral phases, the quality of the diffraction signal had significantly deteriorated, indicating the beginning of partial amorphization [76, 100]. As a result, the uncertainties of the unit cell parameters increased due to the increased mosaicity in the sample. We also expect that the co-existence of crystalline and amorphous phases may induce additional strain via templating/epitaxial effects, and distort the crystal structure.

Axial compressibilities, defined as  $\beta_{10} = 1/3K_{10}$  [149], were determined from our experimental and DFT results using linearized second-order Birch-Murnaghan equations for each of the unit cell parameters, and are shown in Figure 4.9. The linear axial compressibilities obtained from experimental data, derived from linear moduli, were  $\beta_{a0} = 3.7(1) \times 10^{-4}$  GPa<sup>-1</sup>,  $\beta_{b0} = 8.6(1) \times 10^{-4}$  GPa<sup>-1</sup>, and  $\beta_{c0} = 3.8(1) \times 10^{-4}$  GPa<sup>-1</sup>, indicating that cristobalite X-I is more compressible along the  $\langle 010 \rangle$  direction, perpendicular to the layers of octahedral chains, than along  $\langle 100 \rangle$  and  $\langle 001 \rangle$ , which have comparable linear compressibilities. This elastic anisotropy is understandable given the large, highly compressible octahedral void spaces that are

present between each layer of octahedral chains. This is consistent with the results of DFT calculations, where computed linear axial compressibilities were  $\beta_{a0} = 3.0(1) \times 10^{-4} \text{ GPa}^{-1}$ ,  $\beta_{b0} = 7.6(2) \times 10^{-4} \text{ GPa}^{-1}$ , and  $\beta_{c0} = 3.4(1) \times 10^{-4} \text{ GPa}^{-1}$ . The additional compressibility of the  $b$  axis with respect to the  $a$  and  $c$  axes is also described by the X-IH phase's large universal elastic anisotropy ( $A^u$ ) index of 6.201, where a perfectly isotropic material would have  $A^u$  equal to 0, and the index for quartz is approximately 0.8 [192]. Elastic anisotropy related to octahedral chain geometries have also previously been observed in seifertite, which has a similar structural motif of linked polyhedral chains with void space between chains of the same plane, and a comparable  $A^u$  value of 5.741 [199].

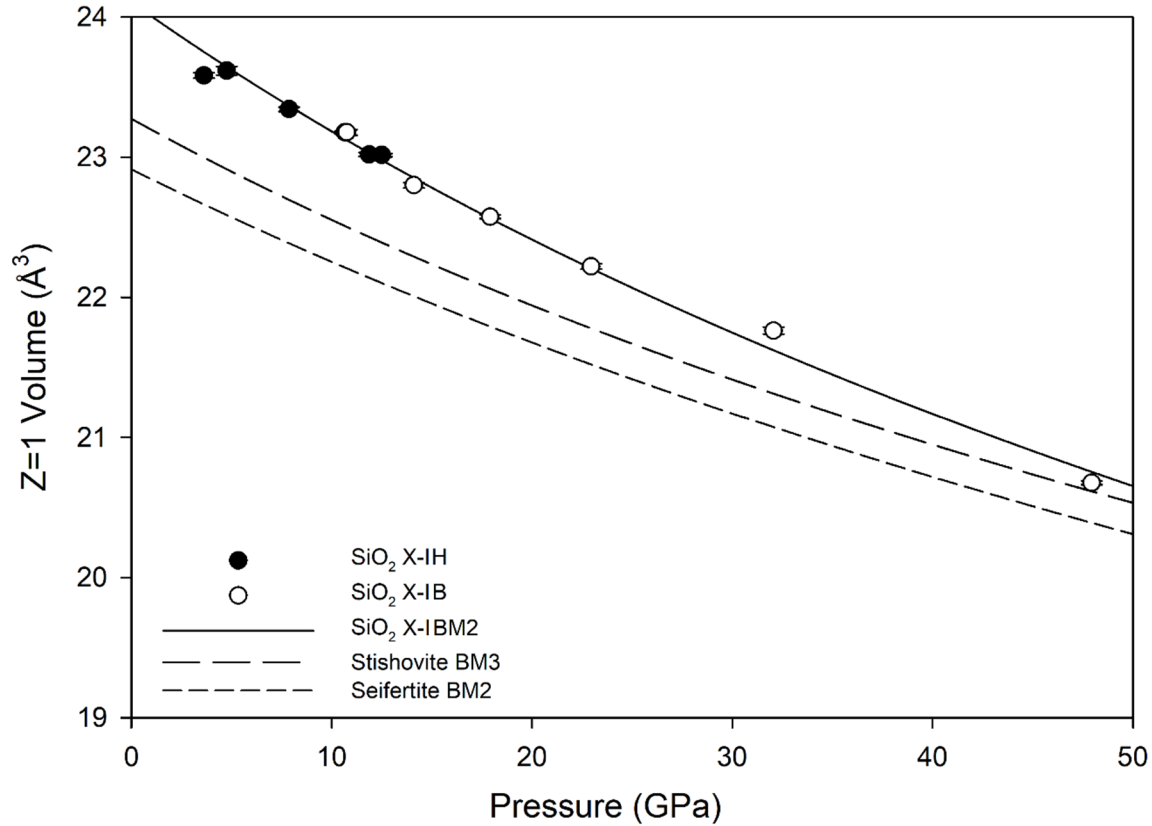


Figure 4.8. Comparison of equations of state for  $\text{SiO}_2$  X-I, stishovite [198] and seifertite [199] up to 70 GPa.  $\text{SiO}_2$  X-I data points are from this study (X-IH, filled circles) and from Černok et al. 2017 (X-IB, open circles).  $\text{SiO}_2$  X-I and seifertite curves are second-order BM fits, while the stishovite curve is third-order.

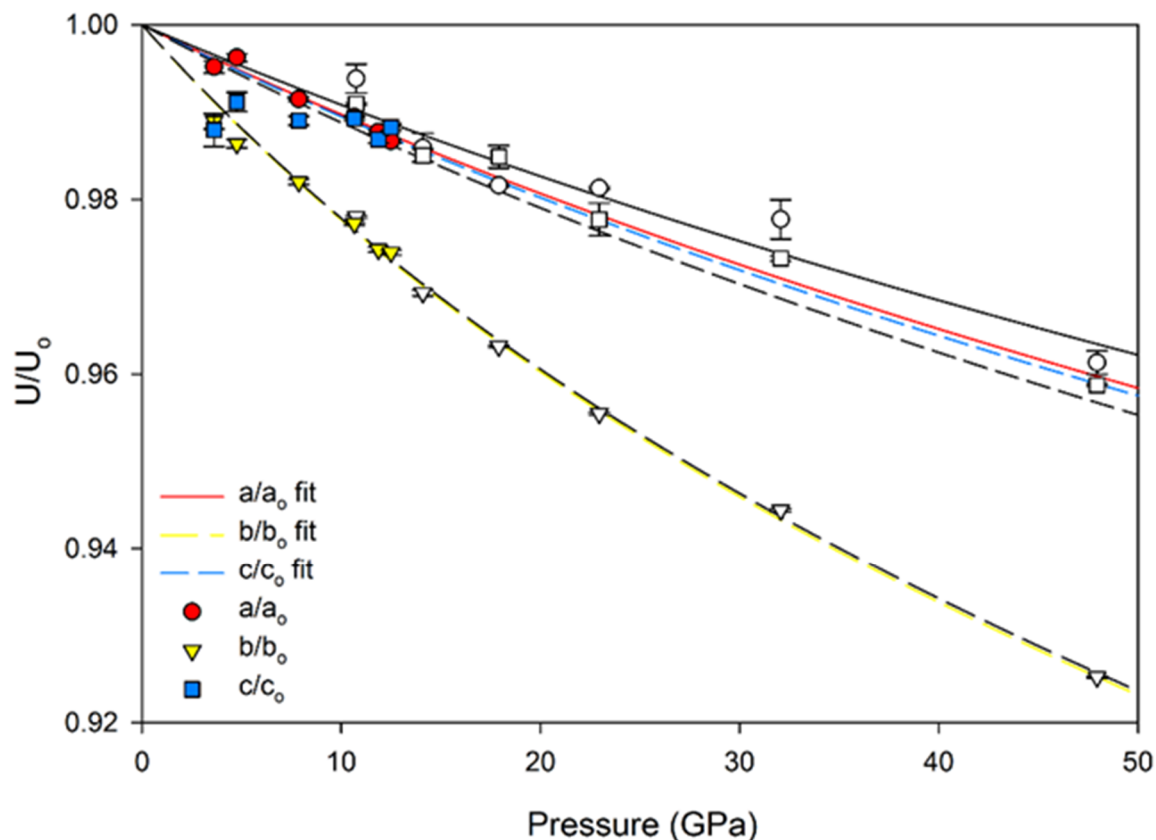


Figure 4.9. Pressure dependence of normalized unit cell parameters. Colored symbols are from experimental data (this study), open symbols are from [76]. Experimental fits (colored lines) are color-matched to experimental data, computational fits (black lines) are pattern-matched to experimental fits.

#### 4.4 DISCUSSION

SiO<sub>2</sub> serves as a fundamental model for understanding phase relations and polymorph topologies for many other chemical systems. For instance, different phases of H<sub>2</sub>O and clathrates have been compared with silica polymorphs, including recent reports of hydrogen clathrate hydrates with similar structural elements as quartz [5, 209]. Some complex organic molecules adopt silica-like crystalline arrangements at high pressure [210]. Cristobalite has unique characteristics in the pressure-temperature space of the SiO<sub>2</sub> phase diagram, with regard to its pressure-dependent behavior. While there are a number of different octahedral high-pressure polymorphs of silica, synthesizing them by compression of tetrahedral phases at ambient temperature is not trivial. Tetrahedral polymorphs other than cristobalite tend to undergo displacive, rigid-unit-preserving distortions when cold-compressed, as seen with coesite [211, 212]. Others form highly defective phases, such as post-quartz [129], or amorphize.  $\alpha$ -

cristobalite has been the only starting material from which SiO<sub>2</sub> X-I can easily be made, and SiO<sub>2</sub> X-I is also the only octahedral SiO<sub>2</sub> phase that cannot be metastably quenched. CaCl<sub>2</sub>-type post-stishovite is also not quenchable, but it only reverts to octahedral stishovite via subtle symmetry distortion [66]. These observations suggest a favorable transformation pathway between low-density  $\alpha$ -cristobalite and octahedral SiO<sub>2</sub> X-I that is characterized by a shallow activation barrier and a deep valley in the Gibbs free energy surface.

CO<sub>2</sub> and carbonate mineral pressure-temperature phase diagrams also share significant analogies with SiO<sub>2</sub>. Carbon has a much smaller ambient ionic radius than silicon (0.15 Å) [64], and is regarded as incompatible with high coordination number geometries. However, a number of tetrahedral high-pressure phases have been reported in both experiments and theoretical calculations. While at low pressure, solid phases of CO<sub>2</sub> contain distinct molecular units, but on high compression, carbon dioxide molecules lose their integrity in favor of assuming silicate-like extended polymeric framework structures with CO<sub>4</sub> tetrahedral units [213]. For example, the high-pressure phase-V of CO<sub>2</sub> has a partially collapsed tetrahedral  $\alpha$ -cristobalite structure [171], and CO<sub>2</sub> can also assume a coesite-type structural arrangement [62]. CO<sub>2</sub> and SiO<sub>2</sub> have even been shown to form a solid solution at pressures of 16-22 GPa and temperatures above 4000 K [170], indicating the potential for carbon to be incorporated into deep earth silicates [214]. This compatibility, however, does not seem to extend to octahedral phases.

Thus far, no high-pressure phase with octahedrally coordinated carbon has been observed. Computational studies have predicted the transformation from four- to six-fold coordination in CO<sub>2</sub> to occur above 950 GPa [60]. One of these predicted structures shares the same space group (*Pbcn*) and structural topology as seifertite. With this link to a high-pressure silica phase, the existence of high-coordination carbon phases in extreme conditions, such as the interiors of giant exo-planets, cannot be ruled out. One experimental study reported the observation of a high-pressure CO<sub>2</sub> phase-VI with octahedral coordination [215], but this interpretation was later disputed in favor of an incompletely transformed molecular arrangement [61, 216]. Diamond has recently been reported to form through the reaction of octahedral (post-stishovite or seifertite) SiO<sub>2</sub> with MgCO<sub>3</sub> carbonate at pressures above 80 GPa and temperatures above 1700 K [217]. Confidently determining the crystal structure and elasticity of cristobalite X-I, a phase that

bridges the tetrahedral and octahedral polymorphs of SiO<sub>2</sub>, enhances our understanding of how carbonates may transform into dense, highly-coordinated phases at extreme conditions.

## 4.5 CONCLUSIONS

Over the last few decades, significant progress has been made in describing the structures of high-pressure SiO<sub>2</sub> phases and the relationships between them, particularly post-quartz and cristobalite X-I. However, questions remain pertaining to several of these structures. Octahedral chain motifs based on distorted, close-packed arrays of oxygen atoms have long been the suspected topology, but the complex energy landscape of SiO<sub>2</sub> and possible crystallographic defect incorporation has made structure solution challenging without reliable high quality experimental constraints. Our results finally settle this debate with a simple model of the X-I phase that does not invoke extensive vacancy defects or partial occupancies, which has been reliably refined against single crystal x-ray diffraction data, and was demonstrated to be dynamically stable, though higher in enthalpy than stishovite, seifertite, or post-quartz, according to DFT calculations.

Broad diffraction features have been observed in every previous experiment in which SiO<sub>2</sub> X-I has been produced, indicating a tendency for this polymorph to accommodate structural defects. Given that the symmetry and unit cell parameters are generally consistent between experiments, it is likely that the variations in individual experimental observations are small departures from an ideal model. Based on the crystallographic refinement conducted with our own data and the experimental diffraction peak intensities obtained by Černok et al. [76] as well as our own DFT calculations, we believe that the model presented in this study properly describes this ideal structure.

The metastable SiO<sub>2</sub> polymorphs of post-quartz and X-I share many characteristics, as they are intermediate structures between thermodynamically stable low-pressure tetrahedral framework structures and high-pressure octahedral phases. Post-quartz and SiO<sub>2</sub> X-I form from different precursors and retain a memory of these parent phases, reverting to the same precursors on decompression. The X-I phase is a bridge between the low-density tetrahedral SiO<sub>2</sub> phases and the high-density polymorphs, and is the only non-quenchable octahedral polymorph that reverts to the original low-density tetrahedral arrangement. Our experimental and computational results converge on a model of SiO<sub>2</sub> X-I that does not invoke extensive vacancy defects or partial

occupancies. Cristobalite-like polymorphs based on 4-coordinated  $\text{CO}_4$  units have been observed in experiments and predicted theoretically; additionally, structural links between octahedrally coordinated  $\text{CO}_2$  and seifertite have been predicted. As a link between different coordination states of  $\text{SiO}_2$ , the X-I phase may be a structure model that describes the formation of octahedrally coordinated carbonates at ultra-high pressure from the currently known cristobalite-like phases.

#### **4.6 ACKNOWLEDGMENTS**

We gratefully acknowledge the willingness of the Bayerisches Geoinstitut group to share with us their crystallographic refinement files for the purpose of cross-comparison of the X-IH and X-IB structure models. We also thank G. Finkelstein for his editing and comments.

We also acknowledge the support of this study from the Carnegie-DOE Alliance Center under cooperative agreement DE FC52-08NA28554. Development of the ATREX software used for data analysis has been supported by NSF grant EAR1440005. This work was performed at HPCAT (Sector 16), Advanced Photon Source (APS), Argonne National Laboratory. HPCAT operations are supported by DOE-NNSA under Award No. DE-NA0001974 and DOE-BES under Award No. DE-FG02-99ER45775, with partial instrumentation funding by NSF. The Advanced Photon Source is a U.S. Department of Energy (DOE) Office of Science User Facility operated for the DOE Office of Science by Argonne National Laboratory under Contract No. DE-AC02-06CH11357. E.Z. acknowledges the NSF (DMR-1505817) for financial support. T. B. was supported by the DOE-NNSA under Award Number DE-NA0002006. The Center for Computational Research (CCR) at SUNY Buffalo is acknowledged for computational support.

## CHAPTER 5: EVOLUTION OF INTERATOMIC AND INTERMOLECULAR INTERACTIONS AND POLYMORPHISM OF MELAMINE AT HIGH PRESSURE

Hannah Shelton,<sup>1,2</sup> Przemyslaw Dera,<sup>1,2\*</sup> and Sergey Tkachev<sup>3</sup>

<sup>1</sup>Department of Geology and Geophysics, School of Ocean and Earth Science and Technology, University of Hawaii at Mānoa, 1680 East West Road, POST Bldg, Honolulu, HI 96822, USA

<sup>2</sup>Hawaii Institute of Geophysics and Planetology, School of Ocean and Earth Science and Technology, University of Hawaii at Mānoa, 1680 East West Road, POST Bldg, Honolulu, HI 96822, USA

<sup>3</sup>Center for Advanced Radiation Sources, University of Chicago, Argonne National Laboratory, 9700 S. Cass Ave., Bldg. 434, Argonne, Illinois 60439, U.S.A.

Published as: *Crystals* **2018**, 8(7), 265; doi:10.3390/cryst8070265

### ABSTRACT

Melamine (C<sub>3</sub>H<sub>6</sub>N<sub>6</sub>; 1,3,5-triazine-2,4,6-triamine) is an aromatic substituted *s*-triazine, with carbon and nitrogen atoms forming the ring body, and amino groups bonded to each carbon. Melamine is widely used to produce laminate products, adhesives, and flame retardants, but is also similar chemically and structurally to many energetic materials, including TATB and RDX. Additionally, melamine may be a precursor in the synthesis of superhard carbon-nitrides, such as β-C<sub>3</sub>N<sub>4</sub>. In the crystalline state melamine forms corrugated sheets of individual molecules, which are stacked on top of one another, and linked by intra- and inter-plane N-H hydrogen bonds. Several previous high-pressure X-ray diffraction and Raman spectroscopy studies have claimed that melamine undergoes two or more phase transformations below 25 GPa. Our results show no indication of previously reported low pressure polymorphism up to approximately 30 GPa. High-pressure crystal structure refinements demonstrate that the individual molecular units of melamine are remarkably rigid, and their geometry changes very little despite volume decrease by almost a factor of two at 30 GPa and major re-arrangements of the intermolecular interactions, as seen through the Hirshfeld surface analysis. A symmetry change from monoclinic to triclinic, indicated by both dramatic changes in diffraction pattern, as well as discontinuities in the vibration mode behavior, was observed above approximately 36 GPa in helium and 30 GPa in neon pressure media. Examination of the hydrogen bonding

behavior in melamine's structure will allow its improved utilization as a chemical feedstock and analogue for related energetic compounds.

## 5.1 INTRODUCTION

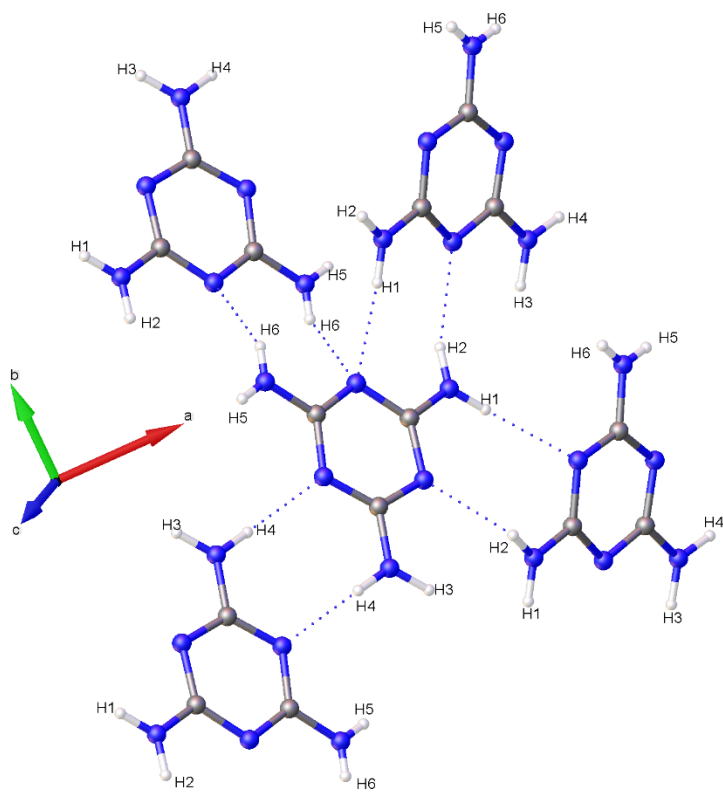
The 6-membered aromatic ring of *s*-triazine, particularly when substituted with nitro (-NO<sub>2</sub>) groups, is a structural motif often found among molecular energetic materials [218]. Melamine, (C<sub>3</sub>N<sub>6</sub>H<sub>6</sub>, 1,3,5-triazine-2,4,6-triamine) is a simple and very stable heterocyclic aromatic molecule based on the *s*-triazine ring. At ambient conditions melamine forms a crystalline molecular solid with monoclinic symmetry, with space group P2<sub>1</sub>/a, in which intermolecular interactions are dominated by N-H···N hydrogen bonds. At ambient conditions individual melamine molecules are linked to others via eight N-H hydrogen bonds, balanced between donor and acceptor roles. The superstructure of melamine forms corrugated sheets of individual melamine molecules, where kinked planes of molecules are stacked on top of one another. When used as a salt or mixed with resins, melamine is an effective fire retardant, in part due to the release of flame-smothering nitrogen gas when burned [219]. When combined with formaldehyde, melamine forms a very durable thermosetting plastic used in a broad variety of kitchenware and household goods [220]. Despite its stability and flame-retardant properties, melamine is also very closely related, both structurally and chemically, to the widely used molecular explosives RDX (hexahydro-1,3,5-trinitro-1,3,5-triazine), TATB (2,4,6-triamino-1,3,5-trinitrobenzene), and to 2,4,6-trinitro-1,3,5-triazine, a hypothetical new explosive [221] which has not yet been successfully synthesized [222, 223]. As a curiously stable cousin of these explosives, melamine is a worthwhile target of investigation in the search for new energetic materials with enhanced safety and stability while maintaining sufficient explosive potential [224].

The primary motivation for studying the high-pressure behavior of melamine ultimately stems from its intermediate position between energetic species and ultra-hard materials; for instance, melamine may be a functional precursor for synthesis of a hypothetical  $\beta$ -C<sub>3</sub>N<sub>4</sub> phase, with a  $\beta$ -Si<sub>3</sub>N<sub>4</sub> structure, predicted to be a super-hard material [225]. Melamine appears to be a good reagent for the high-pressure, high-temperature solid state reactions where carbon nitrides are formed; however, the transformations it exhibits are rather complex, and the products strongly depend on the conditions of pyrolysis and presence of catalysts. Montigaud et al. [226]

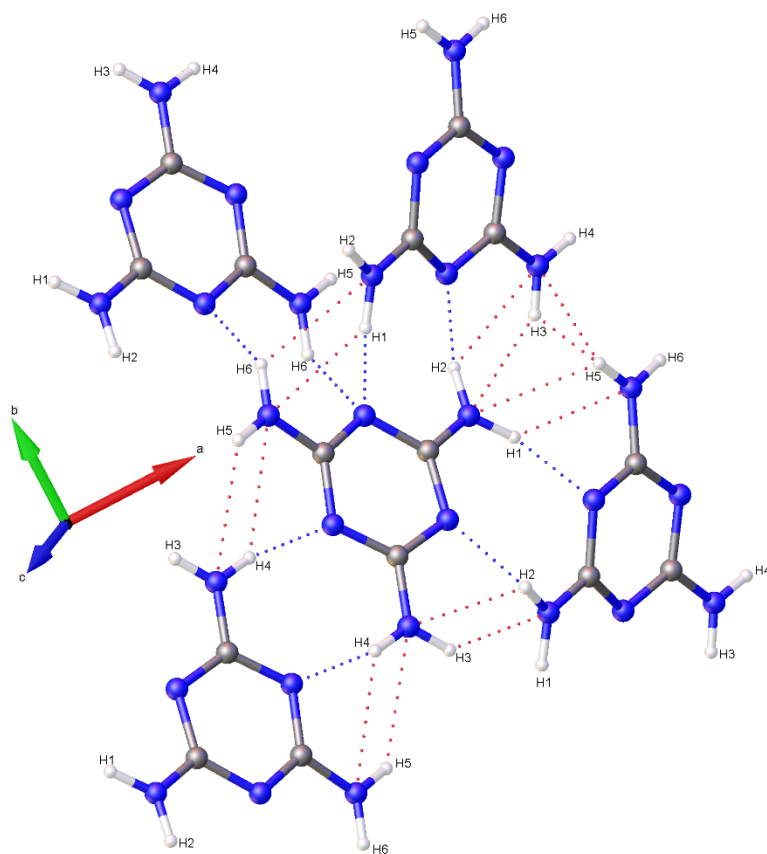
demonstrated that pyrolysis of melamine at 2.5 GPa and 800°C in the presence of hydrazine leads to formation of a bidimensional honeycomb-type structure close to those expected for the theoretical graphitic-like g-C<sub>3</sub>N<sub>4</sub>. Similar syntheses successfully producing g-C<sub>3</sub>N<sub>4</sub> and closely related byproducts utilizing pure melamine have also been achieved [225, 227]. Synthesis of C-N nanotubes was also observed in high-pressure catalytic pyrolysis of melamine with NaN<sub>3</sub>-Fe-Ni at 35 MPa and 650°C [228]. Interestingly, another recent high-pressure pyrolysis experiments at 5 GPa and 800°C showed formation of a different molecular crystalline monoclinic solid [229].

Given the complexity of coupled high temperature and pressure pyrolysis, a good starting point for understanding the reaction potential of melamine is through a thorough examination of the compression mechanism. One of the first high-pressure studies of melamine to 4.0 GPa utilized infrared spectroscopy [230], and while noting a number of important band frequency shifts, it did not report any discontinuous changes in the compression behavior. In contrast, a Raman study to 8.7 GPa in alcohol pressure medium reported discontinuities in the pressure-dependence of some modes, possibly indicating two phase transitions at 2 and 6 GPa [231]. Indeed, a later synchrotron energy dispersive (ED-XRD) powder diffraction study to 14.7 GPa in alcohol pressure medium [232] seemed to confirm the notion of the two low pressure phase transitions, where a new triclinic phase was suggested to form at 1.3 GPa, and transform to an orthorhombic polymorph above 8.2 GPa. The resolution and sensitivity of the ED-XRD experiments, however, were not sufficient to constrain the structures of the new phases, as less than 10 indexable diffraction peaks were observed. Recently, Liu et al. [233] carried out a Raman spectroscopy experiment with melamine powder without pressure medium to 25 GPa, but did not confirm any of the earlier reported discontinuities. A soft mode behavior was observed for one of the N-H vibrations, and N-H vibration peaks gradually disappeared above 10 GPa. A detailed Raman, far-IR, and angular-dispersive X-ray diffraction study conducted by Galley et al. reported three potential phase transitions of powdered melamine with KBr as a pressure-transmitting medium, two of which were observed previously [232, 234], with an additional high-pressure phase forming at 16 GPa. As with previous spectroscopic studies it was observed that the modes associated with N-H stretching, particularly at 3116 and 3325 cm<sup>-1</sup>, broaden significantly with pressure.

(a)



(b)



*From previous page: Figure 5.1. Hydrogen bonding network of melamine at (a) low (0.96(5) GPa) and (b) high (36.2(1) GPa) pressures. Potential hydrogen bonding interactions between anti-parallel amino N-H groups induced by pressure are displayed in red. Bonds behind and in front of the plane of view are omitted for clarity.*

This study also documented irreversible amorphization of the sample, attributed to weakening of the internal bonds, which could foster polymerization of the sample. In each of these previous experiments, the effects of non-hydrostatic stress, hydrogen-bond interactions between melamine and polar solvent-based pressure media, or inter-grain interactions exist. In order to re-examine the details of compression behavior of melamine and reconcile the different results of previous studies we have conducted a combined X-ray diffraction and Raman spectroscopy investigation using high quality single crystal samples in quasihydrostatic noble gas pressure transmitting media.

## **5.2 MATERIALS AND METHODS**

The high-pressure X-ray diffraction and Raman spectroscopy experiments took place over several experimental sessions between 2010 and 2015, where experiments were conducted at the Advanced Photon Source (APS) at Argonne National Laboratory. Data were collected at the 13-IDB and 16-IDB beamlines of GeoSoilEnviro-CARS (GSECARS) and the High Pressure Collaborative Access Team (HPCAT), with gas-loading of diamond anvil cells and Raman measurements conducted at GSECARS [186]. Prior to each experiment, melamine powder of >99% purity was recrystallized from saturated aqueous solution, and crystals approximately 10x30x30  $\mu\text{m}$  in diameter were loaded into symmetric type diamond anvil cell equipped with conical Boehler-Almax type anvils and backing plates [113]. These crystals were accompanied by chips of ruby as a pressure calibrant, with helium (2010) or neon (2015) as a pressure transmitting medium. Diffraction data were collected with Kickpatrick-Baez mirror-focused monochromatic X-rays ( $\lambda=0.3344$  at GSECARS and  $0.4066 \text{ \AA}$  at HPCAT), focused onto the sample crystals. At each pressure point, the sample was rotated during X-ray exposure around the  $\omega$ -axis of the instrument, with diffraction images collected at three detector positions, each perpendicular to the x-ray beam, and differing by 7 cm detector translation. For the 2015 experiment, the internal pressure was changed without removing the cell from the instrument, using a gas-driven membrane device with a Druck PACE 5000 electronic valve controller.

Pressure was measured by the ruby fluorescence method [101] during pressurization and after a complete diffraction data set was collected.

Diffraction images collected during each experiment were analyzed using the ATREX IDL software package [146], where peak intensities were corrected for Lorenz and polarization effects. Peaks were indexed using cell\_now [235], while the orientation matrix was refined and unit cell parameters were obtained using RSV [146]. Integrated peak intensities were used for the structure refinement. Refinements were conducted using SHELXL [142] with isotropic atomic displacement parameters and full site occupancies for all atoms. Amino hydrogens were constrained using the riding hydrogen model of AFIX 94, preventing the H-N-H angle from varying from 120°, but allowing some variance in the N-H bond distance and no limitations on the rotation angle of each amino group. Due to limitations on accurately reporting donor-hydrogen distances determined by X-ray diffraction, donor-acceptor distances are primarily used to gauge intermolecular interactions. No additional constraints or restraints were utilized to fix bond distances or the character of the central triazine ring. Equation of state results, such as bulk modulus and its pressure derivatives ( $K$  and  $K'$ ), as well as linear compressibilities were determined with EOSFit7-GUI [188], fitting experimental unit cell values with a third-order Vinet equation of state [236, 237]. Additional analysis, including hydrogen bond geometries and Hirshfeld surface generation, was conducted using Olex<sup>2</sup> [238] and CrystalExplorer [239], respectively.

For Raman experiments, a separate symmetric Princeton-type diamond anvil cell was prepared. We used low-fluorescence, modified brilliant cut diamond anvils with 0.3 mm culets, mounted on WC backing plates. The gasket preparation technique was identical to the one used for the X-ray diffraction experiments. One good optical quality, single crystal of melamine, approximately 15x50x50  $\mu\text{m}$ , and two small ruby spheres were loaded in neon pressure medium. Raman spectra were collected over a total spectral range of 250-3700 relative  $\text{cm}^{-1}$  with a holographic 1800 gr/mm grating, utilizing the green line of a 200 mW Ar<sup>+</sup> laser ( $\lambda = 514.532$  nm) for excitation, and a Horiba Triax 550 Spectrograph, equipped with a liquid nitrogen-cooled Princeton Instruments CCD detector, at the GSECARS Raman Spectroscopy Lab. Sample Raman spectra were collected every 3-5 GPa from 1 GPa up to 33.1(1) GPa in three separate spectral ranges of 250-1200 relative  $\text{cm}^{-1}$ , 1400-1900 relative  $\text{cm}^{-1}$ , and 3100-3650 relative  $\text{cm}^{-1}$ .

Raman data were processed in Spectragryph 1.2.8 [240], where individual adaptive baseline subtractions were applied to each spectrum to better compare between pressure steps.

## 5.3. RESULTS

### 5.3.1 X-Ray Diffraction

After initial compression and gas-loading with helium to 0.96(5) GPa, the unit cell parameters of melamine were  $a = 10.410(6)$  Å,  $b = 7.465(2)$  Å,  $c = 7.086(6)$  Å, and  $\beta = 113.89(4)^\circ$  in the space group setting of  $P2_1/a$ . Multiple data sets, between 2010 and 2015, provide nineteen pressure points where the compressional effects on the structure of melamine was observed. All nineteen data points were used for equation of state fitting, whereas seventeen were of sufficient data quality to permit hydrogen bonding geometry analysis. The crystal structures obtained during the compression pathway show little deviation in the overall molecular geometry with pressure. At 0.96(5) GPa, each individual melamine unit is connected to its neighbors via eight N-H $\cdots$ N hydrogen bonds, as is the case at ambient pressure, forming layers of melamine molecules, approximately parallel to (010), that are hydrogen bonded within, and also linked to neighboring layers (Fig. 5.1.a). Additionally, in neighboring layers, there are pairs of melamine molecules whose central rings lie within parallel planes and overlap. Neighboring pairs of molecules are offset by 33.8(9) degrees, forming the corrugated structural motif. With each pressure step up to 36.2(1) GPa, full structure refinement was conducted, initially based on the structure of melamine reported from ambient pressure neutron diffraction experiments [241]. Selected data collection and refinement information from initial and final pressure steps for this structure are listed in Table 5.1. The evolution of unit cell parameters with pressure is listed in Table 5.2. Additional information, including fractional atomic coordinates, symmetry operators, and selected bond lengths and angles are listed in appendix Tables A1 to A4. On compression beyond 36.2(1) GPa in helium or 31.8(1) GPa in neon, a reversible phase transition to a twinned triclinic polymorph (where  $a = 6.08(1)$  Å,  $b = 7.267(2)$  Å,  $c = 7.82(1)$  Å, and  $\alpha = 78.25(4)^\circ$ ,  $\beta = 80.1(2)^\circ$ ,  $\gamma = 80.48(4)^\circ$  at 38.9(1) GPa) was seen, with pronounced changes in the diffraction pattern, as shown in Figure 5.2. This transition was reversible, however, further compression past approximately 45 GPa in helium resulted in irreversible amorphization, accompanied by loss of diffraction signal and easily identifiable change of the color and opacity of the crystal (Fig 5.3).

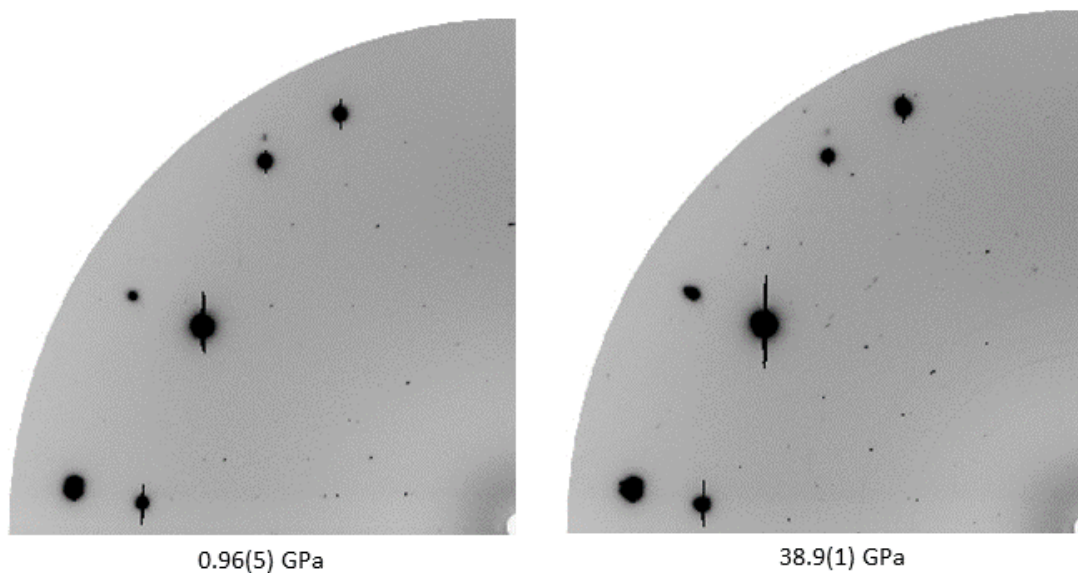


Figure 5.2. Diffraction patterns at the central detector position of low- and high-pressure phases of melamine, displaying the change in pattern before and after the reversible structural phase transition above 36 GPa in helium.

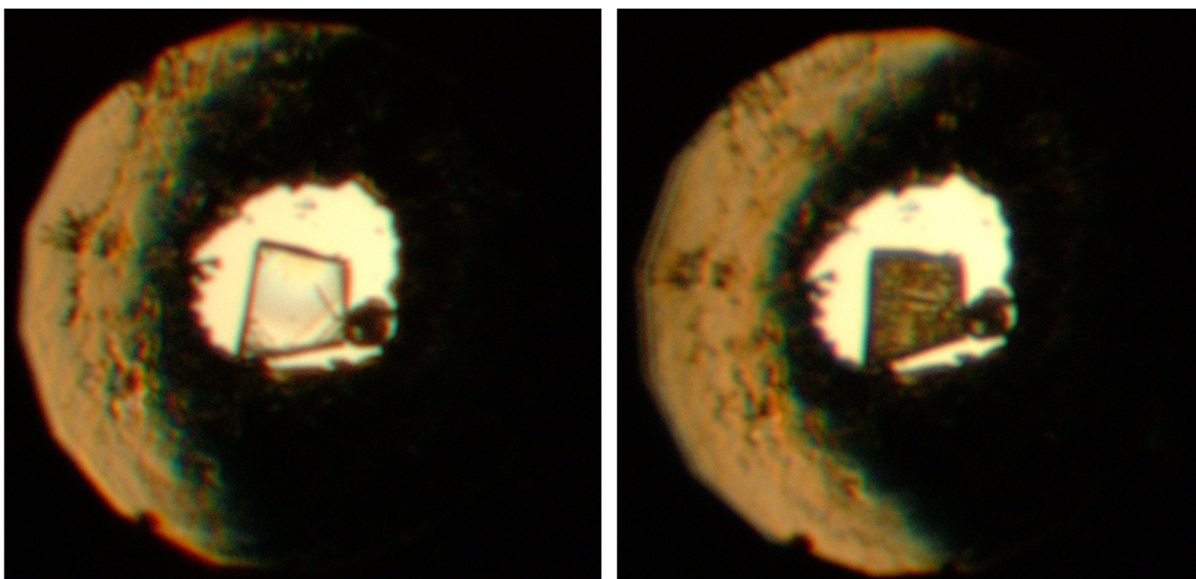


Figure 5.3. Visible changes in a melamine crystal before (left) and after (right) the irreversible high-pressure amorphization at 45 GPa in helium.

Table 5.1. Selected data collection and refinement details from lowest and highest pressure points. The opening angle of the diamond anvil cell in the 2015\_10 experiment was larger by 20° compared to the 2010\_1 experiment, producing higher number of observed peaks.

2010_1 (0.96(5) GPa)		2015_10 (36.2(1) GPa)	
No. of reflections collected	453	No. of reflections collected	654
No. of independent reflections	186	No. of independent reflections	221
R <sub>int</sub>	0.1272	R <sub>int</sub>	0.0944
R[F <sup>2</sup> > 4σ(F <sup>2</sup> )]	0.0611	R[F <sup>2</sup> > 4σ(F <sup>2</sup> )]	0.0700
wR(F <sup>2</sup> )	0.1396	wR(F <sup>2</sup> )	0.1652
Goodness-of-fit	1.114	Goodness-of-fit	1.231
No. of parameters refined	40	No. of parameters refined	40
No. of restraints used	0	No. of restraints used	0

### 5.3.2 Equation of State and Bond Compressibility

Previously, Ma et al. [232] documented the P-V equation of state of melamine, but only to approximately 15 GPa. Although that study describes a transformation to a triclinic structure below 2 GPa, there exist similarities between that study and the current results. In both cases, there is a precipitous drop in the unit cell volume below 5 GPa. However, in the present study, there is no evidence of a phase transformation. Rather, there is a smooth and continuous reduction in the unit cell volume that is well described by the Vinet equation of state [236, 237]:

$$P = 3K_0 \frac{(1 - f_V)}{f_V^2} e^{\left(\frac{3}{2}(K' - 1)(1 - f_V)\right)}$$

where  $f_V = (V/V_0)^{1/3}$ ,  $V_0$  is the initial cell volume,  $K_0$  is the isothermal bulk modulus, and  $K'$  is its derivative when the pressure is equal to zero. The output of this equation of state, with  $V_0$  fixed to the ambiently determined value of 536.7(2) Å<sup>3</sup>, is  $K_0 = 12.9(8)$  GPa, and  $K' = 7.4(3)$ . The linear axial compressibilities (defined as  $\beta_{10} = 1/3K_{10}$ ) [149] were determined using a linearized version of the Vinet equation. The increase of the unit cell's  $\beta$  angle was well-described by a three-parameter exponential rise-to-maximum function. The progression of each of these values with pressure can be seen in Figures 5.4 and 5.5. By 36.2(1) GPa the unit cell volume has experienced a 40 percent collapse, driven primarily by the shortening of the  $a$  and  $c$  axes. As each axis shrinks the  $\beta$  angle opens, reflecting the shift of molecules with respect to one another, rising to a predicted maximum of 120.7(1) degrees at 40 GPa.

When comparing the bulk moduli with other common six-membered ring molecules such as benzene (5.5 GPa) or aniline (5.44 GPa), as well as extended structures with ring motifs such as graphite (33.8 GPa), the compressibility of melamine is closer to the former [85, 87, 242]. This can be readily explained by the type of dominating intermolecular interactions and arrangement of molecules with respect to each other, where graphite is held more rigidly in covalently-bonded planar sheets, while individual benzene or aniline molecules are not covalently bonded to their neighbors. Both polymorphs of aniline also form extended stacked layers held together by hydrogen bonding, where its singular amino group participates in N-H $\cdots$ N and N-H $\cdots$  $\pi$  hydrogen bonds [87, 90]. Individual aniline molecular units do not experience significant structural or energetic modification in pressure, yet their hydrogen bonds decrease in length to the point of destabilization [90]. Benzene does not share hydrogen atoms below a theorized point of metallization [85, 86], and  $\pi$ - $\pi$  interactions act as the driving intermolecular interaction with increasing pressure. For solid benzene-III, a recent theoretical study [86] suggested that at 50 GPa, despite an almost two-fold reduction in unit cell volume, the intramolecular bond lengths stay basically unchanged. A similar situation appears to occur with melamine: while the

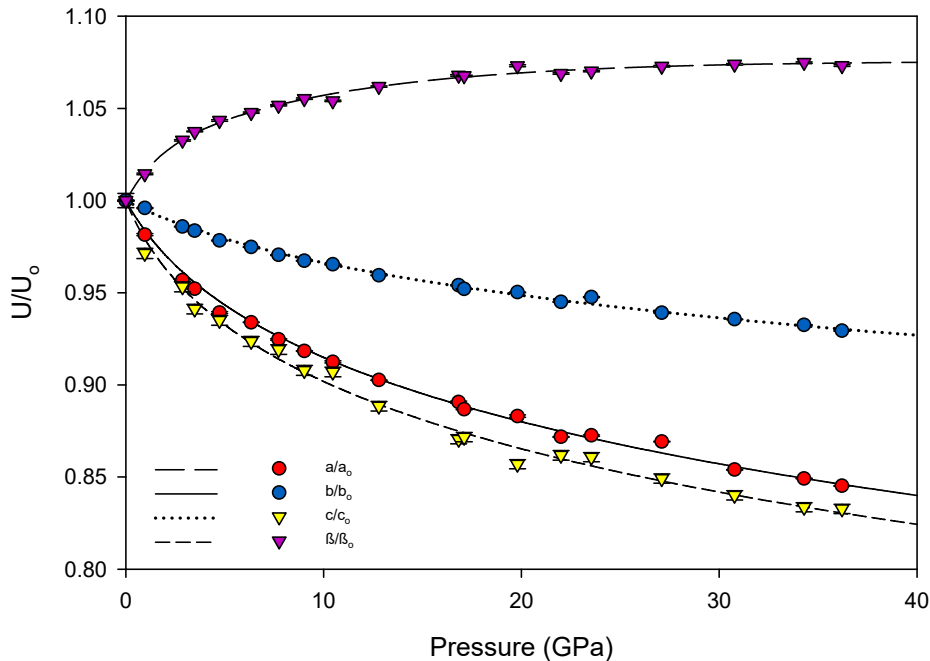


Figure 5.4. Evolution of normalized unit cell parameters of melamine with pressure. Linear axial compressibilities are  $\beta_{a0} = 6.54(5) \times 10^{-3} \text{ GPa}^{-1}$ ,  $\beta_{b0} = 1.89(1) \times 10^{-3} \text{ GPa}^{-1}$ , and  $\beta_{c0} = 9.0(1) \times 10^{-3} \text{ GPa}^{-1}$ .

intramolecular deformation is minimal, intermolecular hydrogen bonds accommodate pressure changes within the crystal without departing from the original space group and basic structure.

*Table 5.2. Unit cell parameters as a function of pressure. 2010 data were collected in Ne, 2015 data in He.*

<b>Data set</b>	<b>P (GPa)</b>	<b>a (Å)</b>	<b>b (Å)</b>	<b>c (Å)</b>	<b>β (°)</b>	<b>V (Å<sup>3</sup>)</b>
2010	10 <sup>-4</sup>	10.606(1)	7.495(1)	7.295(2)	112.26(2)	536.7(2)
2010	0.96(5)	10.410(6)	7.465(2)	7.086(6)	113.90(4)	503.5(6)
2010	2.9(1)	10.148(6)	7.389(2)	6.954(6)	115.93(4)	468.9(5)
2015	3.5(1)	10.099(1)	7.372(1)	6.866(1)	116.47(1)	457.6(6)
2010	4.7(1)	9.962(6)	7.333(2)	6.821(6)	117.14(4)	443.4(5)
2015	6.3(1)	9.906(1)	7.306(1)	6.737(6)	117.62(3)	432.0(4)
2010	7.7(1)	9.807(4)	7.274(1)	6.705(4)	118.07(3)	422.0(4)
2015	9.0(1)	9.740(1)	7.250(1)	6.623(7)	118.47(4)	411.1(5)
2010	10.5(1)	9.678(6)	7.235(1)	6.616(5)	118.34(4)	407.8(4)
2015	12.8(1)	9.572(1)	7.191(1)	6.481(6)	119.21(3)	389.4(4)
2010	16.8(1)	9.446(6)	7.151(2)	6.350(5)	119.89(4)	371.9(4)
2015	17.1(1)	9.404(1)	7.136(1)	6.359(6)	119.86(4)	370.1(4)
2010	19.8(1)	9.366(7)	7.122(7)	6.252(6)	120.47(5)	359.4(5)
2015	22.0(1)	9.246(1)	7.083(1)	6.287(7)	120.00(4)	356.6(4)
2010	23.5(1)	9.254(4)	7.103(4)	6.279(4)	120.14(3)	356.9(3)
2015	27.1(1)	9.219(1)	7.039(1)	6.195(7)	120.44(5)	346.6(4)
2015	30.8(1)	9.057(2)	7.013(1)	6.128(7)	120.57(5)	335.1(4)
2015	34.3(1)	9.006(1)	6.990(1)	6.081(7)	120.67(4)	329.3(4)
2015	36.2(1)	8.965(1)	6.966(1)	6.075(7)	120.48(5)	326.9(4)

In comparison to energetic materials, the bulk modulus of melamine is analogous to or slightly less than  $\beta$ -HMX (12.4 GPa),  $\alpha$ -RDX (13.9 GPa), and TATB (16.2 GPa) [243]. Interestingly, these values were obtained using powder x-ray diffraction techniques in methanol-ethanol-water, argon, and hexane pressure media, respectively [244-246]. The use of powders, as well as non-hydrostatic and non-inert pressure media likely introduces similar uncertainties and irregularities as those encountered with prior high-pressure experiments of melamine. Significant variations in compressibility for these compounds, including elastic constants and phase transformation behavior, have been shown to greatly depend on the hydrostatic character of the pressure media [99, 247]. Hydrogen bonding has also been demonstrated to be the driving interaction in crystalline networks of RDX and TATB, where intermolecular hydrogen bonding networks could be disrupted by participating polar-solvent pressure media or inter-grain boundaries [94]; when compressional hydrostaticity is ensured, highly energetic molecules like TATB have been shown to remain crystalline past 100 GPa [248].

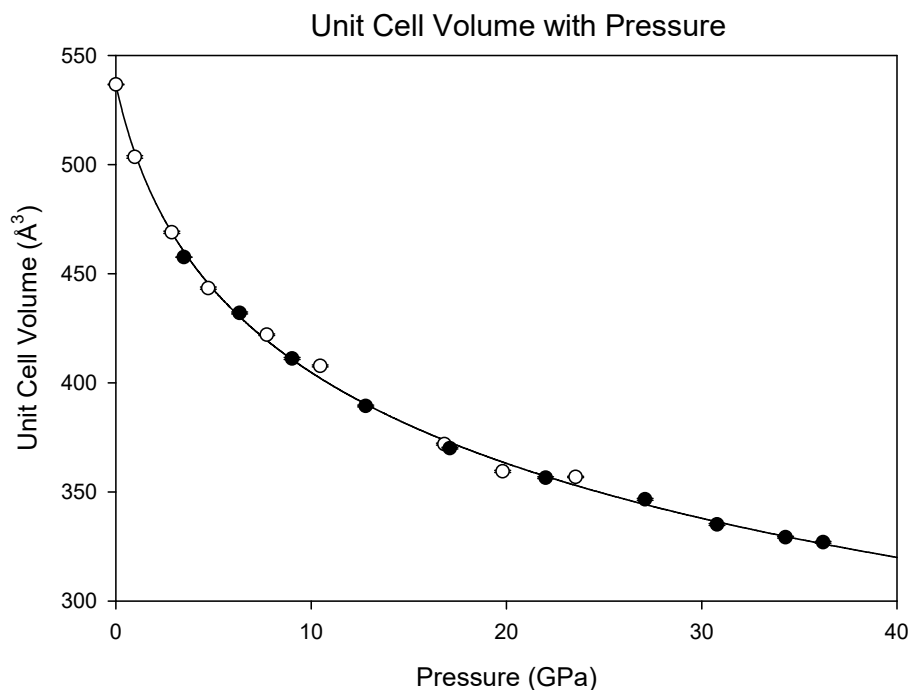


Figure 5.5. Evolution of unit cell volume of melamine with pressure. Data points were fitted with a third-order Vinet equation of state,  $V_0 = 536.7(2) \text{ \AA}^3$ ,  $K_0 = 12.9(8) \text{ GPa}$ , and  $K' = 7.4(3)$ . Open circles indicate 2010 data collected in Ne, filled circles indicate 2015 data collected in He.

For inorganic substances and minerals, a very common notion for understanding a compression mechanism is the Rigid Unit Mode model, in which it is assumed that each subunit (i.e., a tetrahedron or octahedron) is very stiff compared to the framework in which it resides [249]. As a result, rotation of whole units is preferable to alteration of bond lengths within a unit. Although it is an organic molecule, within this frame of reference melamine subunits (primarily the aromatic *s*-triazine ring and amine nitrogen) can be considered as the inflexible subunit, and are relatively unchanged with pressure. In contrast, intermolecular hydrogen bonds greatly compress and shift position with pressure, and individual NH<sub>2</sub> units have some ability to rotate, in order to accommodate pressure changes and avoid repulsive H-H interactions. This is evident from the relative lack of change in carbon-nitrogen bond lengths with substantial increases in pressure, as shown in Fig. 5.6; for both ring and amine carbon-nitrogen bonds, the bond length decrease is less than about 0.05 Å, while the donor-acceptor lengths of hydrogen bonds decrease by nearly 0.5 Å over the same compression path.

The compressional behavior of melamine from the perspective of an individual molecular unit can also be visualized through Hirshfeld surfaces. This method of crystal analysis condenses properties such as interatomic angles and distances, crystal packing schemes, and intermolecular

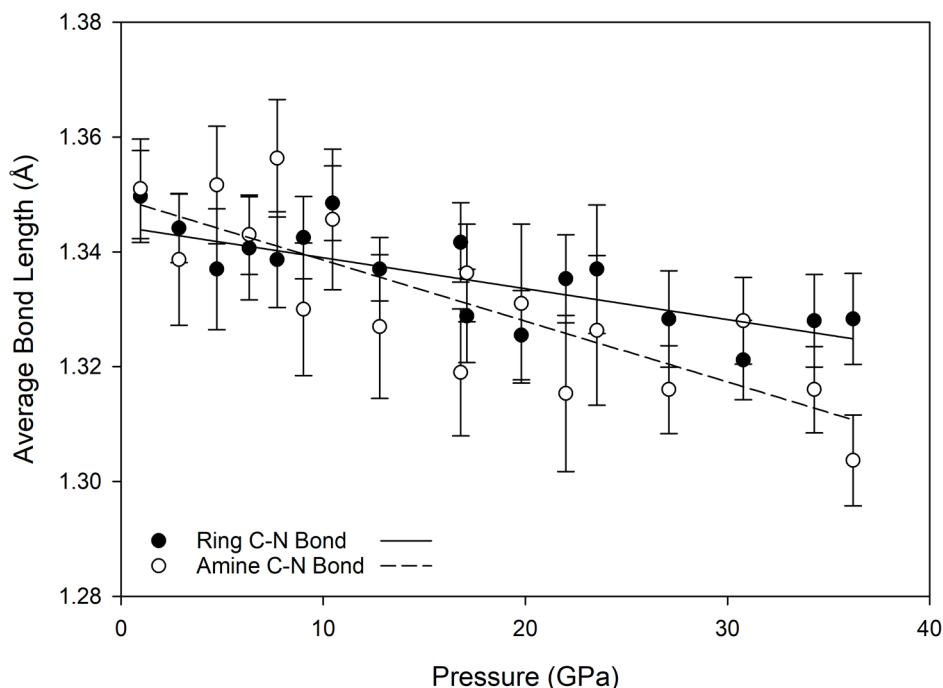


Figure 5.6. Average carbon-nitrogen bond lengths for ring and amine components of melamine. Each follows a loosely linear decrease in length with pressure.

interactions into models that can be easily and qualitatively interpreted, yet are derived from quantitative analysis [250, 251]. Hirshfeld surfaces are differentiated from other molecular surface representations such as electron density maps or van der Waals surfaces by accounting for both a molecule and its proximity to its nearest neighbors, making it well-suited for the analysis of molecular crystals. Two surfaces, the shape index and normalized contact distance ( $d_{\text{norm}}$ ), are particularly useful for describing the packing of molecular crystals such as melamine. The shape index is a Hirshfeld surface that identifies concave or convex areas of a molecule's surface based on charge density. Red areas indicate concave areas, whereas blue indicates convex. For the purpose of examining compressional behavior, any change in the intramolecular geometry is distinguishable by changes in color. For melamine, the relative lack of change between low and high pressure is apparent (Fig. 5.7), mirroring the small changes in covalent bond lengths and overall inflexibility of the aromatic component with pressure.

Hirshfeld surfaces of the normalized contact distances tell the other half of the story; this parameter describes the internal ( $d_i$ ) and external ( $d_e$ ) contact distances of the Hirshfeld surface to the nearest atomic nucleus, normalized by the van der Waals (vdW) radii of the atoms involved. The result is a surface where intermolecular contacts longer than the sum of the atoms' vdW radii are displayed in blue, and contacts shorter than the vdW radii are displayed in red. At low pressures, this highlights the points of contact for the N-H $\cdots$ N hydrogen bonds, where the bond contracts the intermolecular distance. As pressure increases, contact points with distances shorter than the vdW radii appear on the previously non-interacting amine nitrogen and atoms of the central ring.

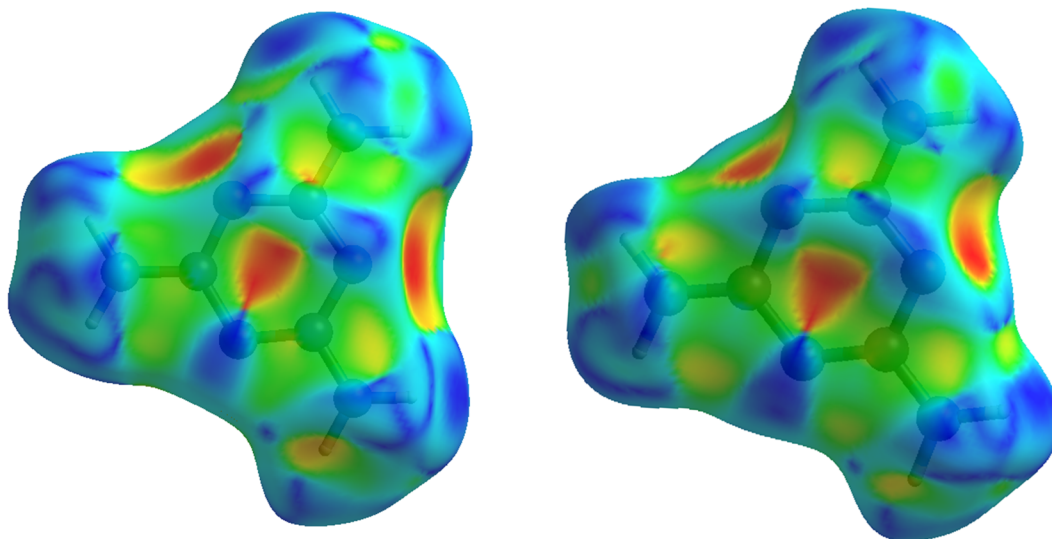


Figure 5.7. Hirshfeld surfaces displaying the shape index of melamine at low (0.96(5) GPa, left) and high (36.2(1) GPa, right) pressures. Concave areas, shown in red, correspond to areas where a complimentary neighboring molecule may interact.

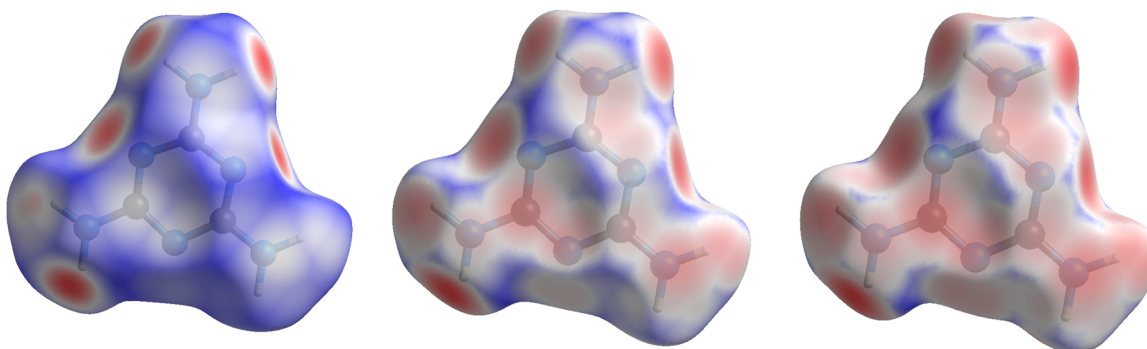


Figure 5.8. Hirshfeld surfaces displaying  $d_{norm}$  at 0.96(5), 17.1(1), and 36.2(1) GPa. As pressure increases, intermolecular contacts are induced, primarily as new hydrogen bonds.

### 5.3.3 Hydrogen Bonding Behavior with Pressure

At ambient and low-pressure conditions, individual melamine molecules are linked with neighbors through pairs of complementary hydrogen bonds connecting amino hydrogens exclusively to ring-based nitrogen atoms. In previous ambient-pressure X-ray and neutron diffraction studies, it was observed that of the six symmetry independent hydrogen atoms in  $\text{NH}_2$  groups, only four strongly participate in hydrogen bonding [241]. The two remaining hydrogen atoms are subject to hindrances that prevent strong hydrogen bonding interactions, and are denoted in this study as H3 and H5. In the case of H5, the hydrogen atom is in close contact with another H5 on a neighboring molecule, and repulsive interaction occurs as distance decreases. For H3, steric hindrance prevents it from being sufficiently close to a ring nitrogen acceptor atom, allowing only weak interaction with a  $\text{NH}_2$  group on a neighboring molecule. Each ring nitrogen atom also acts as a hydrogen bond acceptor for a total of four bonds per ring, with one nitrogen (denoted here as N4) acting as acceptor for two bonds (Fig. 5.1a).

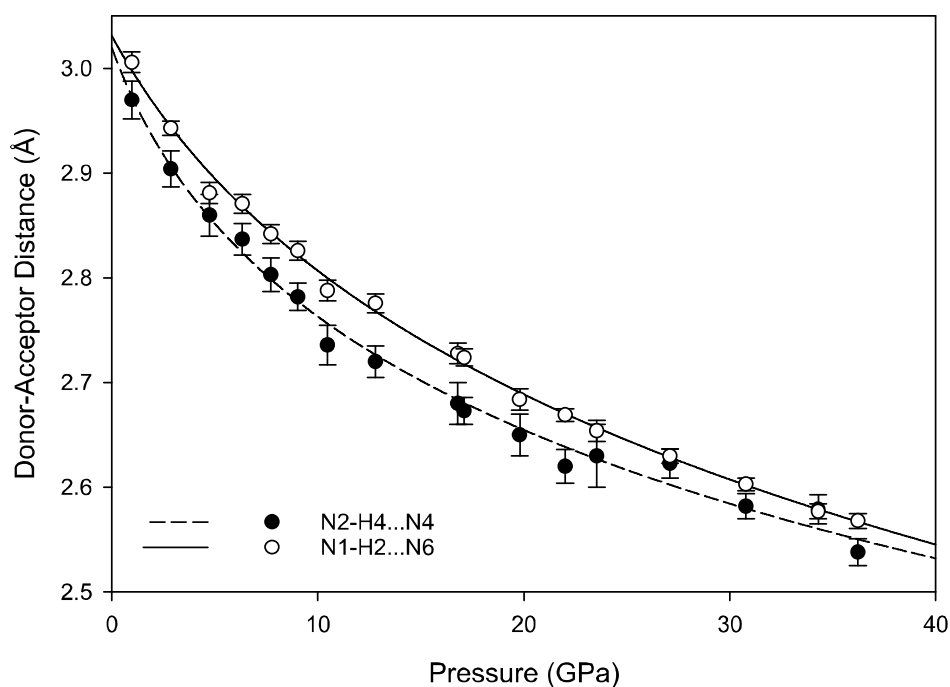


Figure 5.9. Intra-plane hydrogen bond  $D\cdots A$  distance as a function of pressure, fitted with a third-order polynomial function.

The hydrogen bonds in melamine can also be distinguished by whether they link molecules within a given corrugated plane or between them; for instance, the decrease in donor-acceptor distance for intra-plane molecules decreases smoothly as a function of pressure akin to the behavior of the unit cell parameters, while the inter-plane behavior is less consistent (Fig. 5.9, 5.10). This is likely caused by the larger influence of the intra-plane bonding, as there are more hydrogen bonds within a layer, as well as small amounts of rotation and torsion to accommodate the increased intra-layer bonding and repulsive interactions between close-contact hydrogens. Ultimately, the intermolecular hydrogen bonds are capable of significant shortening with response to pressure, without any significant changes in the pattern of the original hydrogen bonds. Compression through 36.2(1) GPa decreases donor-acceptor distances substantially, which increases the covalent character of a bond and increases its strength [1].

Notably, none of the original hydrogen bonds present at ambient pressures are broken below the phase transition pressure; instead, new hydrogen bonds between amino hydrogens and ring nitrogens form by 9.0(1) GPa and persist until at least 36.2(1) GPa (Fig 11). As pressure increases further, amino groups are pushed into close contact with one another, and interactions between oppositely aligned N-H atoms occur as each hydrogen is brought closer to an opposing

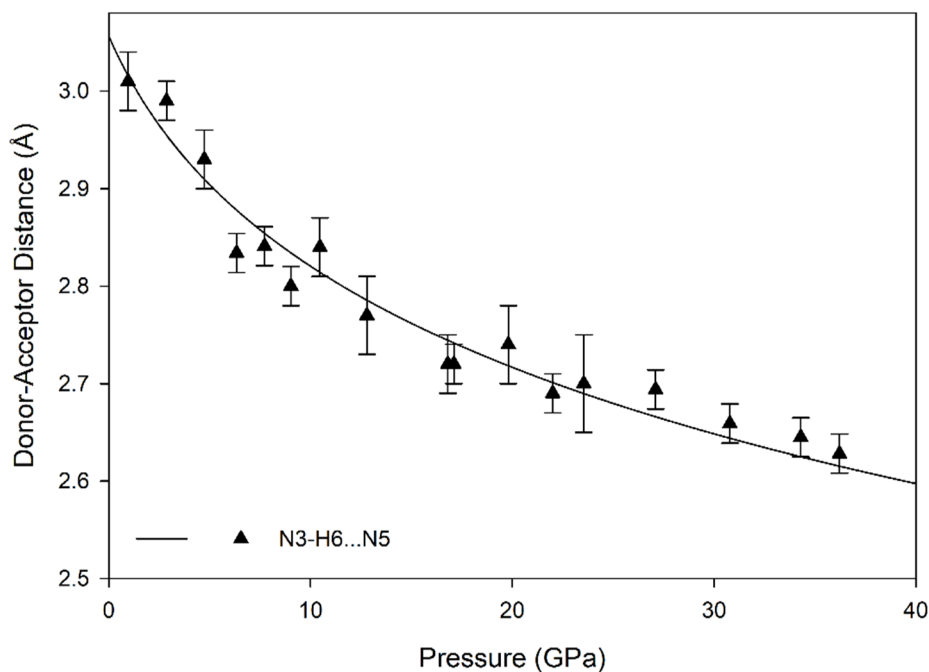


Figure 5.10. Inter-plane hydrogen bond  $D\cdots A$  distance as a function of pressure, fitted with a third-order polynomial function.

nitrogen's lone pair of electrons. These interactions, although primarily electrostatic in character, are stabilized by their anti-parallel orientation to one another, with pressure overriding unfavorably shallow D-H-A angles, steric crowding, and repulsive interactions. At 36.2(1) GPa, sufficiently short bond distances indicate bi- and trifurcation of these bonds, as shown in Fig. 5.1b, by the previously un-bonded H3 and H5 atoms.

The new pressure-induced hydrogen bonds are not sufficiently strong to create a stable high-pressure configuration, as the transformation between monoclinic and triclinic phases is reversible. However, the new pressure-induced hydrogen bonds with ring nitrogen atoms may foster changes in the intermolecular interactions of  $\pi$  electrons in the high pressure phase; at ambient conditions, inter-layer hydrogen bonds link molecules where the centroid planes of the rings are parallel to one another, resulting in a skewed parallel-displaced arrangement where an electron-rich ring nitrogen is roughly aligned with a moderately electron-deficient ring center. At high pressures, the new hydrogen bonds also link molecules whose planes are at an offset to one another, introducing an interaction between these rings not experienced at lower pressures. Furthermore, compression reduces the distance and shift between the ring centroids, as well as reducing the angle between offset pairs of molecules (Fig. 5.12), increasing the likelihood of extended interactions between multiple pairs of molecules. Although the term " $\pi$ - $\pi$  stacking" does not correctly describe the contact between neighboring melamine molecules [252, 253], the distances and angles between ring centroids are within limits for attractive electrostatic  $\pi$ - $\sigma$  interactions at both ambient and high pressures [252, 254, 255]. However, the N-H $\cdots$ N hydrogen bonds ultimately direct the supramolecular changes in the melamine crystal; this provides exceptional stability when compared to un-substituted *s*-triazine, which does not have the ability to act as a hydrogen bond donor [15, 96, 252].

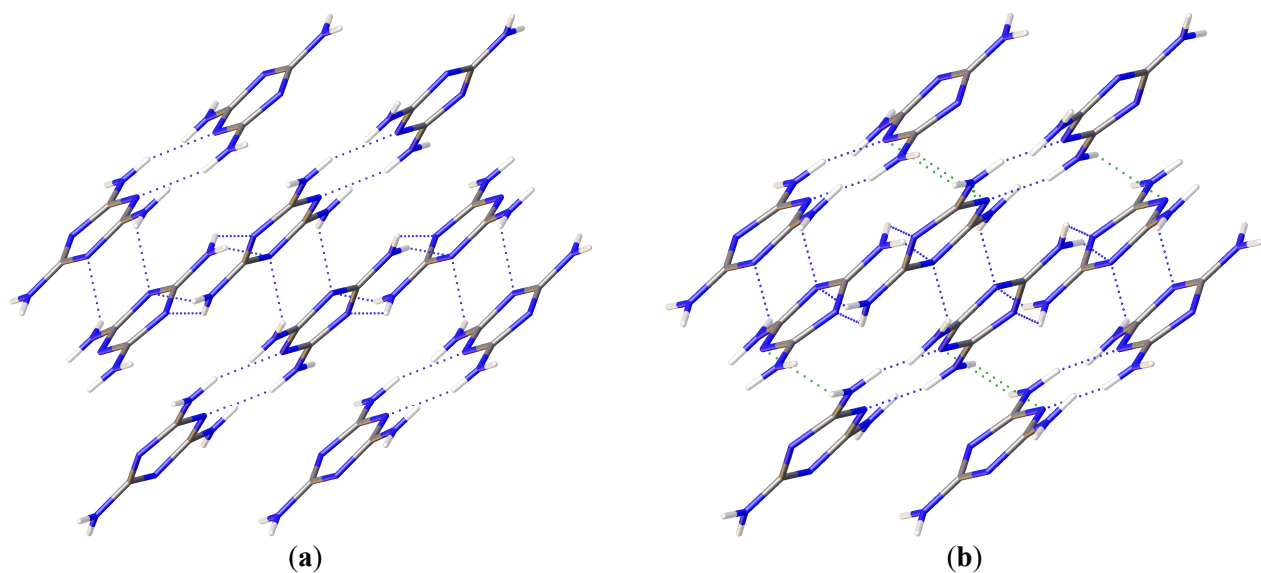


Figure 5.11. Hydrogen bonding network of melamine at (a) low (0.96(5) GPa) and (b) high (36.2(1) GPa) pressures, as viewed down  $\langle 010 \rangle$ , displaying the layered structure. New hydrogen bonds to the central ring have been highlighted in green. Some bonds, including weak amino N-H interactions, have been omitted for clarity.

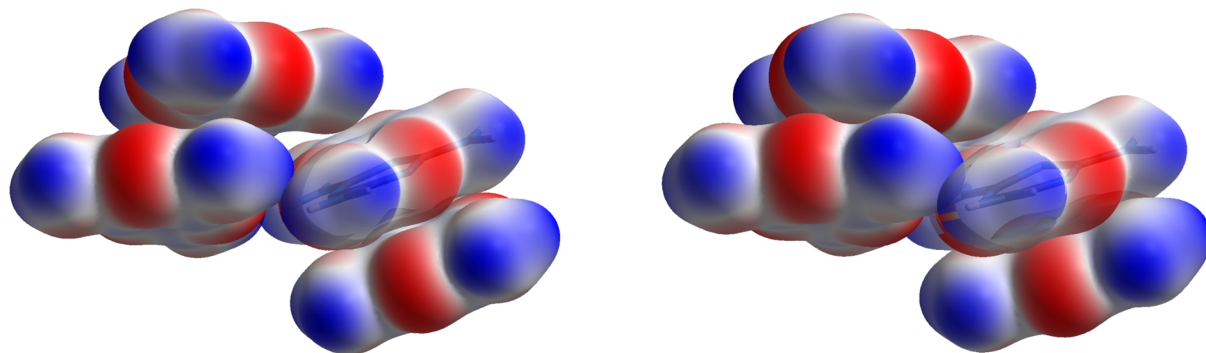


Figure 5.12. Electrostatic potential surfaces of neighboring melamine molecules at 6.3(1) (left) and 36.2(1) (right) GPa, scaled from -0.0928 to 0.1388 au. Regions in red are electron-rich, while regions in blue are electron deficient. With pressure, distance between melamine ring centroids oriented in parallel planes decreases, and the offset angle to the next pair of molecules decreases.

### 5.3.4 Raman spectroscopy

In general, Raman spectroscopy is an excellent tool for detecting pressure-induced structural phase transitions in solids, which usually manifest themselves as discontinuous changes in vibration mode behavior. For instance, symmetry lowering related to displacive phase transitions typically results in splitting of Raman peaks. The case of molecular crystals, however, is often more complicated than simple inorganic solids. The starting crystal symmetry is often lower, and the number of Raman modes can be very significant. At the same time, there are more types of competing interatomic and intermolecular interactions (e.g. hydrogen bonds, van der Waals forces, electrostatic interactions, charge transfer), which affect the vibration force constants. At high pressure the balance between these various interactions changes and may cause discontinuities in the Raman mode behavior unrelated to structural phase transitions. An example of such was found in benzene, for which Raman experiments [256] described the existence of phase transitions between the II-III and III-IV phases at about 4 and 11 GPa respectively. However, later studies combining both IR spectroscopy and powder X-ray diffraction cast doubt on this proposed transition, as the observed discontinuities and changes in vibrational modes did not correspond to symmetry-altering structural changes [85].

The ambient pressure Raman spectrum of melamine was first quantitatively interpreted in terms of mode assignment by Schneider and Schrader [257]. The assignment of the collective ring vibration modes can be made by analogy to the unsubstituted parent-molecule of *s*-triazine [258]. There are also several recent Raman studies of solid salts of melamine [259, 260] that are useful in interpretation of individual vibration modes, such as those from hydrogen bonds. In the spectral range covered by our experiments, the Raman spectrum of melamine can be divided into three regions: the 250-1200  $\text{cm}^{-1}$  is the collective ring vibration mode region, from 1400-1900  $\text{cm}^{-1}$  is the C-NH<sub>2</sub> vibration mode range, and the 3000-3700  $\text{cm}^{-1}$  range is the N-H vibration mode range. This last region proves to be the most informative; at ambient pressure there are four distinct Raman peaks, at 3128, 3333, 3420, and 3471  $\text{cm}^{-1}$  [233]. The two peaks at lower wavenumbers are very broad and quite asymmetric, whereas the peaks at higher wavenumbers are sharp and symmetric, as seen in Fig. 5.13.

The non-uniformity of the hydrogen bonding interactions can also be seen in the Raman spectra. The sharp Raman peaks of 3420 and 3471  $\text{cm}^{-1}$  at close to ambient pressure conditions

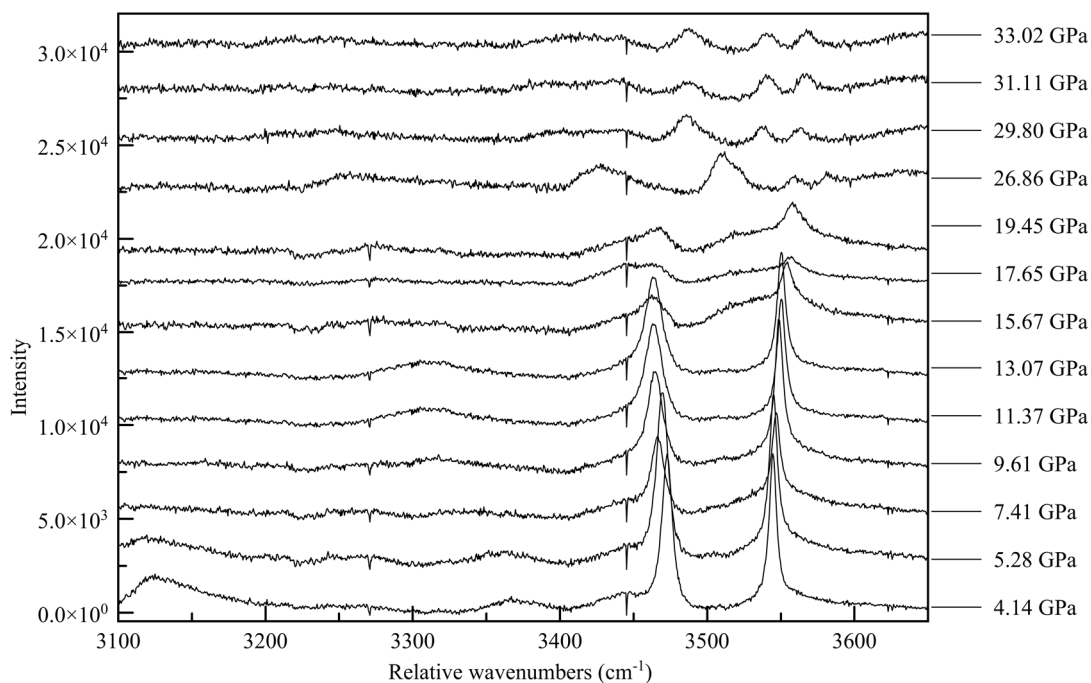


*Figure 5.13. Raman spectra of melamine in N-H vibration region, vertical offset indicates sequential pressure steps in GPa, as shown on the right vertical axis. Intensity is arbitrary with vertical stacking offset.*

can be associated with the non-hydrogen bonded N-H vibrations, such as from H3 and H5. The broad features, reminiscent of the O-H peak shapes in other hydrogen-bonded crystals, e.g. solid H<sub>2</sub>O, correspond to the two groups of hydrogen-bonded NH<sub>2</sub>. With increasing pressure, as intermolecular distances are reduced and hydrogens are forced into closer vicinity of nitrogen atoms, these peaks broaden and fade. As these previously non-interacting atoms are forced into hydrogen bonding interactions, the signal for each is muddled until the point of transition. The changes in the Raman spectra accompanying the monoclinic-to-triclinic phase transition, observed in diffraction data at approximately 30 GPa in Ne and 38 GPa in He, are quite pronounced in all three spectral ranges, with the appearance of new spectral features often occurring slightly before the observed transition pressure. In the ring breathing mode range the high wave number component of the 750 cm<sup>-1</sup> peak splits into a doublet, as does the 1100 cm<sup>-1</sup> peak, shown in Fig. 5.14. This is indicative of a change in the interaction between inter-layer molecules, potentially between newly crystallographically and energetically inequivalent ring systems after the phase transition [261-263]. In the C-N vibration range a whole new family of

peaks appears before the point of transition between 1500 and 1600 relative  $\text{cm}^{-1}$ , with new peaks forming at approximately 1700 and 17900 rel  $\text{cm}^{-1}$  above approximately 30 GPa. This corroborates a change in the electronic state beginning at 26.86(5) GPa, culminating in a change in symmetry. Similarly, in the N-H range two new high wavenumber peaks appear between 3500 and 3600  $\text{cm}^{-1}$  at approximately 30 GPa, and strengthen with increasing pressure.

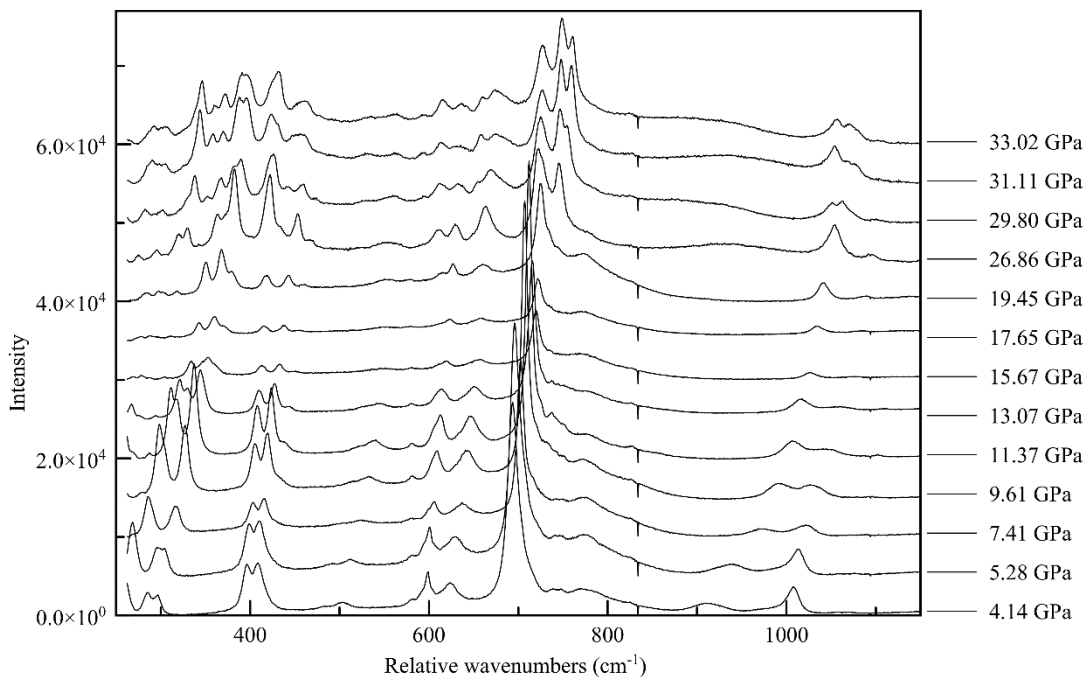


*Figure 5.14. Raman spectra of melamine in the ring vibration-mode range, vertical offset indicates pressure steps in GPa. Splitting of the 750  $\text{cm}^{-1}$  and 1100  $\text{cm}^{-1}$  peaks is observed at 29.80(5) GPa in Ne.*

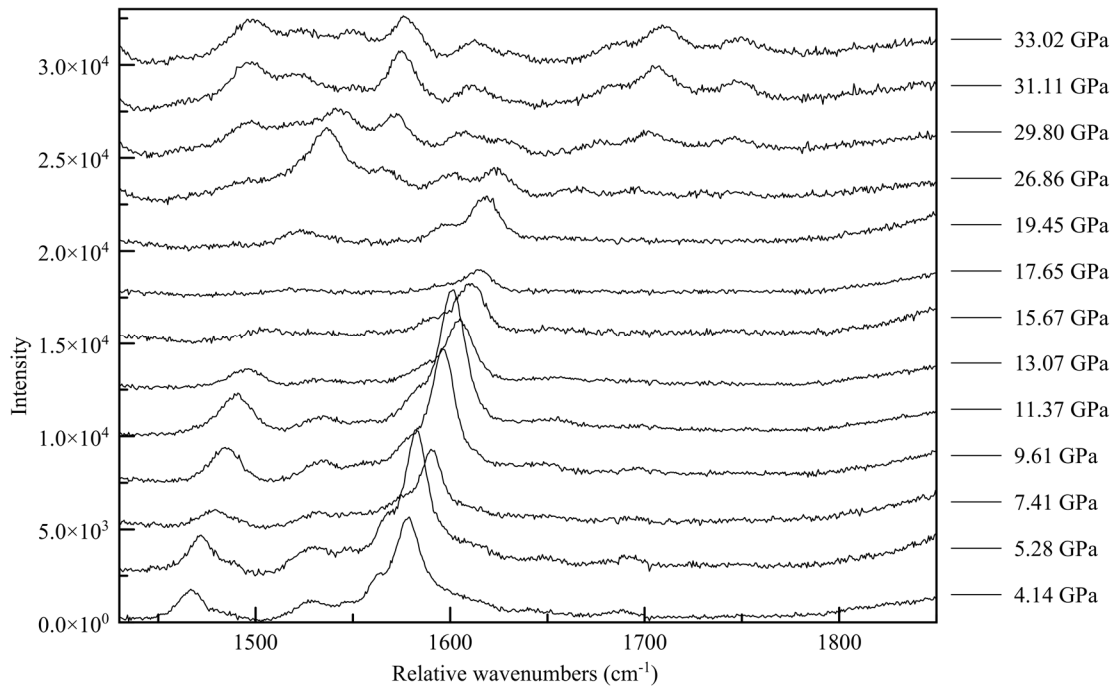


*Figure 5.15. Raman spectra of melamine in the C-N vibration mode range, vertical offset indicates pressure steps in GPa. Appearance of new peaks at approximately 1700 and 1790  $\text{cm}^{-1}$  are seen above approximately 30 GPa.*

## 5.4 DISCUSSION

The compressional behavior of melamine closely resembles that of other hydrogen-bonded molecular solids, where individual molecular subunits and internal covalent bonds are not significantly altered with pressure [15, 87, 88, 90, 264]. Instead, hydrogen bonds can readily accommodate the increase in pressure, becoming more stable with decreasing donor-acceptor distances and linearization of donor-hydrogen-acceptor angles up to a critical pressure [1, 265]. Melamine is notable for its extensive network of hydrogen bonds when compared to other substituted aromatics [15, 88], which allows it to remain structurally stable over the same pressure range where many other molecular crystals irreversibly amorphize or decompose [248]. Additionally, this increase in hydrogen bonding stability (and by extension, covalent character) seems to overrule or direct other steric and electronic interactions that would otherwise exhibit more control over compressional behavior and reactivity. This is especially apparent when comparing against non-hydrogen bonded molecular crystals; for instance, although *s*-triazine shares the same fundamental aromatic ring system as melamine, its behavior is controlled by  $\pi$  interactions, resulting in susceptibility to electronic modification with pressure and increased reactivity [95, 96, 265], ultimately becoming irreversibly amorphous at 15.2 GPa. Similarly, benzene amorphizes into extended polyaromatic compounds at 23 GPa. Crystallinity is also generally limited to lower pressure ranges in molecular solids with limited or weak hydrogen bonding character; pyrimidine amorphizes at 22.4 GPa [266], pyrrole at 14.3 GPa [267], and pyridine at 22 GPa [268]. Each of these amorphization transitions is irreversible, indicating significant changes in the covalent bonding environment, often through ring-opening and polymerization [266].

In molecular crystals with extended hydrogen bonding networks (often with “rosette-type” hydrogen bonding geometry) such as melamine and its related adducts, as well as TATB, the pressure-stability relationship appears to be more complex. In a 1:2 melamine-boric acid adduct, a reversible amorphization transition was reported at 18 GPa, indicating a loss of periodicity but not chemical alteration [269]. For a 1:1 cyanuric acid-melamine adduct, an irreversible phase transition at 4.9 GPa to a quenchable crystalline phase of lower symmetry was reported [270]. This was accompanied by a pronounced change in the crystal’s opacity, not

unlike what is seen in the irreversible amorphization of melamine. Surprisingly, TATB in hydrostatic helium was found to be stable up to at least 150 GPa, after experiencing several subtle, reversible phase transformations that produced visible color changes in the crystal [248].

In melamine, the phase transformations to the triclinic polymorph and amorphous phase occur at roughly double the pressure than other molecular solids, at upwards of 36 GPa in helium. The reversible transformation to the triclinic structure results from a rearrangement of the hydrogen bonding network in melamine, where electronic and electrostatic interactions not seen at ambient conditions are kept stable at high pressure but revert upon decompression. Upon further compression, the crystal can no longer accommodate these forced interactions, and an irreversible transition occurs to release the imposed stress on the structure. The large pressure stability field of melamine, combined with the interesting behavior of melamine adducts with pressure, indicate some potential for using melamine-based substituted triazines or adducts to design functional crystals held together by extensive pressure-stabilized hydrogen bonding networks.

**5.5. ACKNOWLEDGEMENTS:** The authors gratefully acknowledge the support of this study from the Carnegie-DOE Alliance Center under cooperative agreement DE FC52-08NA28554. Development of the GSE\_ADA software used for data analysis is supported by NSF grant EAR1440005. This project was performed at GeoSoilEnviroCARS (GSECARS Sector 13), and the High Pressure Collaborative Access Team (HPCAT Sector 16) of the Advanced Photon Source at Argonne National Laboratory. GeoSoilEnviroCARS is supported by the National Science Foundation - Earth Sciences (EAR-0622171) and Department of Energy - Geosciences (DE-FG02-94ER14466). HPCAT operations are supported by DOE-NNSA under Award No. DE-NA0001974 and DOE-BES under Award No. DE-FG02-99ER45775, with partial instrumentation funding by NSF. Use of the Advanced Photon Source was supported by the U. S. Department of Energy, Office of Science, Office of Basic Energy Sciences, under Contract No. DE-AC02-06CH11357. The authors declare no conflict of interest.

## CHAPTER 6: CONCLUSIONS AND FUTURE PROSPECTS

The presence of hydrogen and hydrogen bonding directly influences the material properties of a variety of geologically and technologically relevant compounds. In both instances, the behavior of hydrogen at high pressures has been of particular interest. Although hydrogen bonding holds large sway over the physio-chemical properties of a crystal (including phase transition behavior), quantifying this relationship has proven difficult. In geologically relevant materials, this manifests as an incomplete understanding of the action of water within the Earth's interior and the behavior of hydrated mineral phases at high pressures and temperatures. Past studies have focused on forcibly incorporating water into nominally anhydrous mineral crystal structures (such as bridgmanite,  $\text{MgSiO}_3$ ) or synthesizing their hydrous derivatives (the “3.65 Å” phase,  $\text{MgSi}(\text{OH})_6$ ) with idealized endmember compositions. However, these experiments are often technically challenging and sometimes produce contradictory results.

This dissertation approached the issue from another angle; rather than attempting to observe the effects of direct hydration on an otherwise anhydrous system, it made use of analogue materials to compare and contrast the high-pressure behavior of anhydrous and hydrous mineral species. For compounds with similar chemical formulas that are closely structurally related, this technique exploits chemical differences in order to extrapolate the behavior of the target system using an analogue that is more experimentally accessible. This has demonstrated success in other mineral systems, such as the use of  $\text{GeO}_2$  to study the high pressure behavior of  $\text{SiO}_2$  [63], where  $\text{GeO}_2$  displays very similar phase transition behavior as  $\text{SiO}_2$ , but at considerably lower pressures. This was the primary focus of Chapter 3, where the high pressure behavior of the mineral behoite ( $\text{Be}(\text{OH})_2$ ) was used as an analogue of  $\alpha$ -cristobalite ( $\text{SiO}_2$ ). The pressure-dependent transformation between  $\beta$  and  $\gamma$ -behoite was shown to be similar to that of  $\alpha$ -cristobalite's transition to cristobalite-II, where the rotation and collapse of tetrahedra induce phase transitions at similar pressures. However, behoite does not mirror the behavior of cristobalite at higher pressures; the addition of hydrogen bonding into the structure increases the rigidity between the corner-linked  $\text{BeO}_4$  tetrahedra, and the structure resists further pressure-induced distortion. Notably, behoite was not observed to experience a change in coordination below 30 GPa, whereas the tetrahedrally coordinated silicon in cristobalite-II transforms into an octahedrally coordinated polymorph known as cristobalite X-I at approximately 12.5 GPa. The

inter-tetrahedral hydrogen bonds appear to be responsible for the lack of higher-pressure polymorphism, which matches previously documented behavior of other hydrous mineral phases (such as  $\delta$ -AlOOH [32-34]). However, the influence of the beryllium cation must not be ruled out; although beryllium and silicon share very similar ionic radii, computational studies have predicted that beryllium oxide (BeO) remains tetrahedrally coordinated to at least 89.6 GPa, at which it forms an octahedrally-coordinated peroxide (BeO<sub>2</sub>) [271]. This highlights the need for further high pressure studies of Be(OH)<sub>2</sub> beyond 30 GPa, which would better correlate to mid and lower mantle conditions.

The tetrahedral to octahedral coordination change in cristobalite, the anhydrous counterpart to behoite, was investigated in Chapter 4, and the crystal structure of cristobalite X-I was determined and validated with both X-ray and DFT techniques. Relating cristobalite X-I to other high pressure octahedrally coordinated polymorphs of SiO<sub>2</sub> expands upon an increasingly complex family of metastable intermediate phases of silica. The behavior of the phase transition also demonstrates a complicated kinetic and thermodynamic landscape for SiO<sub>2</sub>; although an intermediate phase (cristobalite-II) is needed to form cristobalite X-I, it appears to directly transform back into  $\alpha$ -cristobalite during decompression. This back-transformation was observed at much lower pressures than those necessary to form the X-I phase, indicating non-equivalent kinetic and thermodynamic control over the pressurization and depressurization pathways, which corresponds with reported decompression hysteresis in other phases of SiO<sub>2</sub> [100, 174, 272].

Interestingly, the cristobalite X-I phase of SiO<sub>2</sub> could serve as an analogue structure to CO<sub>2</sub>. At very high pressures, CO<sub>2</sub> shares many structural similarities with SiO<sub>2</sub>, and several phases have identical structures [62, 171, 216]. The high pressure behavior of CO<sub>2</sub>, particularly changes in coordination, have been difficult to observe experimentally and are generally predicted at pressures over 900 GPa [60, 62]. Although these pressures do not occur within the Earth, they do occur within giant planets whose internal structures are largely unknown. Many of the computational efforts to discover the structure of high pressure phases of CO<sub>2</sub> produce metastable intermediates and complex path-dependent polymorphism; the structure of cristobalite X-I, along with other metastable silica phases, could serve as footholds for computationally exploring ultrahigh pressure CO<sub>2</sub> phases which may be common in planetary interiors.

Chapter 5, which explores the high pressure behavior of melamine, stands in contrast to Chapters 3 and 4. Rather than a silicate (or silicate analogue), melamine is an organic molecular crystal which does not form a clearly anhydrous or hydrous endmember species. Despite this, a similar strategy can be employed when comparing melamine to other related compounds, where pressure-dependent behavior is framed in the context of functional groups attached to the central triazine ring and their influence on polymorphism and reactivity. The validity of this strategy with molecular crystals has been previously demonstrated, where a central structural motif is held constant and functional groups are varied to determine how hydrogen bonds (as well as other intermolecular interactions) affect properties such as energetic reactivity or potential for directed polymerization [91]. As with hydrated mineral species, the presence of extensive hydrogen bonding networks has been shown to increase stability and resist pressure-induced polymorphism in a variety of organic crystal structures. More specifically, the extensive hydrogen bonding network in melamine results in an extended stability range when compared to *s*-triazine, which may be considered as a non-hydrogen bonded endmember [95, 96, 265]. With this in mind, the high-pressure behavior of melamine could be further utilized in two ways; first, to direct desired traits of melamine adducts, co-crystals, or related triazine species. Secondly, there is the opportunity to apply the same information to the geology of organic-rich planetary bodies such as Titan, where nitrogen-rich heterocycles like melamine are predicted to exist as derivatives of other simpler hydrocarbons and tholins [49, 83, 84]. Systematic exploration of related triazine derivatives using high-pressure experimental and computational techniques, similar to those previously performed for benzene derivatives, would be valuable in quantifying the effects of hydrogen bonding on aromatic nitrogen-rich heterocycles.

Finally, there are broader implications to the use of hydrogen-bonded analogue systems at high pressures. Recently, the use of high pressure has been suggested as a method to better understand thermal and photochemical polymorphism in both organic and inorganic coordination compounds [273]. In this way, pressure is used to probe the mechanical properties of a crystal, and to rank the energetic contributions of different intra- and intermolecular reactions. For instance, the rigidity along a direction in the crystal structure can often be correlated to the length and strength of the hydrogen bonds acting in that direction [16]; subsequently, the behavior of hydrogen bonds under hydrostatic pressure is proposed as a tool to examine the lattice strain

anisotropy of intermolecular interactions. Additionally, crystals that can be continuously compressed without exhibiting polymorphism are valued as benchmarking tools to validate and optimize computational models used to predict physio-chemical properties. The extended stability against pressurization seen in crystals with hydrogen bonding networks meets this criteria, further warranting the systematic evaluation of hydrogen-bonded crystal systems.

## **APPENDIX A: SUPPLEMENTAL MATERIAL TO CHAPTER 4**

### **A.1. Structure Model Comparison**

In crystallographic analysis, structure models are used to represent an approximation of physical reality that allows to produce the best match to experimental observations in x-ray diffraction experiments. The term “model” is used without any derogatory meaning, to simply emphasize that the real structures are likely more complex and non-ideal (e.g. due to defects).

In this paper, we presented a crystal structure model (X-IH) for the SiO<sub>2</sub> X-I phase, alternative to, and different from the X-IB model recently reported by [76]. Both models were derived from independent single crystal X-ray diffraction experiments. The two structures are described in the same space group, but are crystallographically distinct, describe different structural arrangements of zigzag chains of edge sharing octahedra, and different distributions of silicon atoms between available octahedral voids. In this section, we present a more detailed crystallographic analysis of these differences, aimed at assessing which of the two models is more general and better describes the ideal structure of cristobalite X-I. We also present results of four comparative crystallographic refinements in which both structure models were used with experimental data from each of the two studies.

#### **Comparative Structure Refinements**

The authors of [76] kindly provided a copy of their experimental X-ray diffraction peak intensity data (IB). For the purpose of thorough cross-comparison, we conducted four crystallographic refinements, in which models X-IH and X-IB were used with the intensity dataset obtained in our experiments (IH) and IB. Because the two intensity datasets were collected at quite different pressures, we used unit cell parameters specific to each data set. The experimental peak intensity dataset from IB contains more unique peaks (170 unique peaks with intensity higher than  $4\sigma$ , vs. 113 such peaks in data set IH), therefore we performed refinements with anisotropic atomic displacement parameters (ADPs) for Si atoms with IB intensity data and all isotropic ADPs with IH data sets. All refinements included optimization of an extinction parameter (which was used in [76], and seems to be necessary to achieve acceptable refinement convergence with the X-IB model). In all refinements, flexibility was allowed for redistribution of Si ions between the various

octahedral voids, with a restraint assuring that the overall content of the unit cell always remained  $\text{Si}_8\text{O}_{16}$ . Details of refinement statistics for each of these four cases are presented in Table S9.

### **Refinement 1: X-IB model with IB peak intensities**

This refinement was a simple reconstruction of results reported in [76], with treatment of data consistent with the remaining three refinements presented below. Because we used anisotropic ADPs for the Si atoms, and excluded two outlier peaks from the dataset, the figures of merit are slightly better than those reported in [76]. The refinement produced acceptable agreement of observed and calculated peak intensities. No significant electron density peaks or holes were found in the difference Fourier map. We note unusually high values (6.06) of the refined extinction parameter, which suggests that the data was slightly overcorrected during scaling. Refined occupancies of the three Si sites are 0.557, 0.955 and 0.975 for Si1, Si2 and Si3, respectively.

### **Refinement 2: X-IH model with IB peak intensities**

This refinement was a test whether the X-IH model is capable of explaining the experimental observations reported in [76]. Initial refinement with ideal  $4\text{-}60^\circ\text{-}2$  chains produced higher R-factors than refinement 1, and indicated the presence of residual electron density ( $1.2 \text{ e}/\text{\AA}^3$ ) in void V4, which corresponds to disorder related to the presence of  $4\text{-}60^\circ\text{-}2$  chains propagating in both 001 and 100 directions. After including this additional Si site, and optimizing distributions of Si between the three octahedral voids, refinement converged to Si site occupancies of 0.8308, 0.9525, and 0.2167, for Si01, Si02 and Si03, and R-factors comparable, but slightly better than for refinement 1. The value of the refined extinction parameter was also quite high (4.69), though lower than in refinement 1.

### **Refinement 3: X-IB model with IH peak intensities**

In these calculations we tested whether the X-IB model is capable of explaining our experimental observations. Similar to case 2, the initial refinement with only the original three Si ion locations yielded R-factors higher than 10%, and indicated the presence of residual electron density ( $2.0 \text{ e}/\text{\AA}^3$ ) at the X-IB second special position octahedral void, V5. After including this additional Si site, and optimizing the distribution of Si between the three octahedral voids, the refinement converged to Si site occupancies of 0.8095, 1.0441, 0.4535 and 0.1952, for Si1, Si2, Si3, and Si4, with acceptable R-factor statistics. We note that the refined SOF for Si2 was slightly

greater than 1 (unphysical, and suggesting that the model does not reflect the true Si ion distribution well) and extinction parameter was 1.18.

#### **Refinement 4: X-IH model (ideal) with IH peak intensities**

In this case, we report calculations with experimental peak intensity results and an ideal (no disorder, full occupancies of only two sites) 4-60°-2 chain structure model obtained in our structure solution. Refinement with these assumptions converges to R-factors comparable with refinement 3. Because of the simplicity and ideal nature (no disorder) of the model, and good quality of refinement statistics we consider this case an optimal explanation of the experimental observations. Small residual electron density ( $1.2 \text{ e}/\text{\AA}^3$ ) is observed at a center of octahedral void VX, but it is insufficiently high for refinement of disorder model. The refined extinction parameter is small (0.1119).

#### **Crystallographic conclusions**

Based on the four cases of crystallographic refinement discussed above we conclude that both models X-IB and X-IH can satisfactorily reproduce the experimental observations obtained from two independent in situ single crystal x-ray diffraction experiments. While this is true, we also established that the two models are crystallographically distinct and describe oxygen sublattices with sets of octahedral voids that differ in symmetry, thus implying different distributions of Si atoms. Crystallographic conventions require that the simplest, highest symmetry model is selected to describe the crystal structure, and it seems justified that a well-defined crystalline phase of a simple chemical compound, like SiO<sub>2</sub> should have an ideal simple and ordered crystal structure. Based on the above evidence, we believe that this structural arrangement is best described by the 4-60°-2 zigzag of the X-IH model. The ideal X-IH model conveniently lends itself to quantum mechanical simulations and allows for theoretical prediction of thermodynamic properties of cristobalite X-I which cannot be measured in x-ray diffraction experiments. The X-IB model is able to represent an approximation of the cristobalite X-I, configuration, but because of different octahedral void symmetry, requires a complex defect model. While defective crystals of cristobalite X-I definitely exist, and are probably very common, such non-ideal arrangement are best represented within the X-IH description.

## A.2. Supplemental Tables

Table A1. Unit cell parameters as a function of pressure from experimental methods. Entries marked with “\*” are adapted from [76].

<b>P (GPa)</b>	<b>a (Å)</b>	<b>b (Å)</b>	<b>c (Å)</b>	<b>β</b>	<b>V (Å<sup>3</sup>)</b>
3.6(1)	6.673(5)	4.153(4)	6.87(1)	97.9(2)	188.7(2)
4.8(1)	6.680(3)	4.142(2)	6.896(8)	98.10(6)	188.9(3)
7.9(1)	6.648(2)	4.123(1)	6.881(4)	98.10(3)	186.8(1)
10.7(1)	6.635(9)	4.103(7)	6.882(2)	98.21(2)	185.42(7)
10.8(2)*	6.66(1)	4.107(7)	6.894(1)	98.35(5)	186.7(3)
11.9(1)	6.623(2)	4.091(1)	6.866(3)	98.18(3)	184.2(1)
12.5(1)	6.616(1)	4.089(1)	6.876(3)	98.20(3)	184.1(1)
14(1)*	6.61(1)	4.070(1)	6.853(5)	94.10(1)	182.4(3)
17.9 (1)*	6.582(1)	4.044(1)	6.852(9)	98.13(4)	180.6(2)
23.0(3)*	6.580(1)	4.012(1)	6.80(1)	98.25(5)	177.77(3)
32.1(5)*	6.56(2)	3.965(1)	6.771(2)	98.16(8)	174.1(4)
47.9(1)*	6.446(9)	3.885(1)	6.670(1)	98.01(4)	165.4(2)
61.0(8)*	6.393(1)	3.837(1)	6.63(1)	98.05(5)	161.1(3)
69.7(6)*	6.400(3)	3.824(2)	6.527(4)	97.01(2)	158.5(7)

Table A2. Unit cell parameters as a function of pressure from DFT (vdW-optB88) methods.

<b>P (GPa)</b>	<b>a (Å)</b>	<b>b (Å)</b>	<b>c (Å)</b>	<b><math>\beta</math> (°)</b>	<b>V (Å<sup>3</sup>)</b>
0	6.756	4.197	7.030	98.1	198.152
5	6.722	4.156	6.995	98.1	194.152
10	6.692	4.120	6.962	98.1	190.52
15	6.664	4.086	6.931	98.1	187.232
20	6.638	4.055	6.903	98.1	184.168
25	6.614	4.025	6.875	98.1	181.352
30	6.591	3.997	6.849	98.1	178.768
35	6.569	3.972	6.824	98.1	176.296
40	6.549	3.948	6.801	98.1	21.750
45	6.529	3.925	6.778	98.0	21.483
50	6.510	3.903	6.756	98.0	21.228

Table A3. Definitions of symmetry operations.

Atom Number	Symmetry Operation
#1	$-x+3/2, y+1/2, -z+1/2$
#2	$x+1/2, -y-1/2, z-1/2$
#3	$-x++1, -y+, -z+$
#4	$-x+1/2, y+1/2, -z+1/2$
#5	$-x+1, -y+, -z+1$
#6	$-x+3/2, y-1/2, -z+1/2$
#7	$-x+1/2, y-1/2, -z+1/2$
#8	$x-1/2, -y-1/2, z+1/2$

Table A4. Calculated elastic properties at 10 GPa.

	$\alpha$ - cristobalite	-II	-X-IH	-X-IB	Post- quartz	Stishovite	Seifertite
<b>K<sub>V</sub> (GPa)</b>	66.339	76.695	289.935	289.960	332.167	332.278	338.875
<b>K<sub>R</sub> (GPa)</b>	65.667	62.504	277.440	277.467	329.246	324.443	337.636
<b>G<sub>V</sub> (GPa)</b>	89.880	136.016	444.871	443.283	506.497	450.904	508.625
<b>G<sub>R</sub> (GPa)</b>	38.867	51.708	199.385	199.367	237.129	206.049	236.843
<b>K<sub>VRH</sub> (GPa)</b>	66.003	69.599	283.687	283.713	330.707	328.361	338.255
<b>G<sub>VRH</sub> (GPa)</b>	64.374	93.862	322.128	321.325	371.813	328.476	372.734
<b>A<sup>U</sup></b>	6.573	8.379	6.201	6.162	5.689	5.966	5.741

K<sub>V</sub>: Bulk modulus Voigt average

K<sub>R</sub>: Bulk modulus Reuss average

G<sub>V</sub>: Shear modulus Voigt average

G<sub>R</sub>: Shear modulus Reuss average

K<sub>VRH</sub>: Bulk modulus Voigt-Reuss-Hill average

G<sub>VRH</sub>: Shear modulus Voigt-Reuss-Hill average

A<sup>U</sup>: Universal elastic anisotropy

Table A5. Calculated Debye frequency and Debye temperature at 10 GPa

	<b><math>\alpha</math>- cristobalite</b>	<b>II</b>	<b>X-IH</b>	<b>X-IB</b>	<b>Post- quartz</b>	<b>Stishovite</b>	<b>Seifertite</b>
<b><math>\omega_D</math> (THz)</b>	21.472	13.075	21.875	21.878	24.590	22.067	25.292
<b><math>\theta_D</math> (K)</b>	1030.5	627.5	1049.8	1049.8	1180.1	1059.0	1213.8
<b>Dynamically Stable?</b>	No	Yes	Yes	Yes	Yes	Yes	Yes

\* $\omega_D$ : Debye frequency in THz

\* $\theta_D$ : Debye temperature in K

\*Equation used to calculate Debye temperature from Debye frequency:

$$\theta_D = \frac{h\omega_D}{k}$$

Where  $h$  is the Planck's constant and  $k$  is the Boltzmann constant.

Table A6. Calculated Elastic Tensors at 10 GPa.

**$\alpha$ -Cristobalite**

$$C_{ij} = \begin{pmatrix} 542.09304 & 51.98099 & 126.52661 & 0.00000 & 0.00000 & 0.00000 \\ 51.98098 & 542.09312 & 126.52664 & 0.00000 & 0.00000 & 0.00000 \\ 126.55730 & 126.55736 & 446.10131 & 0.00000 & 0.00000 & 0.00000 \\ 0.00222 & 0.00317 & 0.00069 & 86.59478 & 0.00000 & 0.00000 \\ 0.02358 & 0.02623 & 0.02078 & -0.00026 & 174.01022 & -0.00005 \\ 0.02238 & 0.02628 & 0.02653 & 0.00023 & 0.00060 & 174.03571 \end{pmatrix}$$

$$S_{ij} = \begin{pmatrix} 0.00198 & -0.00006 & -0.00054 & 0.00000 & 0.00000 & 0.00000 \\ -0.00006 & 0.00198 & -0.00054 & 0.00000 & 0.00000 & 0.00000 \\ -0.00054 & -0.00054 & 0.00255 & 0.00000 & 0.00000 & 0.00000 \\ -0.00000 & -0.00000 & 0.00000 & 0.01155 & 0.00000 & 0.00000 \\ -0.00000 & -0.00000 & -0.00000 & 0.00000 & 0.00575 & 0.00000 \\ -0.00000 & -0.00000 & -0.00000 & -0.00000 & 0.00000 & 0.00575 \end{pmatrix}$$

**Post-quartz**

$$C_{ij} = \begin{pmatrix} 683.53032 & 193.94309 & 182.67991 & -0.00011 & -0.00006 & 35.80229 \\ 193.91313 & 626.25946 & 195.31316 & -0.00012 & -0.00015 & -6.42711 \\ 182.66454 & 195.33448 & 686.41117 & -0.00004 & -0.00012 & 17.68732 \\ -0.00235 & -0.00325 & -0.00354 & 306.06732 & -17.72981 & -0.00004 \\ -0.00240 & -0.00240 & -0.00241 & -17.73094 & 300.33172 & -0.00013 \\ 35.78921 & -6.44431 & 17.66327 & -0.00008 & 0.00002 & 245.14977 \end{pmatrix}$$

$$S_{ij} = \begin{pmatrix} 0.00168 & -0.00042 & -0.00032 & 0.00000 & 0.00000 & -0.00023 \\ -0.00042 & 0.00186 & -0.00042 & 0.00000 & 0.00000 & 0.00014 \\ -0.00032 & -0.00042 & 0.00166 & -0.00000 & 0.00000 & -0.00008 \\ 0.00000 & 0.00000 & 0.00000 & 0.00328 & 0.00019 & -0.00000 \\ 0.00000 & 0.00000 & 0.00000 & 0.00019 & 0.00334 & 0.00000 \\ -0.00023 & 0.00014 & -0.00008 & 0.00000 & -0.00000 & 0.00412 \end{pmatrix}$$

**Stishovite**

$$C_{ij} = \begin{pmatrix} 566.44503 & 213.79614 & 199.37885 & 0.00000 & 0.00000 & -0.00000 \\ 213.79616 & 566.44506 & 199.37887 & -0.00000 & -0.00000 & 0.00000 \\ 199.34917 & 199.34915 & 756.97953 & 0.00000 & 0.00000 & -0.00000 \\ -0.00306 & -0.00249 & -0.00132 & 339.82240 & -0.00000 & -0.00000 \\ -0.00227 & -0.00326 & -0.00294 & 0.00007 & 265.59933 & -0.00001 \\ -0.00487 & -0.00402 & -0.00507 & -0.00003 & 0.00002 & 265.59433 \end{pmatrix}$$

$$S_{ij} = \begin{pmatrix} 0.00216 & -0.00068 & -0.00039 & 0.00000 & 0.00000 & 0.00000 \\ -0.00068 & 0.00216 & -0.00039 & 0.00000 & 0.00000 & 0.00000 \\ -0.00039 & -0.00039 & 0.00153 & 0.00000 & 0.00000 & 0.00000 \\ 0.00000 & 0.00000 & -0.00000 & 0.00294 & 0.00000 & 0.00000 \\ 0.00000 & 0.00000 & 0.00000 & -0.00000 & 0.00377 & 0.00000 \\ 0.00000 & 0.00000 & 0.00000 & -0.00000 & -0.00000 & 0.00377 \end{pmatrix}$$

**Seifertite**

$$C_{ij} = \begin{pmatrix} 645.90792 & 198.66464 & 188.14030 & -0.00000 & -0.00000 & 0.00000 \\ 198.67826 & 641.50922 & 180.48298 & -0.00000 & -0.00000 & 0.00000 \\ 188.12322 & 180.46942 & 730.59477 & -0.00000 & -0.00000 & -0.00000 \\ -0.00792 & -0.00763 & -0.00799 & 314.57822 & 0.00000 & 0.00000 \\ -0.01880 & -0.01860 & -0.01969 & -0.00134 & 244.59844 & 0.00008 \\ -0.00249 & -0.00267 & -0.00162 & 0.00012 & 0.00025 & 293.57663 \end{pmatrix}$$

$$S_{ij} = \begin{pmatrix} 0.00179 & -0.00046 & -0.00035 & 0.00000 & 0.00000 & 0.00000 \\ -0.00046 & 0.00179 & -0.00033 & 0.00000 & 0.00000 & 0.00000 \\ -0.00035 & -0.00033 & 0.00154 & 0.00000 & 0.00000 & 0.00000 \\ 0.00000 & 0.00000 & 0.00000 & 0.00318 & 0.00000 & 0.00000 \\ 0.00000 & 0.00000 & 0.00000 & 0.00000 & 0.00409 & -0.00000 \\ 0.00000 & 0.00000 & 0.00000 & -0.00000 & -0.00000 & 0.00341 \end{pmatrix}$$

**Cristobalite-II**

$$C_{ij} = \begin{pmatrix} 488.64436 & 170.20404 & 86.49184 & -0.00000 & -0.00000 & 37.19425 \\ 170.21523 & 462.35758 & 131.16557 & -0.00000 & 0.00000 & 4.31134 \\ 86.49440 & 131.14745 & 508.30322 & -0.00000 & -0.00000 & -6.94163 \\ -0.00660 & -0.00647 & -0.00173 & 217.48125 & 8.45843 & 0.00093 \\ -0.00062 & -0.00038 & -0.00364 & 8.47310 & 171.95744 & 0.00013 \\ 37.18659 & 4.30663 & -6.94407 & -0.00018 & -0.00057 & 126.48912 \end{pmatrix}$$

$$S_{ij} = \begin{pmatrix} 0.00242 & -0.00083 & -0.00021 & -0.00000 & -0.00000 & -0.00070 \\ -0.00083 & 0.00262 & -0.00053 & 0.00000 & 0.00000 & 0.00012 \\ -0.00021 & -0.00053 & 0.00214 & 0.00000 & 0.00000 & 0.00020 \\ 0.00000 & 0.00000 & -0.00000 & 0.00461 & -0.00023 & -0.00000 \\ 0.00000 & -0.00000 & 0.00000 & -0.00023 & 0.00583 & -0.00000 \\ -0.00070 & 0.00012 & 0.00020 & 0.00000 & 0.00000 & 0.00812 \end{pmatrix}$$

**Cristobalite X-III**

$$C_{ij} = \begin{pmatrix} 622.30441 & 190.47785 & 181.59375 & -0.00000 & -0.00000 & 4.22067 \\ 190.53278 & 559.33211 & 172.07546 & 0.00000 & -0.00000 & 2.74518 \\ 181.60424 & 172.04229 & 705.60937 & 0.00000 & -0.00000 & -6.26951 \\ 0.00210 & 0.00142 & 0.00211 & 297.59850 & -0.61779 & -0.00009 \\ -0.00046 & -0.00003 & 0.00010 & -0.62363 & 263.03787 & -0.00010 \\ 4.21621 & 2.74606 & -6.26893 & 0.00023 & -0.00055 & 244.95253 \end{pmatrix}$$

$$S_{ij} = \begin{pmatrix} 0.00187 & -0.00053 & -0.00035 & 0.00000 & -0.00000 & -0.00004 \\ -0.00053 & 0.00208 & -0.00037 & 0.00000 & -0.00000 & -0.00002 \\ -0.00035 & -0.00037 & 0.00160 & -0.00000 & 0.00000 & 0.00005 \\ -0.00000 & -0.00000 & -0.00000 & 0.00336 & 0.00001 & 0.00000 \\ 0.00000 & -0.00000 & -0.00000 & 0.00001 & 0.00380 & 0.00000 \\ -0.00004 & -0.00002 & 0.00005 & -0.00000 & 0.00000 & 0.00408 \end{pmatrix}$$

**Cristobalite X-IB**

$$C_{ij} = \begin{pmatrix} 621.63710 & 190.00845 & 182.96738 & 0.00000 & -0.00000 & 0.59853 \\ 190.06130 & 559.32790 & 172.56220 & 0.00000 & -0.00000 & 4.00843 \\ 182.99614 & 172.54741 & 703.56062 & 0.00000 & -0.00000 & -8.44112 \\ 0.00166 & 0.00085 & 0.00165 & 297.50344 & 1.79685 & -0.00013 \\ -0.00140 & -0.00092 & -0.00079 & 1.79413 & 263.13216 & -0.00014 \\ 0.59655 & 4.01139 & -8.43402 & 0.00019 & -0.00042 & 246.33328 \end{pmatrix}$$

$$S_{ij} = \begin{pmatrix} 0.00188 & -0.00053 & -0.00036 & 0.00000 & -0.00000 & -0.00001 \\ -0.00053 & 0.00208 & -0.00037 & 0.00000 & -0.00000 & -0.00005 \\ -0.00036 & -0.00037 & 0.00161 & -0.00000 & 0.00000 & 0.00006 \\ -0.00000 & -0.00000 & -0.00000 & 0.00336 & -0.00002 & 0.00000 \\ 0.00000 & 0.00000 & 0.00000 & -0.00002 & 0.00380 & 0.00000 \\ -0.00001 & -0.00005 & 0.00006 & -0.00000 & 0.00000 & 0.00406 \end{pmatrix}$$

Table A7. Locations of octahedral voids in the X-IB model generated using the Endeavour program from the coordinates of 6 oxygen ligands surrounding each void.

Space group P 1 2<sub>1</sub>/n 1 (no. 14)

a = 6.5700(23) Å, b = 4.0633(6) Å, c = 6.8345(45) Å, β = 98.00(6)°, V=180.68(14) Å<sup>3</sup>

Atom	Wyck.		x	y	z
O2	4e		-0.20059	0.24044	0.53828
O3	4e		-0.04580	0.72682	0.70938
O4	4e		-0.16596	0.73861	0.32565
O5	4e		-0.08620	0.26147	-0.07924
V1	4e		0.37440	0.50153	0.62539
V2	4e	Si3	0.25000	0.50709	0.25000
V3	4e	Si2	-0.12560	0.49847	0.12539
V4	2d	Si1	0.50000	0.00000	0.00000
V5	2b		0.50000	0.50000	0.00000

Table A8. Locations of octahedral voids in the X-IH model generated using the Endeavour program from the coordinates of 6 oxygen ligands surrounding each void.

Space group P 1 2<sub>1</sub>/n 1 (no. 14)

a = 6.6129(1) Å, b = 4.1143(1) Å, c = 6.9124(1) Å, β = 98.33(1)°, V=186.08(1) Å<sup>3</sup>

Atom	Wyck.		x	y	z
O003	4e		0.47860	0.20435	0.10534
O004	4e		0.63961	-0.25269	0.27495
O005	4e		0.26349	-0.22715	0.15180
O006	4e		0.39385	-0.22781	0.51894
V1	4e	Si1	-0.18839	0.49160	0.43881
V2	4e		0.43637	0.49956	0.31338
V3	4e	Si2	0.43637	-0.00044	0.31338
V4	4e	Si3	0.18839	0.00840	0.56119

Table A9. Possible SiO<sub>2</sub> structures with full Si atom occupancies in the X-IB oxygen sublattice.

Octahedral voids occupied	Structure type
V1, V2	4 islands
V1, V3	isolated “stishovite” slabs
V2, V3	4 islands
V1, V4, V5	4 islands inverted honeycomb
V2, V4, V5	isolated “stishovite” slabs
V3, V4, V5	4 islands inverted honeycomb

Table A10. Possible SiO<sub>2</sub> structures with full Si atom occupancies in the X-IH oxygen sublattice.

Octahedral voids occupied	Structure type
V1, V2	4-60°-2 chains along (100)
V1, V3	4-60°-2 chains along (001)
V1, V4	isolated “seifertite” slabs
V2, V3,	isolated “seifertite” slabs
V2, V4,	4-60°-2 chains along (001)
V3, V4	4-60°-2 chains along (100)

Table A11. Comparison of results of the four comparative crystallographic refinements.

	Refinement 1	Refinement 2	Refinement 3	Refinement 4
Data/restraints/ parameters	207 / 1 / 45	207 / 1 / 48	113 / 1 / 32	113 / 0 / 26
Goodness-of-fit on F <sup>2</sup>	1.099	1.036	1.022	1.088
Final R indices				
R1 [I>2sigma(I)]	0.0798	0.0787	0.0841	0.0832
wR2 [I>2sigma(I)]	0.2174	0.1987	0.2552	0.2691
R1 (all data)	0.0889	0.0883	0.0841	0.0832
wR2 (all data)	0.2325	0.2086	0.2552	0.2691
Extinction coefficient	6.1(17)	4.7(11)	1.4(6)	0.12(17)
Largest diff. peak	0.417	0.427	1.189	1.217
Largest diff. hole	-0.452	-0.364	-0.994	-1.442

## APPENDIX B: SUPPLEMENTAL MATERIAL TO CHAPTER 5

### B.1. Supplemental Figures

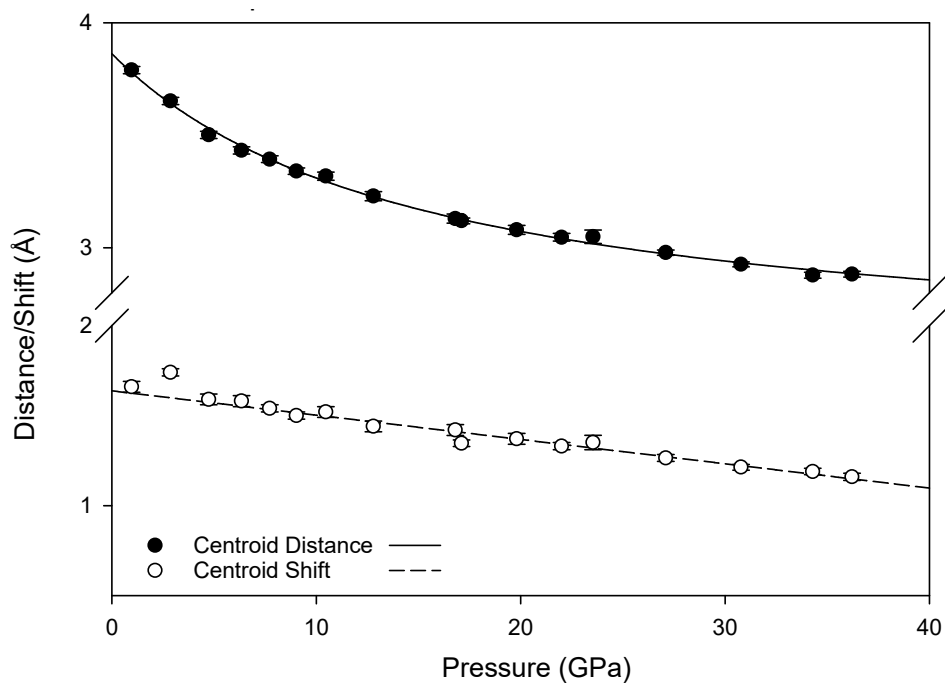


Figure B1. Ring centroid-centroid distance and shift as a function of pressure. Centroid distance is the straight line distance between the centers of the rings, shift indicates the in-plane separation between the centers of ring planes.

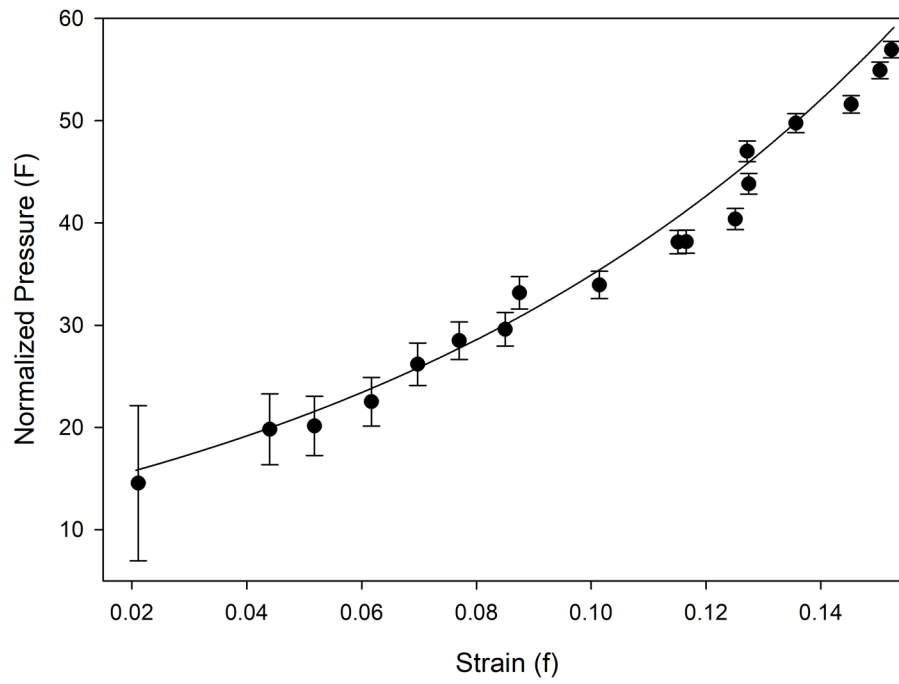


Figure B2:  $F$ - $f$  plot for data plotted with a third-order Vinet equation of state.

## B.2. Supplemental Tables

Table B1. Selected bond lengths and angles for melamine at 36.2(1) GPa (2015\_10). Amino C-N-H angles are set to 120° by the AFIX hydrogen bond command.

Bonded atoms	Length (Å)	Atoms in angle	Angle (°)
C(1)-N(1)	1.26(2)	N(1)-C(1)-N(6)	121.5(6)
C(1)-N(6)	1.345(17)	N(1)-C(1)-N(5)	118.1(12)
C(1)-N(5)	1.361(8)	N(6)-C(1)-N(5)	120.4(14)
C(2)-N(2)	1.302(14)	N(2)-C(2)-N(6)	120.1(6)
C(2)-N(6)	1.316(17)	N(2)-C(2)-N(4)	115.8(11)
C(2)-N(4)	1.345(8)	N(6)-C(2)-N(4)	124.1(10)
C(3)-N(5)	1.30(2)	N(5)-C(3)-N(4)	125.8(8)
C(3)-N(4)	1.317(15)	N(5)-C(3)-N(3)	117.3(10)
C(3)-N(3)	1.335(10)	N(4)-C(3)-N(3)	116.9(14)

Table B2. Atomic coordinates ( $\times 10^4$ ) and equivalent isotropic displacement parameters ( $\text{Å}^2 \times 10^3$ ) for carbon and nitrogen atoms melamine at 36.2(1) GPa (2015\_10).  $U_{\text{eq}}$  is defined as one third of the trace of the orthogonalized  $U_{ij}$  tensor.

Atom	x	y	z	$U_{\text{eq}}$
C(1)	1771(16)	6196(8)	290(40)	11(1)
C(2)	1307(16)	4725(7)	3230(40)	9(1)
C(3)	634(16)	7829(8)	2330(40)	11(1)
N(1)	2234(14)	6180(7)	1340(40)	10(1)
N(2)	1280(12)	3193(7)	4440(30)	7(1)
N(3)	252(13)	9514(7)	2970(30)	10(1)
N(4)	586(15)	6305(7)	3570(40)	11(1)
N(5)	1098(13)	7850(7)	610(30)	10(1)
N(6)	2005(14)	4661(7)	1780(40)	11(1)

Table B3. Definitions of symmetry operators.

Atom	Symmetry operators		
\$1	x,	y,	z-1
\$2	-x+1/2,	y-1/2,	-z
\$3	-x+1/2,	y+1/2,	-z
\$4	x,	y-1,	z
\$5	-x+1/2,	y-1/2,	-z+1
\$6	-x,	-y+1,	-z+1
\$7	x	y+1	z
\$8	-x	-y+2	-z
\$9	-x	-y+2	-z+1

Table B4: Hydrogen bond D-H-A lengths and angles at 36.2(1) GPa (2015\_10). Hydrogen bonds linking to neighboring triazine ring nitrogen atoms are displayed in bold.

D-H..A Symmetry	d(D-H)	d(H..A)	<DHA	d(D..A)
<b>N1-H1...N5_\$2</b>	0.935	1.792	155.72	2.672(8)
<b>N1-H2...N6_\$3</b>	0.935	1.821	134.85	2.568(7)
<b>N2-H3...N4_\$5</b>	0.865	2.16	126.5	2.763(12)
<b>N2-H3...N6_\$5</b>	0.865	2.688	117.55	3.182(16)
<b>N3-H6...N5_\$8</b>	0.886	1.89	139.51	2.628(18)
<b>N2-H4...N4_\$6</b>	0.865	1.703	161.53	2.538(13)
N1-H1...N2_\$1	0.935	2.481	120.73	3.067(18)
N1-H1...N3_\$2	0.935	2.379	134.58	3.108(10)
N1-H2...N2_\$3	0.935	2.477	127.01	3.131(14)
N2-H3...N1_\$2	0.865	2.49	131.52	3.131(14)
N2-H3...N3_\$4	0.865	2.152	122.47	2.717(10)
N2-H4...N3_\$6	0.865	2.561	129.4	3.182(12)
N3-H6...N1_\$3	0.886	2.546	121.95	3.108(10)
N3-H6...N2_\$7	0.886	2.158	120.4	2.717(10)
N3-H5...N2_\$6	0.886	2.565	127.35	3.182(12)
N3-H5...N3_\$9	0.886	1.96	159.3	2.81(3)

## REFERENCES

1. Gilli, G. and P. Gilli, *The nature of the hydrogen bond: outline of a comprehensive hydrogen bond theory*. IUCr monographs on crystallography. 2009, Oxford ; New York: Oxford University Press. xi, 317 p.
2. Grabowski, S., ed. *Hydrogen Bonding - New Insights*. Challenges and Advanced in Computational Chemistry and Physics. Vol. 3. 2006, Springer Netherlands.
3. Spektor, K., et al., *Ultrahydrous stishovite from high-pressure hydrothermal treatment of SiO<sub>2</sub>*. Proceedings of the National Academy of Sciences of the United States of America, 2011. **108**(52): p. 20918-20922.
4. Rozsa, V.F. and T.A. Strobel, *Triple Guest Occupancy and Negative Compressibility in Hydrogen-Loaded  $\beta$ -Hydroquinone Clathrate*. The Journal of Physical Chemistry Letters, 2014. **5**(11): p. 1880-1884.
5. Strobel, T.A., et al., *Hydrogen-Stuffed, Quartz-Like Water Ice*. Journal of the American Chemical Society, 2016. **138**(42): p. 13786-13789.
6. Hawthorne, F.C. and W.H. Baur, *Hydrogen Bonding in Minerals*, in *Advanced Mineralogy: Volume 1 Composition, Structure, and Properties of Mineral Matter: Concepts, Results, and Problems*, A.S. Marfunin, Editor. 1994, Springer Berlin Heidelberg: Berlin, Heidelberg. p. 340-347.
7. Efimchenko, V.S., et al., *Hydrogen Solubility in Cristobalite at High Pressure*. The Journal of Physical Chemistry A, 2014. **118**(44): p. 10268-10272.
8. Mitra, S., *Developments in Geochemistry*, in *High Pressure Geochemistry & Mineral Physics, 1st Edition: Basics for Planetology and Geo-Material Science*. 2004, Elsevier Science. p. 66-93, 840-847, 885-900.
9. Wang, L.-C. and Q.-Y. Zheng, *Hydrogen Bonding in Supramolecular Crystal Engineering*, in *Hydrogen Bonded Supramolecular Structures*, Z.-T. Li and L.-Z. Wu, Editors. 2015, Springer Berlin Heidelberg: Berlin, Heidelberg. p. 69-113.
10. Katrusiak, A. *Hydrogen-Bonded Crystals of Exceptional Dielectric Properties*. in *Engineering of Crystalline Materials Properties*. 2008. Dordrecht: Springer Netherlands.
11. Bell, D.R. and G.R. Rossman, *Water in Earth's Mantle: The Role of Nominally Anhydrous Minerals*. Science, 1992. **255**(5050): p. 1391-7.

12. Hu, Q., et al., *Dehydrogenation of goethite in Earth's deep lower mantle*. Proceedings of the National Academy of Sciences, 2017. **114**(7): p. 1498.
13. Thompson, E.C., A.J. Campbell, and Z. Liu, *In-situ infrared spectroscopic studies of hydroxyl in amphiboles at high pressure*, in *American Mineralogist*. 2016. p. 706.
14. Steiner, T., *The Hydrogen Bond in the Solid State*. Angewandte Chemie International Edition, 2002. **41**(1): p. 48-76.
15. Fanetti, S., et al., *The role of H-bond in the high-pressure chemistry of model molecules*. J Phys Condens Matter, 2018. **30**(9): p. 094001.
16. Boldyreva, E.V., *High-pressure studies of the hydrogen bond networks in molecular crystals*. Journal of Molecular Structure, 2004. **700**(1): p. 151-155.
17. Ohtani, E. and K.D. Litasov, *The Effect of Water on Mantle Phase Transitions*. Reviews in Mineralogy and Geochemistry, 2006. **62**(1): p. 397-420.
18. Jackson, C.R.M., et al., *Noble gas transport into the mantle facilitated by high solubility in amphibole*. Nature Geosci, 2013. **6**(7): p. 562-565.
19. Inoue, T., et al., *Decomposition of K-amphibole at high pressures and implications for subduction zone volcanism*. Physics of the Earth and Planetary Interiors, 1998. **107**(1-3): p. 221-231.
20. Kim, Y., R.W. Clayton, and J.M. Jackson, *Distribution of hydrous minerals in the subduction system beneath Mexico*. Earth and Planetary Science Letters, 2012. **341-344**: p. 58-67.
21. Shieh, S.R., et al., *Decomposition of phase D in the lower mantle and the fate of dense hydrous silicates in subducting slabs*. Earth and Planetary Science Letters, 1998. **159**(1-2): p. 13-23.
22. Ohtani, E., et al., *Stability of Hydrous Minerals and Water Reservoirs in the Deep Earth Interior*. Deep Earth, 2016.
23. Jacobsen, S.D., *Effect of Water on the Equation of State of Nominally Anhydrous Minerals.*, in *Reviews in Mineralogy & Geochemistry*. 2006, Mineralogical Society of America. p. 321-342.
24. Jacobsen, S.D., et al., *Effects of hydration on the elastic properties of olivine*. Geophysical Research Letters, 2008. **35**(14): p. 1-6.

25. Yoshino, T., A. Shimojuku, and D. Li, *Electrical conductivity of stishovite as a function of water content*. *Physics of the Earth and Planetary Interiors*, 2013. **227**(0): p. 48-54.
26. Lakshtanov, D.L., et al., *The post-stishovite phase transition in hydrous alumina-bearing SiO<sub>2</sub> in the lower mantle of the earth*. *Proceedings of the National Academy of Sciences*, 2007. **104**(34): p. 13588-13590.
27. Khisina, N.R. and R. Wirth, *Nano-inclusions of high-pressure hydrous silicate, Mg<sub>3</sub>Si<sub>4</sub>O<sub>10</sub>(OH)<sub>2</sub> · nH<sub>2</sub>O (10Å-phase), in mantle olivine: Mechanisms of formation and transformation*. *Geochemistry International*, 2008. **46**(4): p. 319-327.
28. Wicks, J.K. and T.S. Duffy, *Crystal Structures of Minerals in the Lower Mantle*, in *Deep Earth: Physics and Chemistry of the Lower Mantle and Core, 1*. 2016, John Wiley & Sons, Inc. p. 69-87.
29. Hushur, A., et al., *Hydrogen bond symmetrization and equation of state of phase D*. *Journal of Geophysical Research: Solid Earth*, 2011. **116**(B6).
30. Tsuchiya, J., T. Tsuchiya, and S. Tsuneyuki, *First-principles study of hydrogen bond symmetrization of phase D under high pressure*. *American Mineralogist*, 2005. **90**(1): p. 44-49.
31. Tsuchiya, J. and M. Mookherjee, *Crystal structure, equation of state, and elasticity of phase H (MgSiO<sub>4</sub>H<sub>2</sub>) at Earth's lower mantle pressures*. *Scientific Reports*, 2015. **5**: p. 15534.
32. Panero, W.R. and L.P. Stixrude, *Hydrogen incorporation in stishovite at high pressure and symmetric hydrogen bonding in δ-AlOOH*. *Earth and Planetary Science Letters*, 2004. **221**(1): p. 421-431.
33. Sano-Furukawa, A., et al., *Change in compressibility of δ-AlOOH and δ-AlOOD at high pressure: A study of isotope effect and hydrogen-bond symmetrization*. *American Mineralogist*, 2009. **94**(8-9): p. 1255-1261.
34. Mashino, I., M. Murakami, and E. Ohtani, *Sound velocities of δ-AlOOH up to core-mantle boundary pressures with implications for the seismic anomalies in the deep mantle*. *Journal of Geophysical Research: Solid Earth*, 2016. **121**(2): p. 595-609.
35. Mao, H.-K., et al., *When water meets iron at Earth's core-mantle boundary*. *National Science Review*, 2017. **4**(6): p. 870-878.

36. Geng, H.Y., *Public debate on metallic hydrogen to boost high pressure research*. Matter and Radiation at Extremes, 2017. **2**(6): p. 275-277.
37. Isaac, F.S. and D. Ranga, *Metallic hydrogen*. Journal of Physics: Condensed Matter, 2018. **30**(25): p. 254003.
38. Aarestad, B., et al., *The ice VII-ice X phase transition with implications for planetary interiors.*, in *American Geophysical Union, Fall Meeting 2008*. 2008, AGU.
39. Goncharov, A.F., et al., *Dissociative melting of ice VII at high pressure*. The Journal of Chemical Physics, 2009. **130**(12): p. 124514.
40. Goncharov, A.F., et al., *Compression of ice to 210 gigapascals: Infrared evidence for a symmetric hydrogen-bonded phase*. Science, 1996. **273**: p. 218-220.
41. Kohen, A. and H. Limbach, *Isotope Effects on Hydrogen-Bond Symmetrization in Ice and Strong Acids at High Pressure.*, in *Isotope Effects in Chemistry and Biology*. 2005, CRC Press. p. 175-190.
42. Marques, M., G.J. Acklands, and J.S. Loveday, *Nature and stability of ice X*. High Pressure Research, 2009. **29**(2): p. 208-211.
43. Datchi, F., et al., *Solid ammonia at high pressure: A single-crystal x-ray diffraction study to 123 GPa*. Physical Review B, 2006. **73**(17): p. 174111.
44. Ninet, S. and F. Datchi, *High pressure–high temperature phase diagram of ammonia*. The Journal of Chemical Physics, 2008. **128**(15): p. 154508.
45. Meier, T., et al., *Observation of nuclear quantum effects and hydrogen bond symmetrisation in high pressure ice*. Nature Communications, 2018. **9**(1): p. 2766.
46. Vance, S.D., et al., *Geophysical Investigations of Habitability in Ice-Covered Ocean Worlds*. Journal of Geophysical Research: Planets, 2017. **123**(1): p. 180-205.
47. Grundy, W.M., et al., *Surface compositions across Pluto and Charon*. Science, 2016. **351**(6279).
48. Sohl, F., et al., *Structural and tidal models of Titan and inferences on cryovolcanism*. Journal of Geophysical Research: Planets, 2014. **119**(5): p. 1013-1036.
49. Maynard-Casely, H.E., et al., *Prospects for mineralogy on Titan*. American Mineralogist, 2018. **103**(3): p. 343-349.

50. Vu, T.H., et al., *Formation of a New Benzene–Ethane Co-Crystalline Structure Under Cryogenic Conditions*. The Journal of Physical Chemistry A, 2014. **118**(23): p. 4087-4094.
51. Maynard-Casely, H.E., et al., *A co-crystal between benzene and ethane: a potential evaporite material for Saturn's moon Titan*. IUCrJ, 2016. **3**(3): p. 192-199.
52. Heintz, A. and E. Bich, *The Atmosphere and Internal Structure of Saturn's Moon Titan, a Thermodynamic Study*, in *Thermodynamics*, M. Tadashi, Editor. 2011.
53. Faccenda, M., *Water in the slab: A trilogy*. Tectonophysics, 2014. **614**: p. 1-30.
54. Lawrence, J.F. and M.E. Wysession, *Seismic Evidence for Subduction-Transported Water in the Lower Mantle*. Earth's Deep Water Cycle, 2013.
55. Murakami, M., et al., *Post-Perovskite Phase Transition in MgSiO<sub>3</sub>*. Science, 2004. **304**(5672): p. 855.
56. Redfern, S.A.T., *Using Mineral Analogs to Understand the Deep Earth*. Deep Earth, 2016.
57. Stan, C.V., et al., *High-Pressure Study of Perovskites and Postperovskites in the (Mg,Fe)GeO<sub>3</sub> System*. Inorganic Chemistry, 2017. **56**(14): p. 8026-8035.
58. Bernal, F.L., et al., *Perovskite to Postperovskite Transition in NaFeF<sub>3</sub>*. Inorganic Chemistry, 2014. **53**(22): p. 12205-12214.
59. Ballaran, T.B., R.G. Tronnes, and D.J. Frost, *Equations of state of CaIrO<sub>3</sub> perovskite and post-perovskite phases*. American Mineralogist, 2007. **92**(10): p. 1760-1763.
60. Lu, C., M. Miao, and Y. Ma, *Structural Evolution of Carbon Dioxide under High Pressure*. Journal of the American Chemical Society, 2013. **135**(38): p. 14167-14171.
61. Sun, J., et al., *High-Pressure Polymeric Phases of Carbon Dioxide*. Proceedings of the National Academy of Sciences, 2009. **106**(15): p. 6077-6081.
62. Sengupta, A. and C.-S. Yoo, *Coesite-like CO<sub>2</sub>: An Analog to SiO<sub>2</sub>*. Physical Review B, 2010. **82**(1): p. 012105.
63. Prakapenka, V.P., et al., *High Pressure Induced Phase Transformation of SiO<sub>2</sub> and GeO<sub>2</sub>: Difference and Similarity*. Journal of Physics and Chemistry of Solids, 2004. **65**: p. 1537-1545.

64. Shannon, R., *Revised Effective Ionic Radii and Systematic Studies of Interatomic Distances in Halides and Chalcogenides*. Acta Crystallographica Section A, 1976. **32**(5): p. 751-767.
65. Murakami, M., et al., *Stability of CaCl<sub>2</sub>-type and  $\alpha$ -PbO<sub>2</sub>-type SiO<sub>2</sub> at high pressure and temperature determined by in-situ X-ray measurements*. Geophysical Research Letters, 2003. **30**(5).
66. Lakshtanov, D.L., et al., *The Post-Stishovite Phase Transition in Hydrated Alumina-Bearing SiO<sub>2</sub> in the Lower Mantle of the Earth*. Proceedings of the National Academy of Sciences, 2007. **104**(34): p. 13588-13590.
67. Nishi, M., et al., *Stability of hydrous silicate at high pressures and water transport to the deep lower mantle*. Nature Geoscience, 2014. **7**: p. 224.
68. Umemoto, K., et al., *Post-stishovite transition in hydrated aluminous SiO<sub>2</sub>*. Physics of the Earth and Planetary Interiors, 2016. **255**: p. 18-26.
69. Mitchell, R.H., M.D. Welch, and A.R. Chakhmouradian, *Nomenclature of the perovskite supergroup: A hierarchical system of classification based on crystal structure and composition*. Mineralogical Magazine, 2017. **81**(3): p. 411-461.
70. Lafuente, B., H. Yang, and R.T. Downs, *Crystal structure of tetrawickmanite, Mn<sup>2+</sup>Sn<sup>4+</sup>(OH)<sub>6</sub>*. Acta Crystallographica Section E, 2015. **71**(2): p. 234-237.
71. Kleppe, A.K., et al., *Phase transitions in hydroxide perovskites: a Raman spectroscopic study of stottite, FeGe(OH)<sub>6</sub>, to 21 GPa*. Mineralogical Magazine, 2018. **76**(4): p. 949-962.
72. Welch, M.D. and B. Wunder, *A single-crystal X-ray diffraction study of the 3.65 Å-phase MgSi(OH)<sub>6</sub>, a high-pressure hydroxide perovskite*. Physics and Chemistry of Minerals, 2012. **39**(9): p. 693-697.
73. Welch, M., *High-pressure behaviour of perovskite-related hydroxides: stottite FeGe(OH)<sub>6</sub> to 21 GPa*. Vol. 76. 2012. 946-962.
74. Palmer, D.C., et al., *The High Pressure Behavior of Cristobalite*. International Union of Crystallography, High-Pressure Group Meeting, 1992.
75. Dera, P., et al., *New Insights Into the High-Pressure Polymorphism of SiO<sub>2</sub> Cristobalite*. Physics and Chemistry of Minerals, 2011. **38**(7): p. 517-529.

76. Černok, A., et al., *Compressional pathways of  $\alpha$ -cristobalite, structure of cristobalite X-I, and towards the understanding of seifertite formation*. Nature Communications, 2017. **8**: p. 15647.
77. Koike, C., et al., *Infrared Spectra of Silica Polymorphs and the Conditions of Their Formation*. The Astrophysical Journal, 2013. **778**(1): p. 60.
78. Bridgman, P.W., *Recent Work in the Field of High Pressures*. Reviews of Modern Physics, 1946. **18**(1): p. 1-93.
79. Boldyreva, E., *High-pressure diffraction studies of molecular organic solids. A personal view*. Acta Crystallographica Section A, 2008. **64**(1): p. 218-231.
80. Katrusiak, A., *High-pressure X-ray diffraction studies of organic crystals*. High Pressure Research, 1990. **4**(1-6): p. 496-498.
81. Katrusiak, A. *General Description of Hydrogen-Bonded Solids at Varied Pressures and Temperatures*. in *High-Pressure Crystallography*. 2004. Dordrecht: Springer Netherlands.
82. Casati, N. *High-Pressure Structural Evolution of Molecular Crystals*. in *High-Pressure Crystallography*. 2010. Dordrecht: Springer Netherlands.
83. Cable, M.L., et al., *Titan Tholins: Simulating Titan Organic Chemistry in the Cassini-Huygens Era*. Chemical Reviews, 2012. **112**(3): p. 1882-1909.
84. Derenne, S., et al., *New insights into the structure and chemistry of Titan's tholins via  $^{13}\text{C}$  and  $^{15}\text{N}$  solid state nuclear magnetic resonance spectroscopy*. Icarus, 2012. **221**(2): p. 844-853.
85. Ciabini, L., et al., *High-pressure and high-temperature equation of state and phase diagram of solid benzene*. Phys Rev B, 2005. **72**: p. 094108.
86. Wen, X.D., R. Hoffmann, and N.W. Ashcroft, *Benzene under High Pressure: a Story of Molecular Crystals Transforming to Saturated Networks, with a Possible Intermediate Metallic Phase*. J. Am. Chem. Soc., 2011. **133**: p. 9023-9035.
87. Nobrega, M.M., M.L.A. Temperini, and R. Bini, *Probing the Chemical Stability of Aniline under High Pressure*. The Journal of Physical Chemistry C, 2017. **121**(13): p. 7495-7501.

88. Shishkina, S.V., et al., *Acceptor properties of amino groups in aminobenzene crystals: study from the energetic viewpoint*. CrystEngComm, 2017. **19**(42): p. 6274-6288.
89. Citroni, M., et al., *Role of excited electronic states in the high-pressure amorphization of benzene*. Proceedings of the National Academy of Sciences, 2008. **105**(22): p. 7658-7663.
90. Funnell, N.P., et al., *Destabilisation of hydrogen bonding and the phase stability of aniline at high pressure*. CrystEngComm, 2013. **15**(6): p. 1047-1060.
91. Manner, V.W., et al., *Examining the chemical and structural properties that influence the sensitivity of energetic nitrate esters*. Chemical science, 2018. **9**(15): p. 3649-3663.
92. Liu, G., et al., *Polymorphism of Energetic Materials: A Comprehensive Study of Molecular Conformers, Crystal Packing, and the Dominance of Their Energetics in Governing the Most Stable Polymorph*. Crystal Growth & Design, 2018. **18**(7): p. 4174-4186.
93. Zhang, C., X. Wang, and H. Huang,  *$\pi$ -Stacked Interactions in Explosive Crystals: Buffers against External Mechanical Stimuli*. Journal of the American Chemical Society, 2008. **130**(26): p. 8359-8365.
94. Guo, F., et al., *Effects of hydrogen bonds on solid state TATB, RDX, and DATB under high pressures*. Chinese Physics B, 2014. **23**(4): p. 046501.
95. Citroni, M., S. Fanetti, and R. Bini, *Pressure and Laser-Induced Reactivity in Crystalline s-Triazine*. The Journal of Physical Chemistry C, 2014. **118**(19): p. 10284-10290.
96. Fanetti, S., M. Citroni, and R. Bini, *Tuning the Aromaticity of s-Triazine in the Crystal Phase by Pressure*. The Journal of Physical Chemistry C, 2014. **118**(25): p. 13764-13768.
97. Bassett, W.A., *Diamond anvil cell, 50th birthday*. High Pressure Research, 2009. **29**(2): p. 163-186.
98. Mao, H.-K., et al., *Solids, liquids, and gases under high pressure*. Reviews of Modern Physics, 2018. **90**(1): p. 015007.
99. Millar, D.I.A., *Energetic materials at extreme conditions*. Springer Theses. 2012, Berlin ; Heidelberg: Springer-Verlag Berlin Heidelberg.

100. Černok, A., *Diversity of Compressional Mechanisms Among SiO<sub>2</sub> Polymorphs: Case of Coesite and Cristobalite*, in *Bayreuther Graduiertenschule für Mathematik und Naturwissenschaften*. 2015, University of Bayreuth: Bayreuth,. p. XVII, 121.
101. Mao, H.K., J. Xu, and P.M. Bell, *Calibration of the Ruby Pressure Gauge to 800 kbar Under Quasi-Hydrostatic Conditions*. *Journal of Geophysical Research: Solid Earth*, 1986. **91**: p. 4673-4676.
102. Dewaele, A., et al., *Compression curves of transition metals in the Mbar range: Experiments and projector augmented-wave calculations*. *Physical Review B*, 2008. **78**(10): p. 104102.
103. Syassen, K., *Ruby under pressure*. *High Pressure Research*, 2008. **28**(2): p. 75-126.
104. Blake, A.J. and W. Clegg, *Crystal structure analysis : principles and practice*. 2009, Oxford; New York: Oxford University Press.
105. Putz, H., J.C. Schon, and M. Jansen, *Combined method for ab initio structure solution from powder diffraction data*. *Journal of Applied Crystallography*, 1999. **32**(5): p. 864-870.
106. Sheldrick, G.M., *Crystal structure refinement with SHELXL*. *Acta Crystallogr C Struct Chem*, 2015. **71**(Pt 1): p. 3-8.
107. Schmidtman, M., *Hydrogen transfer in hydrogen bonded solid state materials*. 2008, University of Glasgow.
108. Watkin, D., *Structure refinement: some background theory and practical strategies*. *Journal of Applied Crystallography*, 2008. **41**(3): p. 491-522.
109. Massa, W., *Crystal structure determination*. 2nd completely updated ed. 2004, Berlin ; New York: Springer. xi, 210 p.
110. Glusker, J.P. and K.N. Trueblood, *Crystal structure analysis: a primer*. 2nd ed. 1985, New York: Oxford University Press. xvii, 269 p.
111. Katrusiak, A., *High-pressure crystallography*. *Acta Crystallographica Section A*, 2008. **64**(1): p. 135-148.
112. McMahan, M.I., *High-pressure crystallography*. *Top Curr Chem*, 2012. **315**: p. 69-109.
113. Boehler, R. and K. De Hantsetters, *New Anvil Designs in Diamond-Cells*. *High Pressure Research*, 2004. **24**(3): p. 391-396.

114. Kantor, I., et al., *BX90: A New Diamond Anvil Cell Design for X-ray Diffraction and Optical Measurements*. Review of Scientific Instruments, 2012. **83**(12): p. 125102.
115. Giustino, F., *Materials modelling using density functional theory: properties and predictions*. 1st ed. 2014, Oxford: Oxford University Press. xiv, 286 pages.
116. Hasnip, P.J., et al., *Density functional theory in the solid state*. Philosophical transactions. Series A, Mathematical, physical, and engineering sciences, 2014. **372**(2011): p. 20130270-20130270.
117. Tse, J.S. *Computational High Pressure Science*. in *High-Pressure Crystallography*. 2004. Dordrecht: Springer Netherlands.
118. Winkler, B. *Introduction to High Pressure Computational Crystallography*. in *High-Pressure Crystallography*. 2004. Dordrecht: Springer Netherlands.
119. Klimeš, J., D.R. Bowler, and A. Michaelides, *Van der Waals Density Functionals Applied to Solids*. Physical Review B, 2011. **83**(19): p. 195131.
120. Dion, M., et al., *Van der Waals Density Functional for General Geometries*. Physical Review Letters, 2004. **92**(24): p. 246401.
121. Blöchl, P.E., J. Kästner, and C.J. Först, *Electronic Structure Methods: Augmented Waves, Pseudopotentials and The Projector Augmented Wave Method*, in *Handbook of Materials Modeling: Methods*, S. Yip, Editor. 2005, Springer Netherlands: Dordrecht. p. 93-119.
122. Blöchl, P.E., *Projector Augmented-Wave Method*. Physical Review B, 1994. **50**(24): p. 17953-17979.
123. Togo, A. and I. Tanaka, *First Principles Phonon Calculations in Materials Science*. Scripta Materialia, 2015. **108**: p. 1-5.
124. Vandenabeele, P., *Practical Raman spectroscopy: an introduction*. 2013, The Atrium, Southern Gate, Chichester, West Sussex, United Kingdom: Wiley. xxii, 161 pages.
125. Smith, E. and G. Dent, *Modern Raman spectroscopy: a practical approach*. 2005, Hoboken, NJ: J. Wiley. x, 210 p.
126. Liu, Z., et al., *Synchrotron infrared spectroscopy of OH-chondrodite and OH-clinohumite at high pressure*. American Mineralogist, 2003. **88**: p. 1412-1415.
127. Friedrich, A., M. Kunz, and R. Miletich, *High-pressure behavior of Ba(OH)<sub>2</sub>: Phase transitions and bulk modulus*. Physical Review B, 2002. **66**(214103): p. 1-8.

128. Lin, J., et al., *Melting behavior of H<sub>2</sub>O at high pressures and temperatures*. Geophys. Res. Lett, 2005. **32**(11).
129. Haines, J., et al., *Crystalline Post-Quartz Phase in Silica at High Pressure*. Physical Review Letters, 2001. **87**(15): p. 155503-1 - 155503-4.
130. Haines, J. and O. Cambon, *The effects of pressure, temperature, and composition on the crystal structures of  $\alpha$ -quartz homeotypes*. Zeitschrift für Kristallographie, 2004. **219**: p. 314-323.
131. Koch-Müller, M., et al., *OH<sup>-</sup> in synthetic and natural coesite*. American Mineralogist, 2003. **88**(10): p. 1436-1445.
132. Zhang, G.-Q., et al., *Effect of Si-OH on the transformation of amorphous SiO<sub>2</sub> to coesite*. Journal of Alloys and Compounds, 2009. **476**(1-2): p. L4-L7.
133. Lathe, C., et al., *The influence of OH in coesite on the kinetics of the coesite-quartz phase transition*. American Mineralogist, 2005. **90**(1): p. 36-43.
134. Kusaba, K. and T. Kikegawa, *Phase transitions of Zn(OH)<sub>2</sub> under high pressure and high temperature*. Solid State Communications, 2008. **148**: p. 382-385.
135. Miletich, R., *High-pressure polymorphism, phase transition and elastic behaviour of behoite, Be(OH)<sub>2</sub>*, in *19th General Meeting of the International Mineralogical Association*. 2006: Kobe, Japan.
136. Lutz, H.D., et al., *Hydrogen bonding in solid hydroxides with strongly polarizing metal ions,  $\beta$ -Be(OH)<sub>2</sub> and  $\epsilon$ -Zn(OH)<sub>2</sub>*. Spectrochimica Acta Part A, 1998. **54**: p. 893-901.
137. Stahl, R., et al., *Kristallstrukturen und Wasserstoffbrueckenbindungen bei  $\beta$ -Be(OH)<sub>2</sub> und  $\epsilon$ -Zn(OH)<sub>2</sub>*. Z. Anorg. Chem., 1998. **624**: p. 1130-1136.
138. Brown, P.L. and C. Ekberg, *Alkaline Earth Metals: Beryllium*, in *Hydrolysis of Metal Ions*. 2016, Wiley-VCH: Weinheim, Germany.
139. Bear, I.J. and A.G. Turnbull, *Heats of formation of beryllium compounds*. Journal of Physical Chemistry, 1965. **69**: p. 2828-2833.
140. Nadezhina, T.N., et al., *Crystal structure of a new natural form of Be(OH)<sub>2</sub>*. Doklady Akademii Nauk SSSR, 1989. **305**: p. 95-98.
141. Pletnev, R.N., et al., *Proton magnetic resonance and the state of hydrogen in beryllium hydroxide*. Refractories and Industrial Ceramics, 2005. **46**(4): p. 273-275.

142. Sheldrick, G.M., *A Short History of SHELX*. Acta Crystallographica, 2008. **A64**: p. 112-122.
143. Downs, R.T. and M. Hall-Wallace, *XtalDraw*. American Mineralogist, 2003. **88**: p. 247-250.
144. Angel, R.J., et al., *Effective hydrostatic limits of pressure media for high-pressure crystallographic studies*. Journal of Applied Crystallography, 2007. **40**(1): p. 26-32.
145. Dera, P., *GSE\_ADA data analysis program for monochromatic single crystal diffraction with area detector*. 2007, GSECARS: Chicago, IL.
146. Dera, P., et al., *High Pressure Single-Crystal Micro X-ray Diffraction Analysis with GSE\_ADA/RSV Software*. High Pressure Research, 2013. **33**(3): p. 466-484.
147. Brandenburg, K. and H. Putz, *Endeavour*. 2009, Crystal Impact GbR: Bonn.
148. Dolomanov, O.V., et al., *OLEX<sup>2</sup>: a complete structure solution, refinement and analysis program*. Journal of Applied Crystallography, 2009. **42**: p. 339-341.
149. Hazen, R.M. and R.T. Downs, *High-Temperature and High-Pressure Crystal Chemistry*, in *Reviews in Mineralogy and Geochemistry*, R.M. Hazen and R.T. Downs, Editors. 2000, Mineralogical Society of America: Washington, D.C.
150. Lutz, H.D., et al., *Hydrogen bonding in solid hydroxides with strongly polarising metal ions,  $\beta$ -Be(OH)<sub>2</sub> and  $\epsilon$ -Zn(OH)<sub>2</sub>*. Spectrochimica Acta Part A: Molecular and Biomolecular Spectroscopy, 1998. **54**(7): p. 893-901.
151. Downs, R.T. and D.C. Palmer, *The pressure behavior of  $\alpha$ -cristobalite*. American Mineralogist, 1994. **79**: p. 9-14.
152. Kusaba, K., et al., *Single-crystal to single-crystal phase transition with a large deformation in Zn(OH)<sub>2</sub> under high-pressure*. Chem. Phys. Lett., 2007. **437**: p. 61-65.
153. Tolédano, P. and V. Dmitriev, *Phenomenological Theory of First-Order Phase Transitions*, in *Reconstructive Phase Transitions: In Crystals and Quasicrystals*. 1996, World Scientific: Singapore. p. 1-142.
154. Dove, M.T., *Theory of displacive phase transitions in minerals*. American Mineralogist, 1997. **82**: p. 213-244.

155. Hatch, D.M., S. Ghose, and J.L. Bjorkstam, *The  $\alpha$ - $\beta$  phase transition in  $AlPO_4$  cristobalite: Symmetry analysis, domain structure and transition dynamics*. Physics and Chemistry of Minerals, 1994. **21**(1-2): p. 67-77.
156. Simonov, M.A., Y.K. Egorov-Tismenko, and N.V. Belov, *Utochnennaya kristallicheskaya struktura chkalovita  $Na_2Be[Si_2O_6]$* . Doklady Akademii Nauk SSSR, 1975. **225**: p. 1319-1322.
157. Dove, M.T., et al., *Crystal structure of the high-pressure monoclinic phase-II of cristobalite,  $SiO_2$* . Mineralogical Magazine, 2000. **64**: p. 569-576.
158. Kusaba, K., et al., *Structural consideration of phase transitions in  $Zn(OH)_2$  under high pressure*. Journal of Physics: Conference Series, 2010. **2015**: p. 012001.
159. Palmer, D.C. and L.W. Finger, *Pressure-induced phase transition in cristobalite: An X-ray powder diffraction study to 4.4 GPa*. American Mineralogist, 1994. **79**: p. 1-8.
160. Müller, U., *Inorganic Structural Chemistry, Second Edition*. 2006: John Wiley & Sons.
161. Prewitt, C.T. and R.T. Downs, *Ultrahigh-Pressure Mineralogy: Physics and Chemistry of the Earth's Deep Interior.*, in *Reviews in Mineralogy*, R.J. Hemley, Editor. 1998, Mineralogical Society of America: Washington, D.C.
162. Schmidt, M.W., et al., *Synthesis, crystal structure, and phase relations of  $AlSiO_3OH$ , a high-pressure hydrous phase*. American Mineralogist, 1998. **83**: p. 881-888.
163. Tsuchiya, J., *First principles prediction of a new high-pressure phase of dense hydrous magnesium silicates in the lower mantle*. Geophys. Res. Lett, 2013. **40**: p. 4570-4573.
164. Bindi, L., et al., *Crystal chemistry of dense hydrous magnesium silicates: The structure of phase H,  $MgSiH_2O_4$ , synthesized at 45 GPa and 1000° C*. American Mineralogist, 2014. **99**: p. 1802-1805.
165. McKee William, C., et al., *Covalent Hypercoordination: Can Carbon Bind Five Methyl Ligands?* Angewandte Chemie International Edition, 2014. **53**(30): p. 7875-7878.
166. Angel, R.J., et al., *A Silica-Rich Sodium Pyroxene Phase With Six-Coordinated Silicon*. Nature, 1988. **335**: p. 156.
167. Santoro, M., et al., *Synthesis of 1D Polymer/Zeolite Nanocomposites under High Pressure*. Chemistry of Materials, 2016. **28**(11): p. 4065-4071.

168. Scelta, D., et al., *High Pressure Polymerization in a Confined Space: Conjugated Chain/Zeolite Nanocomposites*. Chemistry of Materials, 2014. **26**(7): p. 2249-2255.
169. Santamaría-Pérez, D., et al., *Structural Evolution of CO<sub>2</sub>-Filled Pure Silica LTA Zeolite under High-Pressure High-Temperature Conditions*. Chemistry of Materials, 2017. **29**(10): p. 4502-4510.
170. Santoro, M., et al., *Carbon Enters Silica Forming a Cristobalite-type CO<sub>2</sub>-SiO<sub>2</sub> Solid Solution*. Nature Communications, 2014. **5**: p. 3761.
171. Santoro, M., et al., *Partially Collapsed Cristobalite Structure in the Non Molecular Phase V in CO<sub>2</sub>*. Proceedings of the National Academy of Sciences, 2012. **109**(14): p. 5176-5179.
172. Hammonds, K.D., et al., *Rigid-Unit Phonon Modes and Structural Phase Transitions in Framework Silicates*. American Mineralogist, 1996. **81**(9-10): p. 1057-1079.
173. Campana, C., et al., *Irreversibility of the Pressure-Induced Phase Transition of Quartz and the Relation Between Three Hypothetical Post-Quartz Phases*. Physical Review B, 2004. **70**: p. 224101.
174. Donadio, D., et al., *Influence of Temperature and Anisotropic Pressure on the Phase Transition in  $\alpha$ -Cristobalite*. Physical Review Letters, 2008. **100**: p. 165502.
175. Garg, N. and S.M. Sharma, *Classical Molecular Dynamical Simulations of High-Pressure Behavior of Alpha Cristobalite (SiO<sub>2</sub>)*. Journal of Physics: Condensed Matter, 2007. **19**: p. 456201.
176. Tsuchida, Y. and T. Yagi, *New Pressure-Induced Transformations of Silica at Room Temperature*. Nature, 1990. **347**(6290): p. 267-269.
177. Dubrovinsky, L.S., et al., *A Class of New High-Pressure Silica Polymorphs*. Physics of the Earth and Planetary Interiors, 2004. **143-144**: p. 231-240.
178. Dubrovinsky, L.S., et al., *Pressure-Induced Transformations of Cristobalite*. Chemical Physics Letters, 2001. **333**: p. 264-270.
179. Bläß, U.W., *Shock-Induced Formation Mechanism of Seifertite in Shergottites*. Physics and Chemistry of Minerals, 2013. **40**(5): p. 425-437.
180. Xue, S.-H., et al., *Induced Transformation of Amorphous Silica to Cristobalite on Bacterial Surfaces*. RSC Advances, 2015. **5**(88): p. 71844-71848.

181. Keskar, N.R. and J.R. Chelikowsky, *Anomalous Elastic Behavior in Crystalline Silica*. Physical Review B, 1993. **48**(22): p. 16227-16233.
182. Grima, J.N., et al., *On the Origin of Auxetic Behaviour in the Silicate  $\alpha$ -Cristobalite*. Journal of Materials Chemistry, 2005. **15**(37): p. 4003-4005.
183. Yeganeh-Haeri, A., D.J. Weidner, and J.B. Parise, *Elasticity of  $\alpha$ -Cristobalite: A Silicon Dioxide with a Negative Poisson's Ratio*. Science, 1992. **257**: p. 650-652.
184. El Goresy, A., et al., *Seifertite, a Dense Orthorhombic Polymorph of Silica from the Martian Meteorites Shergotty and Zagami*. European Journal of Mineralogy, 2008. **20**: p. 532-528.
185. Dera, P., et al., *Characterization of a High-Pressure Phase of Silica from the Martian Meteorite Shergotty*. American Mineralogist, 2002. **87**(7): p. 1018.
186. Rivers, M.L., et al., *The COMPRES/GSECARS Gas Loading System for Diamond Anvil Cells at the Advanced Photon Source*. High Pressure Research, 2008. **28**: p. 273-292.
187. Altomare, A., et al., *SIR92 - A Program for Automatic Solution of Crystal Structures by Direct Methods*. Journal of Applied Crystallography, 1994. **27**(3): p. 435.
188. Gonzalez-Platas, J., et al., *EosFit7-GUI: A New Graphical User Interface for Equation of State Calculations, Analyses and Teaching*. Journal of Applied Crystallography, 2016. **49**(4): p. 1377-1382.
189. Kresse, G. and J. Hafner, *Ab Initio Molecular Dynamics for Liquid Metals*. Physical Review B, 1993. **47**(1): p. 558-561.
190. Román-Pérez, G. and J.M. Soler, *Efficient Implementation of a van der Waals Density Functional: Application to Double-Wall Carbon Nanotubes*. Physical Review Letters, 2009. **103**(9): p. 096102.
191. Hill, R., *The Elastic Behaviour of a Crystalline Aggregate*. Proceedings of the Physical Society. Section A, 1952. **65**(5): p. 349.
192. Ranganathan, S.I. and M. Ostoja-Starzewski, *Universal Elastic Anisotropy Index*. Physical Review Letters, 2008. **101**(5): p. 055504.
193. Gratz, A.J., et al., *Shock Amorphization of Cristobalite*. Science, 1993. **259**: p. 663-666.
194. Kubo, T., et al., *Curious Kinetic Behavior in Silica Polymorphs Solves Seifertite Puzzle in Shocked Meteorite*. Science Advances, 2015. **1**(4).

195. Putz, H., J.C. Schon, and M. Jansen, *Combined Method for 'Ab Initio' Structure Solution from Powder Diffraction Data*. Journal of Applied Crystallography, 1999. **32**: p. 864-870.
196. Teter, D.M., et al., *High Pressure Polymorphism in Silica*. Physical Review Letters, 1998. **80**(10): p. 2145-2148.
197. Hu, Q.Y., et al., *Stability Limits and Transformation Pathways of  $\alpha$ -Quartz Under High Pressure*. Physical Review B, 2017. **95**(10): p. 104112.
198. Wang, F., et al., *P-V-T Equation of State of Stishovite up to Mid-Lower Mantle Conditions*. Journal of Geophysical Research: Solid Earth, 2012. **117**(B6).
199. Grocholski, B., S.H. Shim, and V.B. Prakapenka, *Stability, Metastability, and Elastic Properties of a Dense Silica Polymorph, Seifertite*. Journal of Geophysical Research: Solid Earth, 2013. **118**(9): p. 4745-4757.
200. Haines, J., et al., *Crystalline post-quartz phase in silica at high-pressure*. Physical Review Letters, 2001. **87**: p. 155503.
201. Liu, L.-G., W.A. Bassett, and J. Sharry, *New High-Pressure Modifications of GeO<sub>2</sub> and SiO<sub>2</sub>*. Journal of Geophysical Research: Solid Earth, 1978. **83**(B5): p. 2301-2305.
202. Huang, L., M. Durandurdu, and J. Kieffer, *Transformation Pathways of Silica under High Pressure*. Nature Materials, 2006. **5**(12): p. 977-981.
203. Yahagi, Y., et al., *Infrared Absorption Spectra of the High-Pressure Phases of Cristobalite and their Coordination Numbers of Silicon Atoms*. Solid State Communications, 1994. **89**: p. 945-948.
204. Tsuneyuki, S., et al., *New Pressure-Induced Structural Transformations in Silica Obtained by Computer Simulation*. Nature, 1989. **339**(6221): p. 209-211.
205. Klug, D.D., et al., *Ab Initio Molecular Dynamics Study of the Pressure-Induced Phase Transformations in Cristobalite*. Physical Review B, 2001. **B63**: p. 104106.
206. Wehinger, B., et al., *Lattice Dynamics of  $\alpha$ -Cristobalite and the Boson Peak in Silica Glass*. Journal of Physics: Condensed Matter, 2015. **27**(30): p. 305401.
207. Kieffer, S.W., *Thermodynamics and Lattice Vibrations of Minerals: 1. Mineral Heat Capacities and Their Relationships to Simple Lattice Vibrational Models*. Reviews of Geophysics, 2010. **17**(1): p. 1-19.

208. Navrotsky, A., *Physics and Chemistry of Earth Materials*. 6 ed. Cambridge Topics in Mineral Physics and Chemistry. 1994, Cambridge: Cambridge University Press.
209. Amos, D.M., et al., *A Chiral Gas–Hydrate Structure Common to the Carbon Dioxide–Water and Hydrogen–Water Systems*. *The Journal of Physical Chemistry Letters*, 2017. **8**(17): p. 4295-4299.
210. Tian, Y.Q., et al., *The Silica-Like Extended Polymorphism of Cobalt(II) Imidazolate Three-Dimensional Frameworks: X-ray Single-Crystal Structures and Magnetic Properties*. *Chemistry – A European Journal*, 2003. **9**(22): p. 5673-5685.
211. Hu, Q.Y., et al., *Polymorphic Phase Transition Mechanism of Compressed Coesite*. *Nature Communications*, 2015. **6**: p. 6630.
212. Černok, A., et al., *High-Pressure Crystal Chemistry of Coesite-I and its Transition to Coesite-II*. *Zeitschrift für Kristallographie - Crystalline Materials*, 2014. **229**(11): p. 761.
213. Oganov, A.R., et al., *Structure, Bonding, and Mineralogy of Carbon at Extreme Conditions*. *Reviews in Mineralogy and Geochemistry*, 2013. **75**(1): p. 47-77.
214. Yoo, C.-S., A. Sengupta, and M. Kim, *Carbon Dioxide Carbonates in the Earth's Mantle: Implications to the Deep Carbon Cycle*. *Angewandte Chemie International Edition*, 2011. **50**(47): p. 11219-11222.
215. Iota, V., et al., *Six-fold Coordinated Carbon Dioxide VI*. *Nature Materials*, 2007. **6**(1): p. 34-38.
216. Togo, A., F. Oba, and I. Tanaka, *Transition Pathway of CO<sub>2</sub> Crystals Under High Pressures*. *Physical Review B*, 2008. **77**(18): p. 184101.
217. Maeda, F., et al., *Diamond Formation in the Deep Lower Mantle: a High-Pressure Reaction of MgCO<sub>3</sub> and SiO<sub>2</sub>*. *Scientific Reports*, 2017. **7**: p. 40602.
218. Hiskey, M.A., D.E. Chavez, and D.L. Naud, *Insensitive High-Nitrogen Compounds*. 2001, Los Alamos National Lab. NTIS No: DE-2001-776133.
219. Xu, D., et al., *Flame-retardant effect and mechanism of melamine phosphate on silicone thermoplastic elastomer*. *RSC Advances*, 2018. **8**(9): p. 5034-5041.
220. Liu, A.Y. and M.L. Cohen, *Prediction of New Low Compressibility Solids*. *Science*, 1989. **245**: p. 841-842.

221. Li, J., *An Ab Initio Theoretical Study of 2,4,6-Trinitro-1,3,5-Triazine, 3,6-Dinitro-1,2,4,5-Tetrazine, and 2,5,8-Trinitro-Tri-s-Triazine*. Propellants, Explosives, Pyrotechnics., 2008. **33**: p. 443-447.
222. Coburn, M.D., et al., *Synthesis of Poly(S,S-Dimethylsulfilimino)heterocycles*. Synthesis, 1986. **6**: p. 490-492.
223. Hartman, G.D., R.D. Hartman, and J.E. Schwering, Tetrahedron Letters, 1983. **24**: p. 1011.
224. Hejny, C. and V.S. Minkov, *High-pressure crystallography of periodic and aperiodic crystals*. IUCrJ, 2015. **2**(2): p. 218-229.
225. Ma, H.A., et al., *High-pressure pyrolysis study of C<sub>3</sub>N<sub>6</sub>H<sub>6</sub>: a route to preparing bulk C<sub>3</sub>N<sub>4</sub>*. J. Phys.: Condens. Matter, 2002. **14**: p. 11269-11273.
226. Montigaud, H., et al., *C<sub>3</sub>N<sub>4</sub>: Dream or reality? Solvothermal synthesis as macroscopic samples of the C<sub>3</sub>N<sub>4</sub> graphitic form*. J. Mater. Sci., 2000. **35**: p. 2547-2552.
227. Yao, L.D., et al., *Study of the products of melamine (C<sub>3</sub>N<sub>6</sub>H<sub>6</sub>) treated at high pressure and high temperature*. Phys. Stat. Sol., 2005. **202**: p. 2679-2685.
228. Wu, X., et al., *High-pressure pyrolysis of melamine route to nitrogen-doped conical hollow and bamboo-like carbon nanotubes*. Diamond and Rel. Mater., 2006. **16**: p. 164-170.
229. Yu, D.L., et al., *Phase transformation of melamine at high pressure and temperature*. J. Mater. Sci., 2008. **43**: p. 689-695.
230. Hamann, S.D. and M. Linton, *The influence of pressure on the infrared spectra of hydrogen bonded solids. III Compounds with N-H...X bonds*. Aust. J. Chem., 1976. **29**: p. 1641-1647.
231. Zhao, Y., et al., *High pressure raman spectra of melamine (C<sub>3</sub>H<sub>6</sub>N<sub>6</sub>) and pressure induced transition*. High Pres. Res., 1990. **3**: p. 233-235.
232. Ma, H.A., et al., *Crystal structures of C<sub>3</sub>N<sub>6</sub>H<sub>6</sub> under high pressure*. Chem. Phys. Lett., 2003. **368**: p. 668-672.
233. Liu, X.R., et al., *Raman Spectroscopy of Melamine at High Pressures*. J. Phys.: Conf. Series, 2010. **215**: p. 012045.

234. Pravica, M., et al., *High-pressure studies of melamine*. High Pres. Res., 2010. **30**: p. 65-71.
235. Sheldrick, G.M., *CELL\_NOW*. 2008, Georg-August-Universität Göttingen: Göttingen, Germany.
236. Vinet, P., et al., *Temperature effects on the universal equation of state of solids*. Physical Review B, 1987. **35**(4): p. 1945-1953.
237. Jeanloz, R., *Universal equation of state*. Physical Review B, 1988. **38**(1): p. 805-807.
238. Dolomanov, O.V., et al., *OLEX2: a complete structure solution, refinement and analysis program*. Journal of Applied Crystallography, 2009. **42**(2): p. 339-341.
239. Wolff, S.K., et al., *CrystalExplorer (Version 3.1)*. 2012, University of Western Australia.
240. Menges, F., *Spectragryph - optical spectroscopy software*. 2018.
241. Varghese, J.N., A.M. O'Connell, and E.N. Maslen, *The X-ray and Neutron Crystal Structure of 2,4,6-Triamino-1,3,5-triazine (Melamine)*. Acta Cryst., 1977. **B33**: p. 2102-2108.
242. Hanfland, M., K. Brister, and K. Syassen, *Graphite under pressure: Equation of state and first-order Raman modes*. Phys. Rev. B, 1989. **39**: p. 12598-12603.
243. Peiris, S.M. and G.J. Piermarini, *Static Compression of Energetic Materials*. Shock Wave and High Pressure Phenomena. 2008, Berlin: Springer. 108-110.
244. Yoo, C.S., et al. *Equations of State of Unreacted High Explosives at High Pressures in 11th International Detonation Symposium*. 1998. Snowmass Village, CO: Lawrence Livermore National Laboratory.
245. Stevens, L.L., et al., *Hydrostatic Compression Curve for Triamino-Trinitrobenzene Determined to 13.0 GPa with Powder X-Ray Diffraction*. Propellants, Explosives, Pyrotechnics, 2008. **33**(4): p. 286-295.
246. Gump, J.C. and S.M. Peiris, *Isothermal equations of state of beta octahydro-1,3,5,7-tetranitro-1,3,5,7-tetrazocine at high temperatures*. Journal of Applied Physics, 2005. **97**(5): p. 053513.
247. Plisson, T., et al., *Equation of state of 1,3,5-triamino-2,4,6-trinitrobenzene up to 66 GPa*. Journal of Applied Physics, 2017. **122**(23): p. 235901.

248. Davidson, A.J., et al., “*Stubborn*” triaminotrinitrobenzene: Unusually high chemical stability of a molecular solid to 150 GPa. *The Journal of Chemical Physics*, 2011. **135**(17): p. 174507.
249. Dove, M.T., et al., *Rigid Unit Modes in Framework Structures: Theory, Experiment and Applications*. *Reviews in Mineralogy and Geochemistry*, 2000. **39**(1): p. 1.
250. Spackman, M.A. and D. Jayatilaka, *Hirshfeld surface analysis*. *CrystEngComm*, 2009. **11**(1): p. 19-32.
251. McKinnon, J.J., D. Jayatilaka, and M.A. Spackman, *Towards quantitative analysis of intermolecular interactions with Hirshfeld surfaces*. *Chemical Communications*, 2007(37): p. 3814-3816.
252. Mooibroek, T.J. and P. Gamez, *The s-triazine ring, a remarkable unit to generate supramolecular interactions*. *Inorganica Chimica Acta*, 2007. **360**(1): p. 381-404.
253. Martinez, C.R. and B.L. Iverson, *Rethinking the term "pi-stacking"*. *Chemical Science*, 2012. **3**(7): p. 2191-2201.
254. Mishra, B.K., J.S. Arey, and N. Sathyamurthy, *Stacking and Spreading Interaction in N-Heteroaromatic Systems*. *The Journal of Physical Chemistry A*, 2010. **114**(36): p. 9606-9616.
255. Hunter, C.A. and J.K.M. Sanders, *The nature of  $\pi$ - $\pi$  interactions*. *Journal of the American Chemical Society*, 1990. **112**(14): p. 5525-5534.
256. Thiery, M.M., K. Kobashi, and I.L. Spain, *Raman spectra of solid benzene under high pressure*. *Solid State Comm.*, 1985. **54**: p. 95-97.
257. Schneider, J.R. and B. Schrader, *Measurement and calculation of the infrared and Raman active molecular and lattice vibrations of the crystalline melamine (1,3,5-triamino-s-triazine)*. *J. Mol. Str.*, 1975. **29**: p. 1-14.
258. Larkin, P.J., M.P. Makowski, and N.B. Colthup, *The form of the normal modes of s-triazine: infrared and Raman spectral analysis and ab initio force field calculations*. *Spectr. Acta A*, 1999. **55**: p. 1011-1020.
259. Marchewka, M.K., *Infrared and Raman spectra of the new melaminium salt: 2,4,6-triamino-1,3,5-triazin-1-ium hydrogenphthalate*. *Mater. Lett.*, 2004. **58**: p. 843-848.

260. Marchewka, M.K., *Infrared and Raman spectra of melaminium chloride hemihydrate*. Mater. Sci. and Eng., 2002. **B95**: p. 214-221.
261. Goncharov, A. and E. Gregoryanz, *Chapter 8 - Solid Nitrogen at Extreme Conditions of High Pressure and Temperature*, in *Chemistry at Extreme Conditions*, M.R. Manaa, Editor. 2005, Elsevier: Amsterdam. p. 241-267.
262. Song, Y., et al., *Chapter 6 - Nitrogen-Containing Molecular Systems at High Pressures and Temperature*, in *Chemistry at Extreme Conditions*, M.R. Manaa, Editor. 2005, Elsevier: Amsterdam. p. 189-222.
263. Li, W., et al., *A Novel High-Density Phase and Amorphization of Nitrogen-Rich 1H-Tetrazole (CH<sub>2</sub>N<sub>4</sub>) under High Pressure*. Scientific Reports, 2017. **7**: p. 39249.
264. Szatyłowicz, H., *Structural aspects of the intermolecular hydrogen bond strength: H-bonded complexes of aniline, phenol and pyridine derivatives*. Journal of Physical Organic Chemistry, 2008. **21**(10): p. 897-914.
265. Citroni, M., et al., *Structural and Electronic Competing Mechanisms in the Formation of Amorphous Carbon Nitride by Compressing s-Triazine*. The Journal of Physical Chemistry C, 2015. **119**(51): p. 28560-28569.
266. Li, S., et al., *Effect of pressure on heterocyclic compounds: Pyrimidine and s-triazine*. The Journal of Chemical Physics, 2014. **141**(11): p. 114902.
267. Li, W., et al., *Pressure-Induced Diversity of  $\pi$ -Stacking Motifs and Amorphous Polymerization in Pyrrole*. The Journal of Physical Chemistry C, 2014. **118**(23): p. 12420-12427.
268. Zhuravlev, K.K., et al., *Raman and infrared spectroscopy of pyridine under high pressure*. Physical Review B, 2010. **82**(6): p. 064116.
269. Wang, K., et al., *Stability of Hydrogen-Bonded Supramolecular Architecture under High Pressure Conditions: Pressure-Induced Amorphization in Melamine–Boric Acid Adduct*. Langmuir, 2009. **25**(8): p. 4787-4791.
270. Wang, K., et al., *Pressure-Induced Phase Transition in Hydrogen-Bonded Supramolecular Adduct Formed by Cyanuric Acid and Melamine*. The Journal of Physical Chemistry B, 2009. **113**(44): p. 14719-14724.

271. Zhang, S., et al., *Pressure-Induced Stable Beryllium Peroxide*. Inorganic Chemistry, 2017. **56**(9): p. 5233-5238.
272. Martonak, R., et al., *From four- to six-coordinated silica: Transformation pathways from metadynamics*. Phys. Rev., 2007. **B76**: p. 014120.
273. Zakharov, B. and E. Boldyreva, *High pressure: a complementary tool for probing solid state processes*. CrystEngComm, 2018.